The dynamics of an axisymmetric turbulent jet and of a passive scalar patch in ambient turbulence interpreted from the passive scalar field statistics

Rana Sahebjam
Department of Civil Engineering
McGill University, Montreal
August, 2022

A thesis submitted to McGill University in partial fulfillment of the requirements of the degree of

Doctor of Philosophy

Abstract

The concentration field of an axisymmetric turbulent jet and a momentumless patch of a passive scalar in an approximately homogeneous isotropic turbulence (HIT) with negligible mean flow is studied experimentally. The present research builds on the work of Khorsandi et al. (2013) and Perez-Alvarado (2016), who studied the velocity field and the passive scalar field of an axisymmetric turbulent jet emitted into a turbulent background, respectively. The primary objective of this work is to deduce the jet structure, and to study the evolution of a high-Schmidt number passive scalar within the turbulent jet in the HIT ambient by following the meandering path of the jet. The secondary objective is to investigate the effect of the HIT ambient on the diffusion of a momentumless patch of a passive scalar released from an isokinetic source, which complements the first objective as once the jet has decayed, the passive scalar is only subject to turbulent diffusion in the HIT ambient.

The effect of a turbulent ambient on the dynamics and mixing of the passive scalar field of an axisymmetric turbulent jet is investigated by comparing experiments conducted in a turbulent ambient to those in a quiescent ambient. The turbulent ambient was generated by a random jet array to achieve an approximately homogeneous isotropic turbulence (HIT) with negligible mean flow along the jet axis, as previously documented by Khorsandi et al. (2013) and Perez-Alvarado (2016). Two jet Reynolds numbers of $Re =$ 5800 and 10600 were studied, where $Re = U_0 d/\nu$ is defined based on the jet exit velocity, U_0, the exit diameter, d, and the kinematic viscosity of the jet fluid (water), ν. Planar laser-induced fluorescence was used to measure the concentrations of the passive scalar dye

(disodium fluorescein, Sc = 2000) at orthogonal cross-sections of the jet at axial distances of x/d = 20, 30, 40, 50, 60. The statistics of the passive scalar field were conditioned on the jet centroid, removing the effect of the large ambient eddies which advect the jet laterally and leaving on the effect of the smaller ambient eddies which modify the jet entrainment and mixing. The centroidally conditioned statistics were compared to the commonly used Eulerian statistics and to those of the jet in a quiescent ambient. The use of the centroidal analysis allowed the structure of the jet in the HIT ambient to be deduced, for which a two-region model was proposed. In the first region, following the developing region of the jet, the ambient turbulence disrupts the jet structure and results in a faster concentration decay compared to the quiescent ambient. At a critical downstream distance, where the relative turbulence intensity between the ambient and the jet ($\xi = u_{rms,\,HIT}/u_{rms,\,jet},$, where u_{rms} denotes the root mean square velocity) exceeds 0.5, the HIT ambient has destroyed the jet structure and the second region starts. In the second region, the turbulent diffusion is the only mechanism to transport the passive scalar field. The centroidal statistics of the mean scalar properties show self-similarity and self-preservation before jet break-up. The width of the jet is larger in the HIT ambient compared to that in the quiescent ambient and grows with axial distance, but remains unchanged beyond the jet break-up. Using the present passive scalar data and the velocity data from Khorsandi et al. (2013) and Lai et al. (2019), it is argued that the momentum-driven entrainment of the jet in the HIT ambient is reduced compared to that in the quiescent ambient, and that the entrainment ceases beyond the jet break-up. The entrainment of the smaller scales of the ambient turbulence leads to a wider range of centerline concentrations and rms concentrations within the jet, and they are hypothesized to increase local concentration gradients and reduce the jet mixing.

Diffusion of a momentumless patch of a passive scalar in the same HIT ambient is studied. A high-Schmidt number passive scalar dye (Rhodamine 6G, Sc = 2500) is released isokinetically from a large diameter jet (d = 29.97 mm), and an orthogonal view of the passive scalar field is obtained using planar laser-induced fluorescence. The temporal

evolution of the passive scalar field is due to molecular diffusion and to turbulent diffusion in a quiescent ambient and in the HIT ambient, respectively. Time-averaged statistics of the passive scalar field are assessed at $t = 0.2, 1, 1.8, 2.6, 3.4$ s using a centroidal analysis. The mean concentration decays quickly and the rms concentration increases within the scalar patch. Compared to the quiescent ambient case, a much wider range of concentrations is present at the centroid of the scalar field. The size of the scalar patch increases with time, which is attributed to an increasing turbulent diffusivity for times shorter than the integral time scale of the turbulence.

Abrégé

Le champ du scalaire passif d'un jet turbulent axisymétrique et d'un jet isocinétique dans une turbulence approximativement homogène isotrope (THI) avec un écoulement moyen négligeable sont étudiés expérimentalement. Cette enquête se base sur les travaux de Khorsandi et al. (2013) et Perez-Alvarado (2016) qui étudièrent le champ de vitesse et le champ du scalaire passif d'un jet turbulent axisymétrique émis dans un milieu turbulent. L'objectif principal de cette étude est de déduire la structure d'un jet ainsi que d'étudier l'évolution d'un scalaire passif à grand nombre de Schmidt au sein d'un jet dans une THI ambiante en suivant le parcours à méandres du jet. L'objectif secondaire complète le premier en s'intéressant à l'effet de la THI ambiante sur la diffusion d'une parcelle sans quantité de mouvement d'un scalaire passif émis par une source isocinétique puisqu'une fois le jet désintégré, le scalaire passif est uniquement soumis à la diffusion turbulente dans une THI ambiante.

L'effet d'une turbulence ambiante sur les dynamiques et mélange du champ de scalaire passif d'un jet turbulent axisymétrique est étudié en comparant les résultats d'expériences conduites dans un milieu turbulent à ceux d'expériences faites dans un milieu tranquille. Le milieu turbulent fut produit par un Random Jet Array afin d'atteindre une turbulence approximativement homogène isotrope (THI) avec un écoulement moyen négligeable au long de l'axe du jet tel que décrit par Khorsandi et al. (2013) et Perez-Alvarado (2016). Deux jets avec un nombre de Reynolds de Re = 5800 et 10600 furent étudiés, où $Re = U_0 d/\nu$ est basé sur la vélocité de sortie du jet U_0, le diamètre de sortie d, et la viscosité cinématique du jet d'eau ν. La fluorescence planaire induite par laser fut utilisée pour mesurer les concentrations de la teinture fluorescente du passif scalaire (disodium fluorescein, Sc = 2000) à des coupes transversales orthogonales du jet à des distances axiales de x/d = 20, 30, 40, 50, 60. Les statistiques du champ du scalaire passif furent conditionnées au centroïde du jet, supprimant ainsi l'effet des tourbillons ambiants majeurs qui déplacent le jet latéralement tout en conservant l'effet des plus petits tourbillons qui modifient l'entrainement et le mélange du jet. Les statistiques conditionnées au centroïde du jet sont comparées aux statistiques Eulériennes et à celles du jet en milieu tranquille. L'utilisation de l'analyse du centroïde permit la déduction de la structure du jet dans le milieu THI, pour laquelle un modèle à deux régions est proposé. Dans la première région, qui est celle qui suit la formation du jet, la turbulence ambiante interrompt la structure du jet et produit une déchéance de la concentration plus rapide que dans un milieu tranquille. À la distance en aval critique où l'intensité relative de la turbulence entre le milieu et le jet dépasse 0.5 ($\xi = u_{rms,\,THI}/u_{rms,\,jet}$, où u_{rms} est la racine carrée de la vélocité), le milieu THI a détruit la structure du jet et marque ainsi le commencement de la deuxième région. Dans la deuxième région, la diffusion turbulente est le seul mécanisme assurant le transport du champ du scalaire passif. Les statistiques du centroïde des propriétés moyennes du scalaire démontrent l'auto-similarité et l'auto-préservation avant la désintégration du jet. La largeur du jet est plus ample dans un milieu THI comparée à celle obtenue dans un milieu tranquille et croît avec la distance axiale, alors qu'elle reste constante au-delà de la désintégration du jet. En utilisant les données du champ du scalaire passif et de la vélocité publiées par Khorsandi et al. (2013) et Lai et al. (2019), on soutient que l'entrainement du jet généré par la dynamique dans un milieu THI est réduit comparé à celui observé dans un milieu tranquille et que l'entrainement cesse une fois le jet dissipé. L'entrainement des plus petites échelles de la turbulence ambiante mène à une plus grande fourchette de concentrations de ligne médiane et des concentrations rms au sein du jet, et il est supposé que ces dernières augmentent les gradients de concentration locaux et réduisent le mélange du jet.

La diffusion d'une parcelle de scalaire passif sans quantité de mouvement dans le même milieu THI est étudiée. Une teinture de scalaire passif avec un haut nombre de Schmidt (Rhodamine 6G, Sc = 2500) est émise isocinétiquement depuis un jet à grand diamètre (d = 29.97 mm), et une coupe orthogonale du champ de scalaire passif est obtenue en utilisant une fluorescence planaire induite par laser. L'évolution temporelle du champ du scalaire passif est due à la diffusion moléculaire et à la diffusion turbulente dans un milieu tranquille et dans un milieu THI. Les statistiques moyennes dans le temps du champ du scalaire passif sont évaluées à t = 0.2, 1, 1.8, 2.6, 3.4 s avec une analyse centroïdale. La concentration moyenne se dégrade rapidement et la concentration rms augmente au sein de la parcelle scalaire. Comparé au milieu tranquille, une plus ample fourchette de concentration est présente dans le centroïde du champ scalaire. La croissance de la taille de la parcelle scalaire avec le temps est attribuée à l'augmentation de la diffusivité turbulente pour des temps plus courts que l'échelle de temps intégrale de la turbulence.

Table of Contents

Acknowledgements

I would like to express my sincere gratitude to my supervisor, Prof. Susan Gaskin for her continual support and guidance during my PhD. I gratefully acknowledge the Faculty of Engineering for providing a McGill engineering doctoral award. I would like to thank the members of the technical staff at the Civil Engineering Department for their assistance in the laboratory, especially John Bartczak for his smart suggestions, and William Boyd Dumais. I would thank Dr. Babak Khorsandi for his advice on my project-related questions. I would like to thank my friend and colleague, Khashayar, for his helpful discussions and technical support during my studies. Also, I am thankful to my fellow graduate students and friends, Farzin, and Romaric, for their support. Finally, I would like to extend my gratitude to my family who continually supported me throughout my studies as well as at other stages of my life.

Contribution to original knowledge

The research is a systematic study of the passive scalar field of an axisymmetric turbulent jet in an approximately homogeneous isotropic turbulence (HIT) with negligible mean flow. The aim was to determine how the ambient turbulence changes the entrainment and mixing of the jet and hence also its structure.

The experimental configuration of the RJA and jet produced an almost constant intensity of background turbulence along the jet axis allowing for the study of the effect of a constant level of external turbulence on the downstream evolution of jets with two Reynolds numbers (Re = 5800 and 10600). The ratio of the ambient turbulence intensity to the jet turbulence, ξ, increased over the range [0.16, 0.73] and the ratio of the length scales between the ambient and the jet, $\mathcal{L}$, decreased over the range [6.3, 2.2].

Past studies have used Eulerian analyses of velocity and/or passive scalar statistics, which average the effect of the large scales of the ambient turbulence advecting the jet laterally and resulting in a meandering jet path, and the effect of the smaller scales of the ambient, altering the entrainment and mixing in the jet. In this research, the analysis of the passive scalar statistics and, hence, jet evolution was conditioned on the jet centroid to remove the effect of the large ambient eddies advecting the jet laterally and to isolate the effect of the ambient turbulence intensity on the structure, entrainment and mixing of the jet.

A two-region model of the jet behavior was developed on the basis of the first-order statistics of the centroidal analysis. In the first region, the jet is self-similar and self-preserving, although the rate of concentration decay and the rate of width growth are greater than those in the quiescent ambient and result in a reduced entrainment rate. The second region starts once the jet structure breaks up and the scalar is dispersed only by molecular and turbulent diffusion, which occurs once the relative turbulence intensity between the ambient and the jet reaches a value of ξ = 0.5. In this region, there is no jet-driven entrainment, the width growth ceases and the behavior is no longer self-similar.

The results confirm previous research obtained using an Eulerian analysis, which found a reduction in entrainment before jet breakup and breakup occurring at a similar ratio of external to jet turbulence intensity (Gaskin et al., 2004; Khorsandi et al., 2013; Perez-Alvarado, 2016; Lai et al., 2019). However, the conditional analysis allows for the self-similarity and self-preservation of the jet in the first region to be identified, which is important as it is the jet structure (velocity) that drives the entrainment. The current results also demonstrate that the ambient turbulence affects the jet from the end of the zone of flow development in the same manner (i.e. there is no region in which the jet is unaffected by the ambient turbulence as postulated in previous research).

The self-similarity in the first region is shown, from the centroidal statistics, as the product of the decay of the centerline concentration (as $x^{-1.1}$) and of the half-width growth (as $x^{1.1}$), that were both independent of Reynolds number, scaled to a constant (x^0). The intermittency profile of the centroidally averaged profile provides further evidence that the jet structure is maintained until just before breakup as ambient fluid is not found at the centerline until breakup.

The mixing of the scalar within the jet was shown to be lower in the turbulent ambient due to the occurrence of a large range of concentrations within the jet, with supporting evidence provided by the PDFs and CDFs of the centroidally averaged centerline concentration. This is despite the greater radial transport of the scalar field in the turbulent ambient, and opposes Perez-Alvarado (2016)'s argument of an enhanced mixing in the HIT ambient.

The experiments on the turbulent diffusion of a momentumless passive scalar patch demonstrated the effectiveness/rapidity of the turbulent diffusion of the ambient turbulence (to which the jet was subjected) in dispersing the passive scalar. This demonstrates both the role of the jet in maintaining an orderly structure of the passive scalar before breakup and the resulting dispersion of the passive scalar after breakup.

Contribution of authors

This manuscript-based thesis is consisted of two articles. The work presented in this thesis is mainly the result of my work and research undertaken under the supervision of Prof. Susan Gaskin. My colleague Khashayar F. Kohan contributed to paper one to a small extent. The details of the contributions for each manuscript are summarized below:

Manuscript 1 (Chapter 4): The dynamics of an axisymmetric turbulent jet in ambient turbulence interpreted from the passive scalar field statistics. This paper has been published in Physics of Fluids. Under the supervision of Prof. Susan Gaskin, I carried out the experiments and data collection, analyzed and discussed the results, and wrote the manuscript, which was subsequently edited for publication by Prof. Gaskin. Khashayar F. Kohan provided some ideas and references on turbulent non-turbulent interface, carried out mathematical calculations for the jet entrainment, and reviewed the manuscript. Prof. Susan Gaskin, supervised the project, provided guidance for the experiments and the analysis, and reviewed the manuscript.

Manuscript 2 (Chapter 5): Diffusion of a passive scalar patch in turbulent ambient is studied to complement the results from the previous chapter. Under the supervision of Prof. Susan Gaskin, I modified and extended the existing experimental setup, carried out the experiments and data collection, analyzed and discussed the results, and wrote the manuscript, which was subsequently edited by Prof. Gaskin. Professor Gaskin supervised the project, provided guidance for the experiments and the analysis, and reviewed the manuscript.

List of Figures

List of Tables

Nomenclature

A, B	calibration constants
A_ϕ	surface area of the scalar field
$b_{1/2}$	velocity half-width
b_m	characteristics half-width
$b_{\phi,\,1/2}$	concentration half-width
D	rate of dispersion
d	jet inner diameter
$\mathcal{D}$	molecular diffusivity
$\mathcal{D}_{ij}$	turbulent diffusivity tensor
$\mathcal{D}_t$	turbulent diffusivity
E_b	boundary velocity
E_v	global entrainment velocity
F	scalar flux
I	intensity

I_f	fluorescence intensity
I_{f_0}	incident fluorescence intensity
K	shape constant
k_{HIT}	ambient turbulent kinetic energy at y/M = 7.3
L	integral length scale
L_{HIT}	ambient length scale at $y/\mathrm{M} = 7.3$
$\mathcal{L}$	relative length scale
M	center to center distance between RJA pumps
M	momentum flux
m	mass flow rate
n	growth exponent of the concentration half-width
Pe	Peclet number
R	auto-correlation
r	radial coordinate
Re	Reynolds number
Re_λ	Taylor Reynolds number
S	spreading rate of concentration field
Sc	Schmidt number
Sc_t	turbulent Schmidt number
T	integral time scale

T_{HIT}	ambient time scale at y/M = 7.3
t	time
t_B	Batchelor timescale
U_0	jet exit velocity
$\tilde{u}$	Lagrangian velocity fluctuation
$\overline{U}$	mean axial velocity
u	fluctuating axial velocity
u_m	characteristic velocity
u_τ	characteristic turbulence intensity of the HIT ambient
$\overline{V}$	mean lateral velocity
v	fluctuating lateral velocity
$\overline{W}$	mean vertical velocity
w	fluctuating vertical velocity
X	displacement of a single particle dispersion
x	axial coordinate
x_0	virtual origin
y	lateral coordinate
z	vertical coordinate

Greek Symbols

α	entrainment coefficient

β	molar absorptivity of dye
η	Kolmogorov length scale
η_B	Batchelor microscale
η_C	Corrsin microscale
γ	intermittency
κ_u	decay constant of velocity field
κ_ϕ	decay constant of concentration field
λ	Taylor microscale
μ_{off}	average off time of RJA pumps
μ_{on}	average on time of RJA pumps
ν	kinematic viscosity
ν_t	eddy viscosity
ω	eddy vorticity
$\overline{\phi_c}$	mean centerline concentration
ϕ	concentration
ϕ_0	jet exit concentration
ϕ_t	scalar threshold
ϕ_{rms}	rms concentration
Ψ	quantum efficiency of dye
ρ	density

σ	standard deviation
σ_ϕ	size of the scalar patch
σ_{off}	standard deviation of off time of RJA pumps
σ_{on}	standard deviation of on time of RJA pumps
ε	turbulent kinetic energy dissipation rate
ε_ϕ	dissipation rate of scalar fluctuations
ξ	relative turbulence intensity

Acronyms

CDF	cumulative density function
FOV	field of view
HIT	homogeneous isotropic turbulence
PDF	probability density function
PIV	particle image velocimetry
PLIF	planar laser-induced fluorescence
RJA	random jet array
rms	root mean square
TNTI	turbulent non-turbulent interface
TTI	turbulent turbulent interface

Chapter 1

Introduction

1.1 Background

Scalar mixing in turbulent jets has been extensively studied in a quiescent ambient. In practical applications, such as pollutant dispersion, chemical mixing, and combustion, however, the receiving ambient, itself, is usually turbulent. Turbulence in the ambient is a parameter that greatly affects the jet dynamics and the subsequent mixing. In environmental studies, an understanding of the scalar mixing of effluent jets in a turbulent ambient can improve the available models for turbulent mixing by closely predicting the immediate and the downstream dilution of the effluent jets in a more realistic environmental context. Although there might be other influential parameters in a real environmental flow that affect the jet dynamics (such as presence of flow boundaries, mean flow advection, and density stratification), isolating and studying the effect of one parameter allows its impact to be clearly understood.

The jet in a quiescent ambient (Fig. 1.1) becomes self-similar after the zone of flow establishment (i.e. the developing core region) by breakdown of its initial vortex rings (e.g. Wygnanski and Fiedler 1969). The evolution of the jet in the downstream distance entails drawing large volumes of ambient fluid into its structure, a process called entrainment. The mass flow rate of the jet ($m = 2\pi\rho\int_0^\infty Ur\,\mathrm{d}r$, where ρ is density and U

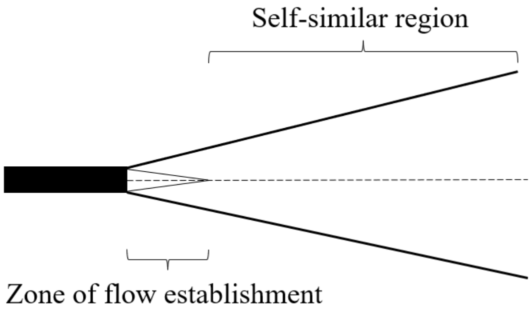

Figure 1.1: Schematic of the jet in a quiescent ambient. The dotted line shows the jet axis.

is the axial velocity) increases during the entrainment, while its momentum flow rate ($M = 2\pi \int_0^\infty U^2 r \, \mathrm{d}r$) remains constant (i.e. conservation of momentum). These parameters, which control the jet behavior (e.g. in mixing), change when the jet is exposed to the ambient turbulence.

Studies of turbulent jets and plumes have reported different effects of the ambient turbulence on the jet dilution. Early experimental studies interpreted their observations as an increased entrainment for a jet released into a turbulent ambient due to superposition of the jet-driven entrainment and turbulent dispersion, supporting the hypothesis by Wright (1994) (Ching et al., 1995; Law et al., 2001; Guo et al., 2005; Cuthbertson et al., 2006). Later arguments attributed the higher dilution in those experiments to an increasing level of ambient turbulence in the downstream direction of the jet/plume and flow blockage by the oscillating grid resulting in an abrupt dispersion at a critical downstream distance (Gaskin et al., 2004). The alternative hypothesis by Hunt (1994) argued that the jet entrainment in the turbulent ambient would be lower if the external turbulence breaks up the jet/plume structure. This was later confirmed by experiments showing a reduced entrainment of a jet in a shallow coflow (Gaskin et al., 2004), and, an axisymmetric jet (Khorsandi et al., 2013; Perez-Alvarado, 2016) and a buoyant jet (Lai et al., 2019) in approximately homogeneous isotropic turbulence (HIT). All the above experiments used Eulerian statistics (i.e. following the jet axis) to study the jet dynamics, however, the measurements have shown a meandering jet path in the turbulent ambient due to lateral

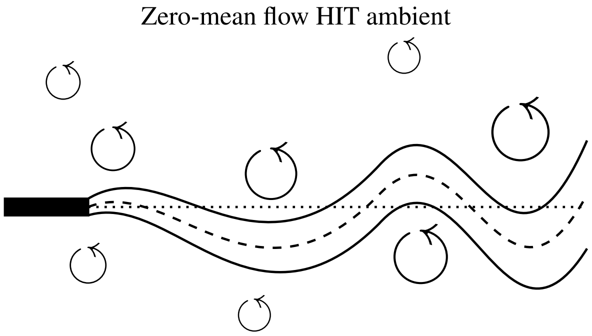

Figure 1.2: Schematic of the jet structure in the ambient turbulence. Large eddies of the HIT ambient cause the jet path to meander. The dotted line and the dashed line show the jet axis and the meandering path of the jet, respectively.

advection of the jet by large ambient eddies (Fig. 1.2). A study of a jet following its meandering path will provide more accurate observation of the jet structure and hence an improved understanding of the jet dynamics in a turbulent ambient.

Turbulent diffusion is the process of spreading and mixing of the scalar by turbulent motions. Dilution of a jet in a turbulent ambient is due concurrently to momentum-driven entrainment and turbulent diffusion by the ambient turbulence. The contribution of the turbulent diffusion dominates in the far-field of the jet, where the momentum-driven entrainment of the jet becomes negligible due to disruption and then breakdown of the jet structure. Beyond this point, the passive scalar is dispersed and mixed into the ambient only due to turbulent diffusion. Diffusion of a passive scalar from point sources (such as jets and plumes) has been studied in different turbulent flows, such as channel flow (Webster et al., 2003; Rahman and Webster, 2005; Mohaghar et al., 2020), grid-generated turbulence (Connor et al., 2018), fan-generated turbulence (Halloran et al., 2014) and uniformly sheared flow (Britter et al., 1983; Vanderwel and Tavoularis, 2014a). The study of passive scalar diffusion in approximately homogeneous isotropic turbulence (HIT) with zero mean flow, as a simplified turbulent field, can be used as a benchmark to analyze more complex flows occurring in natural and industrial contexts.

1.2 Objectives

Mixing of a turbulent jet in a turbulent ambient is encountered in many applications, such as fuel injection into a combustion engine, smoke dispersion in the atmosphere, and sewage release into waterways. The fuel/air mixing in the combustion systems controls the pollutant emission and flame stabilization (e.g. Lacarelle and Paschereit (2012)), and the mixing rate of the effluent jets determines the extent of the adverse effects of the pollutant release in the environment. Despite its importance, the diffusion and mixing of turbulent jets in a turbulent ambient are not yet fully understood. Therefore, the present research investigates the dynamics and the mixing of an axisymmetric turbulent jet in approximately homogeneous isotropic turbulence with zero mean flow, and studies the contribution of the turbulent diffusion to the jet dispersion after breakup.

The first objective of the experimental research is to study the dynamics and mixing of an axisymmetric turbulent jet in a turbulent ambient from the passive scalar field statistics. Two jet Reynolds numbers of Re = 5800 and 10600 are selected, following the previous work in our laboratory, to lie below and above the mixing transition Reynolds number, i.e. $Re = 10^4$ (Dimotakis, 2000). The ambient turbulence is generated by a random jet array (RJA) to create an approximately homogeneous isotropic turbulence (HIT) with negligible mean flow. The concentration field of the jet is measured by planar laser-induced fluorescence (PLIF) technique using a high-Sc passive scalar dye ($Sc = \nu/\mathcal{D}$, where ν and $\mathcal{D}$ are the kinematic viscosity and molecular diffusivity, respectively). The concentration measurements are carried out at axial distances of x/d = 20, 30, 40, 50, 60. The dynamics of the jet in the HIT ambient is analyzed following the meandering motion of the jet by conditioning the analysis on the jet centroid, which will remove the effect of the larger ambient eddies which advect the jet laterally and leave only the effect of the smaller ambient eddies which modify the jet entrainment. The centroidal analysis is compared to that obtained by Eulerian averaging and to that of the jet in a quiescent ambient.

The dynamics and mixing of the jet in a HIT ambient is interpreted through the study of the evolution and structure of the passive scalar field of the jet using statistics conditioned on the jet centroid. The downstream evolution, and the radial profiles of the mean and the root-mean-square (rms) concentrations, and the evolution of the rate of growth of the jet half-width are analyzed. Self-similarity and self-preservation of the centroidally-averaged passive scalar field of the jet in the HIT ambient is assessed. The entrainment into the jet in the HIT ambient is investigated through the analysis of integral volume flux, integral momentum flux and integral scalar flux of the jet. The effect of the HIT ambient on the mixing of the passive scalar within the jet is discussed in terms of jet intermittency, probability density function (PDF) and cumulative density function (CDF) of the centroidal concentrations.

The second objective of this work is to isolate and study the turbulent diffusion of an isokinetically released jet into the turbulent ambient. These results will complement the results from the first objective by analyzing how the turbulent ambient diffuses the momentumless passive scalar field, as happens for the jet in the HIT ambient once its structure is broken up. To this end, the turbulent diffusion of a point source, momentumless passive scalar in the same HIT ambient is studied. This is achieved by slowly towing the jet outlet backwards while discharging the jet fluid at the towing velocity. The temporal evolution of the passive scalar field in the HIT ambient is assessed in terms of the mean concentration, the rms concentration, the rate of width growth, the intermittency and the PDF/CDF of the instantaneous centroidal concentration. The results are compared to those of the momentumless scalar patch in a quiescent ambient, in which molecular diffusion is responsible for diffusing the passive scalar field.

1.3 Organization of the Thesis

The thesis is presented in the form of a manuscript-based thesis. Chapter 2 provides a literature review of i) the passive scalar field in turbulent jets, ii) the production of approximately homogeneous isotropic turbulence in a laboratory, iii) the effect of external turbulence on turbulent shear flows, iv) turbulent diffusion, and v) the laser-induced fluorescence technique for the measurement of passive scalar concentrations.

Chapter 3 describes the experimental facility and the measurement technique, including the jet and its traversing mechanism, the random jet array, and the planar laser-induced fluorescence (PLIF) apparatus. The calibration of the PLIF setup, and the data acquisition and post-processing methods are explained.

The results of the effect of the homogeneous isotropic turbulence (HIT) with zero-mean flow on the passive scalar field of the jet are presented in Chapter 4. This chapter has been published as a paper in Physics of Fluid in January 2022, entitled ”The dynamics of an axisymmetric turbulent jet in ambient turbulence interpreted from the passive scalar field statistics”.

Chapter 5 presents the results for diffusion of a momentumless patch of a passive scalar in the turbulent ambient. This chapter complements the results from Chapter 4 by providing a closer insight to the characteristics of the jet beyond its breakup.

Chapter 6 provides a summary of the results of the Chapters 4 and 5 and provides recommendations for future work.

Chapter 2

Literature review

In this section, a review of the following topics is presented: i) Passive scalar in turbulent jets, ii) homogeneous isotropic turbulence, iii) the effect of external turbulence on turbulent shear flows, iv) turbulent diffusion, and v) laser-induced fluorescence.

2.1 Passive scalar evolution in turbulent jets

Turbulent jets are free shear flows and occur frequently in environmental and industrial contexts, such as pollutant dispersion into the atmosphere/oceans, and combustion. A steady-state, momentum-driven, axisymmetric turbulent jet has a dominant mean momentum in the axial direction ($|\overline{V}| \approx 0.03|\overline{U}|$), and zero mean azimuthal velocity (i.e. no swirl, $\overline{W} = 0$, also $\overline{uw} = \overline{vw} = 0$, where u, v, and w are the fluctuating components of the velocity) (Pope, 2000). The lateral gradients of the mean velocity are greater than those in the axial direction, and the jet spreads radially at a relatively constant rate of $\mathrm{d}b_{1/2}/\mathrm{d}x \approx 0.1$, where $b_{1/2}$ is the velocity half-width, defined as the radial distance at which the mean axial velocity decays to half its centerline value (Wygnanski and Fiedler, 1969; Hussein et al., 1994). Therefore, Prandtl's boundary layer approximations can be applied to the Navier-Stokes equations to describe the jet behavior (Pope, 2000). Using Reynolds decomposition of the mean and fluctuating components of the velocity, $U_i = \overline{U_i} + u_i$, the continuity and axial momentum equations reduce to:

$$\frac{\partial \overline{U}}{\partial x} + \frac{1}{r}\frac{\partial (r\overline{U})}{\partial r} = 0 \tag{2.1}$$

$$\overline{U}\frac{\partial \overline{U}}{\partial x} + \overline{V}\frac{\partial \overline{U}}{\partial r} = \frac{\nu}{r}\frac{\partial}{\partial r}\left(r\frac{\partial \overline{U}}{\partial r}\right) - \frac{1}{r}\frac{\partial}{\partial r}(r\overline{uv}) \tag{2.2}$$

where $\overline{U}$ and $\overline{V}$ are the mean velocities in the axial and radial directions, respectively. x and r are the axial and the radial coordinates, and ν is the kinematic viscosity. u and v represent the fluctuating components of the axial and radial velocities, respectively, and $\overline{uv}$ is the Reynolds stress. It is noted that the mean pressure distribution can be obtained from the radial momentum equation and then substituted in equation 2.2.

The velocity field of an axisymmetric turbulent jet released into a quiescent ambient has been thoroughly investigated and its behavior is well documented (e.g. Wygnanski and Fiedler 1969; Panchapakesan and Lumley 1993a; Hussein et al. 1994; Xu and Antonia 2002, and the references therein). Experimental investigations have observed self-similar behavior in the jet after the zone of flow establishment, where initially large scale vortex rings, shed from the discharging flow, break down into multi-scale eddies, and the axial mean velocity profiles collapse onto a Gaussian curve (Wygnanski and Fiedler, 1969; Hussein et al., 1994). The rate of decay of the centerline mean velocity of an axisymmetric turbulent jet in the self-similar region varies with x^{-1} and the jet half-width, $b_{1/2}$, increases linearly with downstream distance; i.e. $b_{1/2} \propto x$.

As the jet develops in the downstream direction, a continuous range of spatial and temporal scales evolve due to the continuous transfer of turbulent kinetic energy from the larger eddies to successively smaller eddies by the means of vortex stretching. This process continues until the initial momentum is spread to such a large extent that the viscous action dominates the flow and dissipates the energy. The motion and behavior of the small scales in high Reynolds number turbulence is predicted by Kolmogorov's theory

(Kolmogorov, 1941a,b). This theory suggests that the statistics of the small scale motions in turbulent flows have a universal form, and are independent of the mean flow properties and boundary conditions. The smallest scales of the velocity field (i.e. Kolmogorov microscale), at which the turbulent kinetic energy is converted into internal energy by viscous dissipation, depend only on the kinematic viscosity (ν) and the dissipation rate of turbulent kinetic energy (ε); i.e. $\eta = (\nu^3/\varepsilon)^{1/4}$ (Kolmogorov, 1941a,b; Tennekes and Lumley, 1972; Pope, 2000).

Diffusivity of the scalar is important when studying the scalar field of a jet. The Schmidt number ($Sc = \nu/\mathcal{D}$) defines the ratio between viscous forces and diffusion, where $\mathcal{D}$ is the molecular diffusivity of the scalar in the given fluid. Similar scaling arguments to that for the velocity can predict the smallest dissipative scales of the scalar field in the turbulent flows. The smallest scale of a scalar field in low Schmidt number flows, $Sc \ll 1$, is called the Corrsin scale, $\eta_C = (\mathcal{D}^3/\varepsilon)^{1/4} = \eta Sc^{-3/4}$ (Corrsin, 1951). Similarly, the smallest scales of the scalar field for $Sc \gg 1$, the Batchelor scale, is defined as $\eta_B = \nu\mathcal{D}^2/\varepsilon = \eta Sc^{-1/2}$ (Batchelor, 1959). In high-Sc flows, $\eta_B < \eta$, indicating that the fluctuations of the scalar field are much finer than the size of the smallest eddies in the flow. Moreover, the corresponding time scale of the smallest concentration variation, $\eta_B/\overline{U}$, is much smaller than its counterpart for the finest velocity structures, and hence, a higher spatio-temporal resolution is required to resolve the smallest scalar scale in a turbulent flow.

A passive scalar is a diffusive contaminant in the fluid flow at low concentrations, which has no dynamical effect (such as buoyancy) on the fluid motion. The transport of a passive scalar in a non-reacting, incompressible flow ($\nabla . U$ = 0) is governed by the advection-diffusion equation:

$$\frac{\partial \phi}{\partial t} + U_i \frac{\partial \phi}{\partial x_i} = \mathcal{D} \frac{\partial^2 \phi}{\partial x_i^2}, \tag{2.3}$$

where ϕ is the concentration of the passive scalar, U_i is the velocity in the i direction and $\mathcal{D}$ is the molecular diffusivity of the passive scalar. The advection-diffusion equation can be non-dimensionalized using the non-dimensional variables $\hat{\phi} = \phi/\phi_0$, $\hat{t} = U_0 t/d$, $\hat{u} = U_i/U_0$, and $\hat{x} = x_i/d$, where ϕ_0 is the concentration at the jet exit, U_0 denotes the jet exit velocity, and d is the jet diameter. Substitution of the above variables into equation 2.3 results in:

$$\frac{\partial \hat{\phi}}{\partial \hat{t}} + \hat{U}_i \frac{\partial \hat{\phi}}{\partial \hat{x}_i} = \frac{1}{Pe} \frac{\partial^2 \hat{\phi}}{\partial \hat{x}_i^2}, \tag{2.4}$$

where $Pe = ReSc$ is the Peclet number ($Pe = RePr$ when the passive scalar is temperature, $Pr = \nu/\alpha$, where α is the thermal diffusivity). The evolution of the scalar concentration depends on the product of the Reynolds and Schmidt number, indicating that the scalar field of the jet is coupled to the velocity field. Using Reynolds decomposition ($U_i = \overline{U_i} + u_i$ and $\phi = \overline{\phi} + \phi'$), equation 2.3 can be rewritten in cylindrical form as

$$\frac{\partial \phi}{\partial t} + \overline{U} \frac{\partial \overline{\phi}}{\partial x} + \overline{V} \frac{\partial \overline{\phi}}{\partial r} = \mathcal{D} \Big\{ \frac{\partial^2 \overline{\phi}}{\partial x^2} + \frac{1}{r} \frac{\partial}{\partial r} \big(r \frac{\partial \overline{\phi}}{\partial r} \big) \Big\} - \frac{\partial}{\partial x} \overline{u\phi'} - \frac{1}{r} \frac{\partial}{\partial r} (r \overline{v\phi'}), \tag{2.5}$$

where $\overline{u\phi'}$ and $\overline{v\phi'}$ are the axial and radial turbulent scalar fluxes, respectively.

Experimental studies of the passive scalar field of turbulent jets in a quiescent ambient have investigated flow conditions using different experimental techniques. The measurement techniques include thermometry (Corrsin, 1951; Lockwood and Moneib, 1980), Mie scattering (Becker et al., 1967), Raman scattering (Birch et al., 1978), cold wire anemometry (Chua and Antonia, 1986; Mi et al., 2001), Rayleigh scattering (Dowling and Dimotakis, 1990; Richards and Pitts, 1993), and laser-induced fluorescence (LIF) (Dahm and Dimotakis, 1990; Law and Wang, 2000; Webster et al., 2001; Cowen et al., 2000; Fukushima et al., 2002). The jet Reynolds number and initial conditions (such as jet diameter, exit velocity and exit shape) determine the downstream statistics of the passive scalar field (Dowling and Dimotakis, 1990; Mi et al., 2001). Nevertheless, the smallest scales of the passive scalar are independent of the initial and boundary conditions, and depend only on the kinematic viscosity, the dissipation rate of the kinetic energy, and the molecular diffusivity.

The main characteristics of the passive scalar field of a turbulent jet is similar to those of the velocity field. In a quiescent ambient, after the zone of flow development, the mean profile of the passive scalar follows a Gaussian curve, $\overline{\phi}/\overline{\phi_c} = \exp\{-K(r/x)^2\}$, where K is a shape constant which varies between 55.3 and 62, as found for both experimental and direct numerical simulation (DNS) data (Fischer et al., 1979; Papanicolaou and List, 1988; Dowling and Dimotakis, 1990; Lubbers et al., 2001; Fukushima et al., 2002). The mean concentration profile becomes self-similar after the zone of flow development, which has a length of approximately x/d = 20 (Wilson and Danckwerts, 1964; Becker et al., 1967; Birch et al., 1978; Dowling and Dimotakis, 1990; Panchapakesan and Lumley, 1993b). In the self-similar region, the mean centerline concentration, $\overline{\phi_c}$, decays inversely with the downstream distance, such that $\overline{\phi_c} = \kappa_\phi \phi_0 (\frac{x-x_0}{d})^{-1}$, where κ_ϕ and x_0 denote the decay constant and the position of the virtual origin, respectively (Wilson and Danckwerts, 1964; Dowling and Dimotakis, 1990; Law and Wang, 2000; Webster et al., 2001). The decay constant, κ_ϕ, depends slightly on Reynolds number and on the initial conditions (Mi et al., 2001), and its value ranges between $4.48 < \kappa_\phi < 5.59$ (Fischer et al., 1979; Dowling and Dimotakis, 1990). The virtual origin, however, depends strongly on the Reynolds number and the initial condition of the jet (Fukushima et al., 2002). The concentration half-width, $b_{\phi,1/2}$, grows linearly with the downstream distance, $b_{\phi,1/2}(x) = S(x - x_0)$, where S is the spreading rate of the scalar field in the jet (Fischer et al., 1979; Webster et al., 2001; Fukushima et al., 2002). Experimental data show that S is independent of Reynolds number, and it varies between $0.101 < S < 0.156$ (Fischer et al., 1979). The rms concentration profile has a double-peaked shape with its maximum at $r/x \approx$ 0.1, corresponding to the inflection point of the mean concentration profile, where the maximum concentration gradient occurs (Papanicolaou and List, 1988; Webster et al., 2001). The rms profiles become self-similar downstream of the first-order properties, i.e. by x/d = 40 (Wilson and Danckwerts, 1964; Lockwood and Moneib, 1980).

It is worthwhile to compare the evolution of the concentration and the velocity fields of a turbulent jet in a quiescent ambient. The mean concentration decays faster than the mean axial velocity, i.e. $\kappa_u > \kappa_\phi$ (Fischer et al., 1979), and the spreading rate of the concentration half-width is greater than its counterpart in the velocity field (Fischer et al., 1979). Faster transport of the concentration compared to the momentum is attributed to the presence of the pressure gradient term in the Navier-Stokes equation that suppresses the transport of momentum. Also, turbulent Schmidt number, defined as $Sc_t = \nu_t/\mathcal{D}_t$, is in general smaller than unity in the shear layers because eddy diffusivity, $\mathcal{D}_t$, is greater than eddy viscosity, ν_t (Chua and Antonia, 1990; Lubbers et al., 2001). Particularly, at the edges, $\mathcal{D}_t$ is almost twice as big as ν_t, indicating that the scalar is transported faster than the momentum throughout the turbulence field (Westerweel et al., 2009).

2.1.1 Entrainment and mixing in turbulent jets

Mixing of a passive scalar in a turbulent jet has been widely studied in a quiescent ambient (e.g. Corrsin and Uberoi (1950); Becker et al. (1967); Chevray and Tutu (1978); Dahm and Dimotakis (1987); Dowling and Dimotakis (1990); Catrakis and Dimotakis (1996); Law and Wang (2000); Fukushima et al. (2002); Dimotakis (2005)). As initially described by Eckart (1948), mixing occurs via three relatively distinct and successive processes: entrainment, turbulent stirring, and molecular mixing (Dimotakis, 2000). First, the eddies draw the ambient fluid into the turbulent region. Then, the scalar is advected throughout the flow domain by means of the turbulent stirring (i.e. vortex stretching) and the surface area of the flow interface distorts and increases. This process continues until the scalar is spread very thinly to the point that small-scale diffusive action dominates the flow and mixes the scalar into the ambient fluid. Mixing at the molecular level will be further discussed in Sec.2.4. In this section, the entrainment process and its mechanisms for a jet in a quiescent ambient will be discussed.

The entrainment hypothesis was first introduced by Morton et al. (1956) following a note by Taylor in 1949. Assuming self-similarity, the entrainment is described as a continuous, multi-scale transport of irrotational fluid across the turbulent non-turbulent interface (TNTI), through which it acquires mass and momentum, and ultimately irreversibly mixes into the turbulent region at the molecular level (Turner, 1986; Sreenivasan et al., 1989; Holzner et al., 2009; Mistry et al., 2016). With entraining the ambient fluid, the jet expands radially and its mass flow rate increases, while its axial velocity decreases due to conservation of momentum. Total entrainment is quantified with a global entrainment velocity E_v, the rate at which the ambient fluid flows towards the turbulent core. E_v is proportional to a large-scale characteristic velocity, such as the centerline velocity, $E_v = \alpha\overline{U}$, and is independent from the small scale turbulent parameters; i.e. energy dissipation rate, ε, and viscosity, ν. The entrainment coefficient, α, is $\mathcal{O}(0.1)$ (but not a universal constant) and varies between $0.065 < \alpha < 0.080$ for jets in a quiescent ambient depending on initial conditions (Fischer et al., 1979; Hossain and Rodi, 1982; Turner, 1986).

Although the entrainment hypothesis estimates the entrainment velocity by relating it to the mean axial velocity, it does not provide information about the entrainment mechanisms. The significance of different-sized eddies (i.e. ranging between the integral scale to the Kolmogorov micro-scale) in the entrainment process has been described by two principle hypotheses. The equilibrium hypothesis, proposed by Townsend (1956), ascribes the entrainment mainly to the large scale eddies, referred to as engulfment, which is an inviscid process. During the engulfment, the large eddies envelop parcels of irrotational fluid and draw them into the turbulent region, where they subsequently acquire mass, momentum and vorticity. The engulfment leaves large volumes of unmixed fluid within the jet boundaries, for which evidence has been obtained in some experimental studies (Brown and Roshko, 1974; Dahm and Dimotakis, 1987; Dimotakis, 2000).

On the other hand, several experiments and numerical simulations have observed insignificant volumes of unmixed fluid within the turbulent fluid, suggesting an alternate entrainment mechanism in agreement with the superlayer hypothesis proposed by Corrsin and Kistler (1955) (Mathew and Basu, 2002; Westerweel et al., 2005, 2009; da Silva and Taveira, 2010; Holzner and Lüthi, 2011; Wolf et al., 2012; Taveira et al., 2013). According to the superlayer hypothesis, a viscous process carried out by small-scale eddies at the TNTI is responsible for the entrainment. During this process termed nibbling, initially irrotational fluid acquires vorticity via viscous diffusion of vorticity, with no or negligible enstrophy production (Corrsin and Kistler, 1955; Phillips, 1955). Similarly, scalar is transported to the entrained fluid through molecular diffusion. Although viscous diffusion and molecular diffusion are slow processes, they occur along the contorted surface of the TNTI, allowing the exchange of the scalar and momentum across the TNTI (Sreenivasan et al., 1989; Mathew and Basu, 2002). The small-scale motions at the TNTI contribute to almost 90% of the total jet mass flux of a turbulent jet in a quiescent ambient (Westerweel et al., 2005, 2009).

In the past decade, studying the processes occurring at the TNTI has improved the understanding of the entrainment mechanisms and mixing in the turbulent shear flows. The TNTI studies include those of wakes (Bisset et al., 2002), boundary layers (Borrell and Jiménez, 2016), jets (Westerweel et al., 2009; Mistry et al., 2016; Kohan and Gaskin, 2020), mixing layers (Jahanbakhshi and Madnia, 2016), and plumes (Burridge et al., 2017). It is shown that despite similarities in the properties of the TNTI and the flow passing across it, the characteristics of these interfaces are not universal and depend on the flow type (da Silva et al., 2014).

2.2 Homogeneous isotropic turbulence

The dynamics of a jet and its dilution depends on the flow parameters (i.e. mass flow rate, momentum flow rate and buoyancy) and on environmental parameters, such as presence of a mean flow, density stratification, turbulence and boundaries (Fischer et al., 1979). Turbulence in the ambient is in general inhomogeneous and anisotropic. However, the study of shear flows in approximately homogeneous isotropic turbulence (HIT) allows for analysis in a simplified laboratory context. In addition, approximately homogeneous isotropic turbulence is often used to study the fundamental characteristics of turbulence, such as internal intermittency and spectral energy transfer. Although homogeneous isotropic turbulence is a relatively simple flow, it is challenging to generate in a laboratory context due to a mean velocity gradient required for initial production of turbulent kinetic energy (Perez-Alvarado et al., 2016).

Despite the challenges, and the fact that turbulence production is always associated with secondary flow generation (Variano et al., 2008), researchers have used different methods to create the closest approximations to HIT, such as oscillating grids (De Silva and Fernando, 1994) active/passive grids (Mydlarski and Warhaft, 1996; Kang et al., 2003; Lavoie et al., 2007; Bodenschatz et al., 2014), loudspeakers (Hwang and Eaton, 2004; Webster and Brathwaite, 2004), rotating elements (Douady et al., 1991; Liu et al., 1999; Fallon and Rogers, 2002; Friedman and Katz, 2002), and random jet arrays (Variano and Cowen, 2004; Lavertu et al., 2008; Khorsandi et al., 2013; Carter et al., 2016; Perez-Alvarado et al., 2016). Grid-generated turbulence has been the most commonly used HIT flow in the literature (e.g. Jayesh and Warhaft (1992); De Silva and Fernando (1994); Comte-Bellot and Corrsin (1966); Ertunç et al. (2010); Krogstad and Davidson (2011); Valente and Vassilicos (2011), and references therein). With advances in development of active grids (Makita, 1991; Mydlarski and Warhaft, 1996) and low-viscosity fluid wind tunnels (Bodenschatz et al., 2014), channel flows can achieve relatively high Reynolds numbers (a recent review by Mydlarski (2017)).

Oscillating grids were the first method used to obtain three-dimensional HIT with nearly zero-mean-flow with one or two paralell grids oscillating normal to their plane (Thompson and Turner, 1975; McDougall, 1979; Brumley and Jirka, 1987; De Silva and Fernando, 1994; Villermaux et al., 1995; Srdic et al., 1996; Ott and Mann, 2000; McKenna and McGillis, 2004; Blum et al., 2010). Despite optimizing mesh size, stroke and frequency of the oscillating grids, the generated turbulence still suffered from large mean flows, whose magnitude ranged from a minimum of 25% of rms velocity to maximums of 60% and 30% of the rms velocities of single and double-sided grids, respectively. In addition, mechanical systems required to oscillate the grids were large for high Reynolds number flows, adding costs and complications to the projects.

In another method achieving nearly zero-mean flow HIT, loudspeakers symmetrically pointing towards the center of a test chamber were used (Hwang and Eaton, 2004; Webster and Brathwaite, 2004; Warnaars et al., 2006; Lu et al., 2008; Goepfert et al., 2010; Sabban and van Hout, 2011; Chang et al., 2012; Sabban et al., 2017). The loudspeakers generate pulsed synthetic jets by pushing fluid through circular orifices to induce vortex rings. Flow quality is improved compared to the oscillating grids as it has very low (and approximately isotropic) mean flow. However, the HIT flow is confined to a small central region of the chamber. For example, 32 loudspeakers generated an approximately zero-mean-flow homogeneous isotropic turbulence with a relatively high Taylor Reynolds number, Re_λ = 480, but the extent of the isotropic flow was limited to a 10-cm-diameter central region (Chang et al., 2012).

Rotating elements, such as propellers (Fallon and Rogers, 2002; Birouk et al., 2003; De Jong et al., 2009; Zimmermann et al., 2010), rotating grids (Liu et al., 1999; Friedman and Katz, 2002), and counter-rotating disks (Douady et al., 1991; Fauve et al., 1993; Maurer et al., 1994; Cadot et al., 1995; Aumaitre et al., 2000; Mordant et al., 2001; Voth et al., 2002) have also been used to produce zero-mean-flow turbulence. Symmetrically placed counter-rotating propellers (pointing towards the center of a chamber) generate a flow similar to that generated by the loudspeakers. These methods can achieve moderate to high Taylor Reynolds numbers, Re_λ = 290 and 970 in Liu et al. (1999) and Voth et al. (2002), respectively. However, the isotropic homogeneous flow is usually limited to a central region of a few centimeters diameter. The rotation of the elements generates a cylindrical region of turbulence (causing anisotropy) with its axial extension depending on the size of the tank (Machicoane et al., 2014).

Initially proposed by Variano and Cowen (2004), random jet arrays (RJAs) have become progressively more popular (Variano et al., 2008; Lavertu et al., 2008; Khorsandi et al., 2013; Bellani and Variano, 2014; Carter et al., 2016; Perez-Alvarado et al., 2016; Esteban et al., 2019; Lai et al., 2019; Berk and Coletti, 2021). A single RJA is a planar array of jets randomly and independently turned on and off by an algorithm to produce turbulence downstream of the RJA. The single-RJA-generated turbulence is approximately homogeneous, with an unavoidable decay in the direction normal to the RJA plane, and negligible mean flow (less that 10% of the rms velocities in all directions) over a large volume (Variano et al., 2008). Relatively high Reynolds numbers can be achieved (Re_λ = 314 in Variano et al. (2008)) and the isotropy of the flow is of the same order as that of grid-generated wind tunnel turbulence. The isotropy, defined as the ratio of rms velocities, $u_{\alpha-rms}/u_{\beta-rms}$ is less than one in single-plane RJAs (0.81 in Variano and Cowen (2004), 0.66 in Lavertu (2006), 0.79 in Variano et al. (2008), and 0.71 in Khorsandi et al. (2013)) due one-sided forcing (Variano et al., 2008), which can be reduced using two parallel RJAs.

Double-RJAs (Bellani and Variano, 2014) generate a better approximation (compared to single-RJAs) of homogeneous isotropic turbulent flow with negligible mean flow in relatively large volumes (Carter et al., 2016; Carter and Coletti, 2017; Esteban et al., 2019; Berk and Coletti, 2021). In this method, two symmetrically placed RJA planes (separated by a distance) face each other improving the homogeneity and isotropy of the flow, reaching 0.95 - 0.99 isotropy in the central region (Bellani and Variano, 2014). Relatively high Taylor Reynolds numbers can be achieved (up to Re_λ = 580 in water, Esteban et al. (2019), and Re_λ = 470 in air, Carter et al. (2016)), while the mean flow is negligible (less than 10% of the rms velocity) (Bellani and Variano, 2014). The profile of the turbulent kinetic energy is almost flat at the symmetry plane, and the homogeneous isotropic region extends beyond one integral length scale from the center (Bellani and Variano, 2014; Carter et al., 2016; Esteban et al., 2019). A maximum volume of 0.4×0.4×0.2 m^3 in water and 0.5×0.7×0.4 m^3 in air have been achieved to date, by Bellani and Variano (2014) and Carter et al. (2016), respectively.

In a recent study, Cazaubiel et al. (2021) introduced a novel technique to generate three-dimensional HIT ambient with zero mean flow using remotely driven, small magnetic particles to randomly force the fluid volumes in space and time. The turbulence field was generated in a $11.5 \times 11.5 \times 9$ cm^3 chamber and its level of homogeneity and isotropy was comparable to those of direct numerical simulation. The randomness of this method is flexible to be in space and time, or, in space or in time only, and it is deemed to be an appropriate technique to study large-scale properties of 3D turbulence (i.e., scales larger than the injection scale).

2.3 Effect of HIT on turbulent shear flows

The turbulence in the ambient fluid can be expected to have a significant effect on the entrainment and mixing processes in jet. In the near field, dilution is predominantly due to fluid entrained by the jet momentum, while external turbulence has a minimal effect. However, in the far field, the mean axial velocity has decayed and the ambient turbulence determines the rate (and the mechanism) of the jet entrainment and mixing. In this region, the dilution occurs mainly due to turbulent diffusion in the ambient turbulence (Wright, 1994; Gaskin et al., 2004).

Previous studies have highlighted the significance of the turbulence intensity and integral length scale of the background turbulence on the shear flows (Hancock and Bradshaw, 1989; Ching et al., 1995; Gaskin et al., 2004; Eames et al., 2011b; Kankanwadi and Buxton, 2020). Given the similarities between the turbulent shear flows (e.g. turbulent boundary layers, turbulent wakes, and turbulent jets), the effect of external turbulence on their flow characteristics should be comparable. The intensity of external turbulence for boundary layers and wakes is defined as the ratio of the rms of the external velocity fluctuations to the mean free stream velocity, u/U_∞. When a high-intensity external turbulence is imposed on a turbulent boundary layer, the irregularity of the interface between the boundary layer and the free stream increases (Hancock and Bradshaw, 1989). The large-scale turbulent structures disturb the boundary layer and increase the streamwise velocity fluctuations. While the outer part of the boundary layer undergoes a higher mixing, the log-law region persists against the intensities of 10-20%. However, with increasing external turbulence intensity, the large scale structures penetrate deeper into the log-law region and tend to modulate the motion of the small-scale fluctuations (Thole and Bogard, 1996; Hutchins and Marusic, 2007; Dogan et al., 2016). Conditional statistics showed that the low-frequency (i.e. large-scale) structures of the free-stream turbulence penetrate the logarithmic layer and enhance the energy of the outer large-scale motions in the boundary layer (You and Zaki, 2019).

Similar effects of increased turbulence levels are observed inside wakes. As the external turbulence is entrained into the wake, the energy transfer from the mean flow to the fluctuating components increases and reduces the mean velocity deficit of the wake (Legendre et al., 2006; Amoura et al., 2010; Pal and Sarkar, 2015). Two power-law decay regions are observed for the mean centerline velocity: a x^{-1} decay in the near wake region similar to the laminar case, followed by a x^{-2} decay starting as the velocity defect becomes of the order of the rms fluctuating velocity of the free stream flow (Eames et al., 2011a). The starting point of the x^{-2} decay shifts closer to the body with an increase in the external turbulence levels. The length of the recirculating region of the wake is reduced in an isotropic turbulent ambient (Bagchi and Balachandar, 2004; Amoura et al., 2010). The width of the wake grows diffusively with distance, $x^{1/2}$, when the wake width is smaller than the integral length scale of the turbulence, while its growth rate increases to x^1 once the integral length scale of the ambient turbulence becomes larger than the wake width (Legendre et al., 2006; Eames et al., 2011a,b).

In wakes, the ambient turbulence intensity has been shown to be the dominant factor compared to the integral length scale (Pal and Sarkar, 2015; Kankanwadi and Buxton, 2020). In a recent study, Kankanwadi and Buxton (2020) used grid-generated turbulence to systematically study the influence of the two parameters on the entrainment into the far wake of a cylinder. Conditional statistics at the interface revealed that despite the presence of turbulent rotational fluid on both sides, there is still a well-defined enstrophy jump at the wake/ambient interface. The background turbulence increased the shear rate at the interface when the turbulence intensity was not too high (and hence owerpowering the wake). The surface area of the interface increased with increasing the turbulence intensity of the ambient turbulence. However, the entrainment flux showed a net reduction compared to the unforced wake, due to large, intermittent (but infrequent) detrainment events that reduce the entrainment despite the increased surface area. Also, it was argued that the turbulent/turbulent entrainment is a multi-scale phenomenon because not only the large, energy containing eddies in the background affect the entrainment, but all length scales are involved in the process.

There are two hypotheses on the effect of external turbulence on the jet evolution. The first hypothesis suggests a superposition of the jet dilution and turbulent diffusion in the near-field region. It was first introduced by Wright (1994), who proposed adding a separate term to the classic entrainment function (Morton et al., 1956) ($E = 2\pi\alpha b u_m$, where b is the jet half-width and u_m is a characteristic velocity) to account for the entrainment increase due to the external turbulence. The hypothesis suggests that the dilution is enhanced with increasing levels of external turbulence. In experiments that claimed to support this hypothesis, an abrupt increase in the jet dispersion is observed at a critical distance from the nozzle exit, where the jet disruption occurs. It is claimed that the external turbulence intensity, defined as the ratio of the rms turbulent ambient velocity to the turbulent jet rms velocity, determines this break-up position (Guo et al., 2005). Similar observations of the enhanced dilution of linear plumes and jets in the presence of external turbulence generated by an oscillating grid, supported Wright's hypothesis (Ching et al., 1995; Law and Wang, 2000). However, the conclusions drawn from these experiments was questioned as, in the experimental set up (with the jet flowing towards the oscillating grid), external turbulence increased in the downstream direction and the oscillating grid effectively blocked the flow. It was argued that the reason for an abrupt increase in the jet spreading and entrainment rate was the blockage of the flow by the oscillating grid resulting in an accumulation of mass near the oscillating grid (Gaskin et al., 2004; Khorsandi et al., 2013).

A second hypothesis on the effect of background turbulence explains, that since the mass and momentum flow rate of the jet induces the entrainment, any influence that tends to break up the jet into detached eddies reduces the dilution (Hunt, 1994). This theory argues that if the rms velocity of the background turbulence is greater than the rms velocity of the jet, the external turbulence reduces the entrainment. When the jet turbulence is lower than the ambient turbulence, the self-similar structure of the jet is disrupted, and the entrainment reduces significantly. The dilution then occurs mainly due to turbulent diffusion at a rate dependent on the ambient turbulence level (Gaskin et al., 2004; Cuthbertson et al., 2006; Lavertu et al., 2008; Khorsandi et al., 2013; Perez-Alvarado, 2016; Lai et al., 2019). Findings by Gaskin et al. (2004), on a plane jet in a shallow co-flow gave the first support to this hypothesis. In those experiments, the background turbulence was increased using ribs across the channel bed. Measurements showed faster decay rates for the velocity and concentration, and a decreased entrainment throughout the jet due to the background turbulence. However, it was likely that the periodic nature of the background turbulence (caused by the ribs), as well as the mean-flow advection and shallowness of the channel, further affected the turbulent jet structure (Khorsandi et al., 2013). Thus, the development of an approximately homogeneous isotropic background turbulence was suggested to reduce the variation in the external turbulence in the study of turbulent jets.

The effect of background turbulence on the velocity field of turbulent axisymmetric jets was studied by Khorsandi et al. (2013). A random jet array (RJA) generated an approximately homogeneous isotropic turbulence (with zero mean flow) and was oriented perpendicular to the jet axis, to ensure a constant level of turbulence intensity along the axis of the jet. The background turbulence increased the rms velocity within the jet, and destroyed the self-similarity of the jet. The mean axial velocity was decreased relative to the jet in a quiescent background, which resulted in lower mass flow rates. However, mean radial velocities increased, especially at the edges of the jet. The decay rate of the mean velocity and the jet half-width increased, and the increase was more intense for higher turbulence intensity levels. Consistent with the works of Hunt (1994) and Gaskin et al. (2004), a lower entrainment rate was reported due to the reduced mass flow rate. The break up location of the jet was found to be a function of the ratio of the local turbulence intensity level relative to that of the jet, which shifted towards the jet exit with increasing relative intensity of the background turbulence.

Perez-Alvarado (2016) carried out further measurements, but of the concentration field, of turbulent jets in the presence of external turbulence. The findings revealed similar results for the jet concentration as previously found for the velocity statistics in the presence of background turbulence. However, the main difference was the wider concentration profiles compared to those of the velocity, which was attributed to the turbulent transport of the scalar in the radial direction due to the meandering of the jet and due to turbulent diffusion. In the presence of background turbulence, the mean centerline concentration of the jet decreased with a steeper power-law decay as compared to a jet in a quiescent background. However, slightly higher concentrations were measured near the edges of the jet. The concentration profiles became wider, indicating a larger concentration half-width. Higher rms concentrations occurred due to the meandering of the jet, and the intermittency of the scalar field increased. Therefore, the probability of low concentrations increased, while the probability of high concentrations decreased compared to the quiescent case. A bimodal distribution of the concentration PDFs of the jet in the turbulent background compared to its Gaussian distribution in quiescent case, was due to a very high number of very low concentrations. It was hypothesized that the background turbulence affects the entrainment process, and its effect become more dominant with increasing the downstream distance. Finally, at a specific downstream distance (i.e. the breakup location) the jet is destroyed and the scalar mixing then occurs only due to turbulent diffusion.

In a recent study, Lai et al. (2019) proposed a second-order integral model for the mixing of buoyant jets in approximately homogeneous isotropic turbulence. A random jet array, similar to that in Khorsandi et al. (2013) and Perez-Alvarado (2016), was used to generate the background turbulence, and a range of pure to buoyant jets were studied using PIV. The jet followed a meandering path and a critical length was determined beyond which the jet mixing was significantly affected by the ambient turbulence, or even broke up. Similar to previous studies, the jet decayed faster than than that in the quiescent ambient and the width growth was faster (spreading rate of 0.18). An integral jet model was proposed based on the conservation of mass, total momentum and buoyancy fluxes, and the downstream decay function of the jet mean momentum. The model predicted a faster width growth of the jet once the turbulence intensity ratio reached a critical level (similar to that observed in Ching et al. (1995)). Unlike the buoyant jets in the quiescent ambient, in which the turbulent momentum flux has a minimal contribution to the total momentum flux (about 10%) (Papanicolaou and List, 1988), the momentum flux of the buoyant jets in a HIT ambient was found to be conserved only if the second-order turbulence statistics were accounted for. A lower volume flux (and hence a lower entrainment) was predicted for the jet in the HIT ambient, consistent with the previous studies (Hunt, 1994; Gaskin et al., 2004; Khorsandi et al., 2013; Perez-Alvarado, 2016).

2.4 Turbulent diffusion

Diffusion, in general, defines the process of scalar transport in a fluid from a region of high concentration to one of a lower concentration. Based on the means of this transport, diffusion can be categorized as molecular diffusion or turbulent diffusion. The diffusive flux of a scalar by molecular diffusion is described by Fick's second law, $\frac{\partial \phi}{\partial t} = \mathcal{D}\frac{\partial^2 \phi}{\partial x_i^2}$. For a passive scalar in a flow, advection of the fluid also contributes to diffusion, governed by the advection-diffusion equation (eq. 2.3).

In turbulent flows, a second mechanism for scalar transport is carried out by turbulent motions (i.e. eddies), which is important in pollutant dispersion and heat transport in atmosphere and oceans, and mixing process in engineering flows, such as combustion. Turbulent diffusion is structurally similar to molecular diffusion, but entails larger scales due to the turbulent fluid motion (with scales ranging from the Taylor micro-scale to the integral length scale). It occurs more rapidly than the molecular diffusion. If a scalar is non-reactive and in small concentrations, the Reynolds-averaged advection-diffusion equation governs the problem

$$\frac{\partial\overline{\phi}}{\partial t} + \underbrace{\overline{U_i}\frac{\partial\overline{\phi}}{\partial x_i}}_{\text{advection}} = \underbrace{\mathcal{D}\frac{\partial^2\overline{\phi}}{\partial x_i^2}}_{\text{molecular diffusion}} + \underbrace{\frac{\partial(-\overline{\phi' u_i})}{\partial x_i}}_{\text{turbulent diffusion}} , \tag{2.6}$$

where $\overline{\phi' u_i}$ is the turbulent scalar flux vector (or concentration-velocity covariance). Analysis of this equation is, in general, concerned with closure models for the turbulent scalar flux vector, mainly in terms of mean concentration (Roberts and Webster, 2002), so that the equation 2.6 can be solved for $\overline{\phi}$. The first-order gradient transport model (Arya, 1999) is the most commonly used closure for the turbulent scalar flux,

$$-\overline{\phi' u_i} = \mathcal{D}_{ij}\frac{\partial\overline{\phi}}{\partial x_j} \tag{2.7}$$

where $\mathcal{D}_{ij}$ is the turbulent diffusivity (or eddy diffusivity) tensor. This model estimates the turbulent scalar flux based on two assumptions; (i) the characteristic length scale of the scalar (e.g. concentration half-width) is much larger than the integral length scale of the turbulence, and (ii) the flow properties in the turbulence length scale are approximately homogeneous (Corrsin, 1975). Knowledge of all nine components of $\mathcal{D}_{ij}$ is difficult, as it requires simultaneous measurement of the local magnitude and directions of the mean concentration gradient and the turbulent scalar flux. This tensor was measured empirically by Vanderwel and Tavoularis (2014a) for a slender plume in a uniformly sheared turbulent flow, discussed in details in section 2.4.

In the pioneering study of turbulent diffusion by Taylor (1921), he argued that the mean square displacement (and therefore turbulent dispersion) of fluid elements is related to the Lagrangian velocity autocorrelation function. This assumes that a fluid element is a sufficiently small volume of fluid that moves with flow, without significant deformation over the time of interest. The fluid element is labeled with a scalar quantity, which remains unchanged as the element moves through the fluid, i.e. the molecular diffusivity of the scalar is assumed to be zero. For one-dimensional motion of an individual fluid element released from a point source in a stationary isotropic turbulence, Taylor's argument states that

$$\overline{X^2}(t) = 2\overline{\tilde{u}^2}\int_0^t (t-\tau)R(\tau)\,d\tau \tag{2.8}$$

where X is the displacement of a fluid element in time t, $\tilde{u}$ represents the Lagrangian velocity fluctuations ($\tilde{U} = dX/dt = \overline{\tilde{U}} + \tilde{u}$), and $R(\tau)$ is the auto-correlation function of Lagrangian velocity, $\tilde{U}$. Using equation 2.8, rate of dispersion (termed by Vanderwel) (i.e. diffusivity - Britter, Hunt 1983), D, is defined as

$$D(t) = \frac{1}{2}\frac{d\overline{X^2}(t)}{dt} = \overline{\tilde{u}^2}\int_0^t R(\tau)\,d\tau. \tag{2.9}$$

Depending on time t, two regimes of diffusion would occur due to turbulent motions; turbulent convection (i.e. turbulent advection) in shorter times and turbulent diffusion for larger time limits (Taylor, 1921; Warhaft, 1984; Anand and Pope, 1985). At sufficiently short times, $R(\tau)$ is approximately 1, and equations 2.8 and 2.9 can be simplified as

$$\overline{X^2}(t) \approx \overline{\tilde{u}^2}t^2 \quad \text{and} \quad D(t) \approx \overline{\tilde{u}^2}t \quad \text{for} \quad \mathcal{D}/\overline{v^2} \ll t \ll T \tag{2.10}$$

where T is the Lagrangian integral timescale of the turbulence defined as $\int_0^t R(\tau)\,d\tau$, t is the "flight-time" since the release (Lepore and Mydlarski, 2011), and $\overline{v^2}$ is the mean-square transverse velocity fluctuation. Equation 2.10 implies that for shorter times, the rate of dispersion grows linearly with time. For longer times, however, R tends to zero, and it is of interest to assume a large time (e.g. $t \gg T$), beyond which the velocity of the fluid particle has no correlation with its velocity at the beginning. In this case, $\lim_{t\to\infty} R(\tau)d\tau$ approaches some finite value. Therefore, equations 2.8 and 2.9 can be rewritten as

$$\overline{X^2}(t) \approx 2\overline{\tilde{u}^2}tT \quad \text{and} \quad D(t) \approx \overline{\tilde{u}^2}T \quad \text{for} \quad t \gg T \tag{2.11}$$

implying that the rate of dispersion would eventually reach an asymptote, which depends only on the Lagrangian integral timescale of the turbulence and the variance of the Lagrangian velocity fluctuation (Vanderwel and Tavoularis, 2014a). The product $D(T) = \overline{\tilde{u}^2} T$ is known as Taylor diffusivity.

It is noted that although equation 2.8 gives a measure of the spatial distribution of the mean concentration field, $\overline{\phi(x,t)}$, it does not take into account the effect of molecular diffusion, a process to which all real contaminants are subject. Saffman (1960) extended Taylor's result to include the effect of the molecular diffusion

$$\overline{X^2}(t) = 2\overline{\tilde{u}^2} \int_0^t (t-\tau) R(\tau)\, d\tau + 2\mathcal{D}t \tag{2.12}$$

where $\overline{X^2}$ is now the mean square separation of the molecules, and $R(\tau)$ is the correlation function of the flow velocity along molecular trajectories. Equation 2.12 suggests that the dispersion of a passive scalar in a stationary and homogeneous turbulent field can be expressed in terms of a scalar auto-correlation function. Batchelor (1952) proposed that the diffusivity (D) is an increasing function of the mean square displacement ($\overline{X^2}$) of a pair of marked fluid particles (elements) and not of the actual displacement (X). The mean square displacement approaches a limit with increasing averaging time, because only the eddies comparable to $\overline{X^2}$ are effective in increasing the displacement (Richardson, 1926).

It is important to distinguish between scalar transport by turbulent eddies and that by molecular motion. Initially, it was assumed that the the effects of the two processes are statistically independent, and are superimposed at large enough times and thereby enhance scalar dispersion/diffusion (Townsend, 1954). Later, Saffman (1960) argued that in a stationary homogeneous turbulent field, the interaction between the molecular and the turbulent diffusion reduces the overall diffusion compared to the case if they acted independently and were linearly additive. This was attributed to the difference between the convective velocities of different eddies, while the convective speed of the scalar was in general less than the (originally matching) speed of the turbulent eddies. The interaction increases with molecular diffusivity ($\mathcal{D}$) and eddy vorticity (ω), and at large Reynolds numbers, the direct effect of the molecular diffusion is smaller than the interaction term.

At high Reynolds and high Peclet ($Pe = Re\, Sc = Ud/\mathcal{D}$) number flows, the mean concentration is mainly transported by turbulent diffusion (Saffman, 1960), except very close to a small source or to a boundary. Moreover, in such flows, the mean rate of dissipation of scalar fluctuations ($\overline{\varepsilon}_\phi = \mathcal{D}\overline{(\frac{\partial \phi'}{\partial x_i})^2}$, where $\overline{\phi'^2}$ is the scalar variance) is independent of molecular processes; that is, $\overline{\varepsilon}_\phi$ depends on the existence of molecular diffusion, but its magnitude is controlled by turbulent diffusion (Sawford, 2001). Although at large-Re flows, the scalar is mainly transported by the mean and turbulent velocity field and the molecular diffusion is less dominant, its contribution cannot be neglected and plays a controlling role in cases involving chemical reactions, boundaries, and buoyancy effects (e.g. Chatwin and Sullivan 1979). Uberoi and Corrsin (1952) argued that the role of the molecular diffusion is to increase mean square displacement by $\overline{X^2} = 2\mathcal{D}t$ in very small flight-times, $t \ll \mathcal{D}/\overline{v^2}$. In other words, molecular diffusion dominates the initial stages of dispersion (i.e. initiates dispersion) and as the time t grows and once the mean square displacement is sufficiently large (e.g. of the order of the smallest eddy sizes), turbulent eddies take over the dispersion process (Sawford, 2001).

Turbulent diffusion studies can be categorized either by source type or turbulent flow characteristics. Examples include experimental studies on point source plumes in channel flow (Webster et al., 2003; Rahman and Webster, 2005; Mohaghar et al., 2020), grid turbulence (Connor et al., 2018), fan-generated flow (Halloran et al., 2014) and uniformly sheared flow (Britter et al., 1983; Vanderwel and Tavoularis, 2014a), line source in channel flow (Lavertu and Mydlarski, 2005; Lepore and Mydlarski, 2011; Germaine et al., 2014), grid turbulence (Taylor, 1935; Uberoi and Corrsin, 1952; Townsend, 1954; Warhaft, 1984; Anand and Pope, 1985; Stapountzis et al., 1986; Nedić and Tavoularis, 2016), and uniformly sheared flow (Tavoularis and Corrsin, 1981; Karnik and Tavoularis, 1989).

Scalar dispersion in homogeneous isotropic turbulence has been theoretically studied by Durbin (1980) and Sawford and Hunt (1986) using two-point dispersion models.

In the experimental studies, a practical approach to measure turbulent diffusion is to study the growth rate of the plume/puff in the turbulent flow, and relate it to an apparent turbulent diffusivity, $\mathcal{D}_t$. Early studies of turbulent diffusion behind a thermal line source in (homogeneous and isotropic) grid turbulence (i.e. uniform turbulent flow according to Townsend 1954) demonstrated that the mean scalar (i.e. temperature) profile was well represented by a Gaussian curve (Taylor, 1935; Uberoi and Corrsin, 1952; Townsend, 1954). Furthermore, the mean scalar field was found to evolve differently in three regions where different diffusion mechanisms were dominant; molecular diffusion, turbulent convection, and turbulent diffusion (Warhaft, 1984; Anand and Pope, 1985; Stapountzis et al., 1986). At very short flight-times, $t \ll \mathcal{D}/\overline{v^2}$, where molecular diffusion dominates, the width of the plume grows as $b \propto (\mathcal{D}t)^{1/2}$. In the turbulent convective regime, $\mathcal{D}/\overline{v^2} \ll t \ll T$, the plume width grows linearly with time, i.e. $b \propto \overline{v^2}^{1/2}t$. Finally, at sufficiently long times, $t \gg T$, the plume width obeys $\mathrm{d}b/\mathrm{d}t \propto \mathcal{D}_t$, where $\mathcal{D}_t$ is the turbulent diffusivity.

In a similar approach, Taylor's dispersion expression for plume width in the second and third regimes was developed in terms of the relative plume width to the integral length scale of the turbulence (Nedić and Tavoularis, 2016). The result is

$$b^2 \approx v^2(\Delta x/U)^2 \quad \text{for} \quad b \ll L \tag{2.13}$$

$$b^2 \approx 2vL(\Delta x/U) \quad \text{for} \quad b \gg L \tag{2.14}$$

where L is the integral length scale of transverse velocity fluctuations along the transverse direction, $L = Tv$, and $t = \Delta x/U$ is the diffusion time (Δx denotes the streamwise distance from the source). Using equation 2.12, Taylor's diffusivity can be estimated from the so-called apparent turbulent diffusivity, $\mathcal{D}_t = \frac{U}{2}\frac{\mathrm{d}b^2}{\mathrm{d}x}$. The above discussion on dominant diffusion mechanisms in the three regimes can be described in terms of the plume width as follows. In the first regime, where the root mean square separation of a pair of particles in the flow, $(\overline{X^2})^{1/2}$, is smaller than the Kolmogorov microscale, the plume width is very small and its spreading is dominated by molecular diffusion, termed as molecular-diffusive range. When the plume width grows, but still is much narrower than the integral length scale of the turbulence, the transverse velocity fluctuation governs the growth rate, known as the turbulent-convective range. In this range, diffusion is dominated by eddies of the size of $(\overline{X^2})^{1/2}$, and can be further divided into two subranges: Batchelor subrange, $t \ll t_B$ ($t_B = (\overline{X_0^2}/\epsilon)^{1/3}$ denotes the Batchelor timescale), where the diffusion depends slightly on the initial separation, X_0, and Richardson-Obukhov subrange, $t_B \ll t \ll T$, where the diffusion depends only on the mean dissipation rate of the turbulent kinetic energy. Finally, as the plume width grows sufficiently larger than the integral length scale of the turbulence, its growth rate is determined by the variance of the transverse velocity fluctuations and the integral length scale, referred to as turbulent-diffusive range (Salazar and Collins, 2009; Vanderwel and Tavoularis, 2014a; Nedić and Tavoularis, 2016).

For a continuous plume from a point source in a uniform mean turbulent flow, assuming that the streamwise diffusion is negligible and the radial turbulent diffusivities are uniform and equal (i.e. constant transverse diffusivity), a Gaussian curve predicts the mean concentration of the plume (Arya, 1999),

$$\overline{\phi} = \frac{Q}{4\pi \mathcal{D}_t x} \exp\left[-U\left(\frac{y^2 + z^2}{4\mathcal{D}_t x} \right) \right], \tag{2.15}$$

where Q is the volume flux. Accordingly, the maximum concentration and the width of the plume are found to follow x^{-1} and $x^{1/2}$ power-law decay and growth rates, respectively (e.g. Fischer et al. 1979). In the actual turbulent flows, however, the turbulent kinetic energy and the integral length scale of the plume evolve downstream and so does the turbulent diffusivity (Crimaldi and Koseff, 2006; Vanderwel, 2014), which in turn affects the accuracy of the Gaussian model.

Experimental studies of plumes in turbulent flows confirmed the Gaussian distribution of the mean scalar profiles, $\overline{\phi}/\overline{\phi_c} = \exp(-y^2/2\sigma_\phi^2)$, where σ_ϕ is the standard deviation of the time-averaged scalar profile (Fackrell and Robins, 1982; Webster et al., 2003; Crimaldi and Koseff, 2006; Connor et al., 2018). The plume width in grid turbulence (Warhaft, 1984; Anand and Pope, 1985) and in shear flows (Webster et al., 2003; Rahman and Webster, 2005; Lepore and Mydlarski, 2011; Vanderwel and Tavoularis, 2014a) followed power-law growth, although not necessarily at the same rate as the theoretical predictions.

Isokinetic free and near-bed plumes in grid turbulence showed Gaussian mean scalar profiles, regardless of the release position; i.e. truncated Gaussian for vertical mean profiles in the near-bed plumes (Connor et al., 2018). The mean distribution of the near-bed plume closely resembled the instantaneous scalar distributions, indicating that the plume evolution occurred within the viscous sub-layer of the boundary layer of the channel flow, where flow is relatively laminar. A similar effect was observed for a near wall plume in channel flow by Crimaldi and Koseff (2006). For the free plumes, however, the mean distribution was dissimilar to the instantaneous distributions due to the highly intermittent nature of free plumes. Also, it was argued that with an increase in the flow speed for the free plume case (i.e. higher Peclet number), diffusive scalar mixing decreases during the advective timescale (i.e. $\mathcal{D}/\overline{v^2} \ll t \ll T$) (Connor et al., 2018).

The (transverse) width of a neutrally buoyant isokinetic plume in a fully-developed turbulent boundary layer (released near the smooth bed of a [shallow] open channel flow) followed a growth rate of $x^{0.75}$ (Webster et al., 2003). While the mean centerline concentration decayed as x^{-1} for $x/H > 2$ (H being the channel depth), the scalar variance decayed more rapidly at $x^{-3.5}$, indicating that the plume became more homogeneous more rapidly than it was diluted by the ambient fluid. Closer to the source ($x/H < 2$), the scalar variance followed an exponential decay (or a x^{-2} power-law) and the mean concentration decayed faster than the theoretical predication of x^{-1}. This was attributed to the downstream evolution of eddy diffusivity until the eddy sizes reach the integral length scale of the turbulence (i.e. half the channel depth, $H/2$ (Webster et al., 2003). The mean centerline concentration at $x/H > 2$ remained almost unchanged with variation of Reynolds number (Re = 5000 - 20000), while it varied greatly with the source nozzle diameter ($d = 2.2 - 9.4$ mm) (Mohaghar et al., 2020). The integral length scale and Taylor microscale of the scalar reached asymptotic values beyond $x/H > 10$, indicating the self-similarity of the scalar field.

Nedić and Tavoularis (2016) studied the diffusion of a thermal line source in a wind tunnel with a fractal grid and three regular grids with equal solidity and mesh sizes comparable to the iterations of the fractal grid. It was shown that the mean scalar profile was Gaussian regardless of the grid type, not only in the fully developed region of the decaying grid turbulence, but also in the developing region, where the mean velocity was non-uniform and the turbulence was transversely inhomogeneous. Similar observations of the Gaussian profile of the mean scalar in non-uniform velocity fields was made by Karnik and Tavoularis (1989) for a line plume in uniformly sheared flow and by Lavertu and Mydlarski (2005) in a channel flow. The fractal grid enhanced the scalar diffusion compared to the regular grid with mesh sizes much smaller than the largest element of the fractal grid, L_0, because of an increased turbulence production due to the higher-level elements in the fractal grid (Suzuki et al., 2010a,b; Laizet and Vassilicos, 2015; Nedić and Tavoularis, 2016). However, the regular grid with a mesh size of L_0 (i.e. roughly equal to half the height of the duct) produced the highest diffusion and scalar mixing, because of a stronger turbulence intensity and length scale than the fractal grid. The plume width was found to be maximum at an optimum grid position relative to the source (almost one duct height upstream of the source), beyond which the plume became narrower despite being exposed to larger turbulence intensity.

Diffusion of a line source plume in a high-aspect-ratio, fully turbulent channel flow (Lavertu and Mydlarski, 2005; Lepore and Mydlarski, 2011) is an example of scalar diffusion in inhomogeneous turbulence. While the former studied a vertical line source, which roughly represented a statistically two-dimensional plume, the latter, oriented the line source horizontally (i.e. in the direction of the velocity inhomogeneity), resulting in a three-dimensional thermal plume. The lateral mean concentration profiles were Gaussian in both studies, while the rms profiles showed differences based on the line source configuration. Similar to diffusion in homogeneous flows, the rms profiles of the 3D plumes were symmetric, and evolved from single-peaked shape in intermediate downstream distances to double-peaked profiles far downstream. Moreover, the centerline mean and rms concentrations, as well as the corresponding half-widths were found to follow power-law evolution. In contrast, the statistically two-dimensional plume showed no tendency to follow a power-law growth rate of the scalar half-width, and the rms profiles remained single-peaked for the full downstream distance studied.

Vanderwel and Tavoularis (2014a) studied the diffusion of a slender point source plume in uniformly sheared flow (vertically homogeneous), following the plume meandering axis. In the uniformly sheared flow, the TKE grows exponentially from an effective origin upstream of the source. Despite flow anisotropy, the mean concentration profiles showed Gaussian distribution for $x/L > 5$, beyond which the injection effects became less persistent (L denotes the length of the flow separator used to allow flow development). Both the transverse and spanwise half-widths grew with power-laws, $x^{0.75}$, while the spanwise half-width was larger than transverse half-width by a factor of 1.25, due to greater velocity fluctuations in the spanwise direction than in the transverse direction. Centeroidal mean and rms concentrations, normalized by ϕ_0, decayed with streamwise distance at $x^{-1.4}$ and x^{-1} power-laws, respectively. While the decreased mean concentration indicates plume mixing with the ambient flow, the decreased rms concentration implies more homogeneity within the plume (Webster et al., 2003). Thus, contrary to the plume in a turbulent boundary layer (Webster et al., 2003), in the uniformly sheared flow, the plume is diluted faster than it becomes homogeneous. The turbulent diffusivity was several orders of magnitude greater than the molecular diffusivity, with a large contribution of the in-plane turbulent diffusive fluxes (spanwise and transverse), while the streamwise diffusive flux was an order of magnitude smaller than the in-plane flux and contributed less than 5% to the net diffusion.

Although the mean scalar profile has a robust Gaussian shape even in the regions with nonuniform velocity (e.g. Karnik and Tavoularis 1989), and turbulence inhomogeneity (Nedić and Tavoularis, 2016) and anisotropy (e.g. Vanderwel and Tavoularis 2014a), the rms profiles show more sensitivity to the state of development of the plume. The rms profiles of the point source plume (transverse rms in the near-bed plumes) show bimodal distribution (Fackrell and Robins, 1982; Bara et al., 1992; Rahman and Webster, 2005; Connor et al., 2018), with the off-center maxima being greater when the length scale of the well-mixed central core is comparable or larger than the local scale of the plume meandering (Bara et al., 1992; Connor et al., 2018). Near the release point, the plume meandering is smaller than the plume width, and the rms profile has larger peaks. Further downstream, the plume meanders at larger scales as compared to the local length scale of the plume (e.g. plume width) and the rms profiles become smoother. With this trend, the rms profiles are expected to evolve into single-peaked profiles further downstream (Connor et al., 2018), and again revert to a double-peaked shape far downstream, when turbulent diffusion begins to prevail. A similar trend is seen for a line source in decaying grid turbulence (Warhaft, 1984; Stapountzis et al., 1986; Nedić and Tavoularis, 2016), and a high-aspect-ratio, fully turbulent channel flow (Lepore and Mydlarski, 2011). This behavior agrees with the meandering plume model (Bara et al., 1992), which suggests that the rms peaks will occur in the regions where plume spreading is mainly due to small-scale turbulent mixing rather than to large meandering motions.

The emergence of dual peaks near the inflection points of the mean scalar profiles is associated with an increased gradient transport (Sreenivasan et al., 1982), particularly when the plume width becomes large compared to the local turbulent length scale. At sufficiently far downstream distances, this could be an indication of the existence of a turbulent-diffusive range (Nedić and Tavoularis, 2016). Observations of a point source plume in uniformly sheared flow, however, did not exhibit dual peaks for $12 < x/L < 35$, which was attributed to the very small width of the plume compared to the turbulent length scale, such that local scalar transport was carried out by eddy motions that sweep much of or the entire plume width and thus smooth off-axis peaks of concentration fluctuations (Vanderwel and Tavoularis, 2014a).

It is noted that the contribution of the scalar fluctuations in the calculation of the rms is nonlinear, and hence the rms profiles extend laterally and longitudinally further than the mean profiles. This is attributed to the highly intermittent nature of the plume, where rare but relatively strong scalar events exist and cause the mean concentration to decay spatially more quickly than the rms concentrations (Connor et al., 2018). Similarly, Vanderwel and Tavoularis (2014a) reported a greater rms half-width than a mean half-width for a plume source in uniformly sheared flow. Strong meandering of the plume causes fluid parcels from the edges of and outside the plume to cross its axis more often. Simultaneous large fluctuations in the axial velocity and the concentration result in a large turbulent scalar flux, $-\overline{\phi' u}$, which is an implication of turbulent diffusion. Vanderwel and Tavoularis (2014a) proposed that a positive turbulent scalar flux near the plume axis is the result of the plume width growth with downstream distance, associated with transverse turbulent diffusion.

2.5 Laser-induced fluorescence technique for measuring scalar concentrations

Laser-induced fluorescence (LIF) is a popular, non-intrusive technique to measure scalar concentrations. Fluorescent dyes that absorb energy and emit photons at different wavelength spectra are mixed into the flow, which is illuminated by a laser light sheet and whose emitted fluorescent light is captured by an optical device (usually a camera). Continuous wave or pulsed lasers can be used to excite the fluorescent molecules from the ground state to a higher energy level. Once exited, the molecule collides with other molecules, loses some energy and returns to the ground state while emitting a photon. Due to the loss of energy, the emitted light has a longer wavelength, corresponding to a lower energy level. The separation between the (peaks of the) absorption and the emission wavelength spectra (i.e. the Stokes shift) allows for easy differentiation between the illumination and the emitted light. The emitted light is correlated to the local dye concentration, and, because the absorption of the energy and the emission of the fluorescent light occur within a few nanoseconds, it allows for instantaneous measurement of the concentration field.

The ability to perform high spatiotemporal concentration measurements makes LIF a powerful tool for turbulent flow studies. The LIF technique became more popular following the work of Dewey Jr (1976) on the potential applications of the technique, and the work of Owen (1976); Liu et al. (1977) on qualitative concentration measurements. Breidenthal 1981; Dyer and Crosley 1982; Koochesfahani and Dimotakis 1985; Walker 1987, and Ferrier et al. 1993 are among those who contributed to the development of the LIF technique.

The relationship between the dye concentration and the emitted fluorescence intensity is, in general, nonlinear, and three main parameters control the fluorescence intensity: the quantum efficiency (Ψ), the intensity of the incident radiation (I_{f_0}), and the molar absorptivity of the species (β) (Guilbault, 1973),

$$I_f = \Psi I_{f_0}\{1 - \exp(-\beta b \phi)\}, \tag{2.16}$$

where I_f is the fluorescence intensity, b is the path length of the cell, and ϕ is the molar concentration. For very dilute concentrations, i.e. $\beta b \phi < 0.05$, the exponential term can be expressed as the first two terms of a Taylor series expansion, and hence the fluorescence intensity varies linearly with the species concentration (given a constant laser power):

$$I_f = \Psi I_{f_0} \beta b \phi. \tag{2.17}$$

The use of LIF generally lies in the linear range, which simplifies the calibration process and the data analysis. However, some studies have used the non-linear range of the intensity-concentration relationship (e.g. Wang and Fiedler 2000b; Crimaldi and Koseff

2006; Crimaldi 2008). The nonlinear range begins where the local excitation intensity exceeds the saturation intensity for the dye (Crimaldi, 2008). In the non-linear range, the fluorescence intensity usually increases with concentration, although at a lower rate than in the linear range, and in some conditions, it decays with a further increase in the concentration.

LIF can be used in different contexts for measurement of concentration. The fluorescence intensity can be captured by a photodetector, such as a photomultiplier tube, photodiode, or camera. The LIF measurements can be (i) punctual (focusing a laser beam on a small spot), (ii) along a line coinciding with a section of laser beam, (iii) planar by creating a laser sheet using a cylindrical lens or scanning the laser beam by a rotating mirror, or (iv) volumetric by rapidly sweeping a laser sheet. The most common application of LIF in fluid flows is planar laser-induced fluorescence (PLIF).

Potential sources of error of the LIF technique include attenuation, saturation, photobleaching and thermal blooming. The primary considerations for the selection of a dye for a PLIF experiment include the compatibility of the absorption spectrum with the laser excitation, a large separation between the absorption and the emission spectra, a high quantum efficiency to maximize the light intensity (Arcoumanis et al., 1990), a small degree of sensitivity to temperature and PH (Smart and Laidlaw, 1977; Walker, 1987; Coppeta and Rogers, 1998), resistance to photobleaching (Crimaldi, 1997; Wang and Fiedler, 2000a; Larsen and Crimaldi, 2006), and linearity of the fluorescence with concentration (Karasso and Mungal, 1997; Shan et al., 2004).

A source of non-linearity of the fluorescent response is attenuation of the laser light. Attenuation occurs when the laser beam crosses through non-negligible volumes of dyed fluid before it reaches the measurement location, and thus (a part of) the laser energy is absorbed by the fluorescent dye. Fluorescence saturation is another condition at which the intensity-concentration relationship is non-linear due to higher rate of excitation compared to the rate of fluorophore deactivation of the dye (Patsayeva et al., 1999).

Photobleaching occurs when the fluorescence intensity decays in time due to constant irradiation. Photobleaching depends on the type of fluorescent dye, flow velocity (Crimaldi, 1997; Wang and Fiedler, 2000a), dye concentration and laser power (Wang and Fiedler, 2000a). Photobleaching increases with laser power and dye concentration, and decreases with flow velocity. Rhodamine 6G and Fluorescein are the two most common PLIF dyes used in aqueous solutions. While Rhodamine 6G is highly resistant to Photobleaching (Crimaldi, 1997; Larsen and Crimaldi, 2006), Fluorescein is susceptible to this error (Crimaldi, 1997), although it is shown to be minimal for the concentration range of typical PLIF applications (Larsen and Crimaldi, 2006).

Temperature fluctuations should be avoided during the PLIF experiments, because the fluorescence decreases with a temperature increase (Guilbault, 1973; Walker, 1987). Moreover, temperature variations could cause buoyancy and inertial effects due to density differences in the fluid (Miller and Dimotakis, 1991; Lavertu, 2006). Another temperature-related error in LIF is thermal blooming, occurring when the beam diverges because of changes in the fluid density due to heating of the dyed medium by the laser beam. Thermal blooming depends on laser power and velocity, and results in a weaker fluorescent signal (Koochesfahani, 1984). Similar to photobleaching, the effects of thermal blooming can be reduced by decreasing the laser power (lowering the energy heating the dye) and increasing the flow velocity (reducing the time of continuous irradiation) (Wang and Fiedler, 2000a).

Secondary fluorescence is another source of error in PLIF measurements, recently investigated by Vanderwel and Tavoularis (2014b) for a slender plume and by Baj et al. (2016) for an isokinetic scalar tracer in the near wake of a multi-scale turbulence generator. This error arises because not only the fluorescence light emitted by the dye within the laser sheet is received by the camera, but the entire volume of the dyed fluid contributes to the PLIF image. Secondary fluorescence is attributed to absorption and re-emission of primary fluorescence both within and out of the laser sheet. Vanderwel and Tavoularis (2014b) showed that the out of sheet emissions are at least an order of magnitude smaller than the peak emission of the in-sheet dye, and out of focus, although almost clearly recognized/captured by the camera. As a result of the out-of-sheet fluorescence, the detection of the flow outline is inaccurate and the estimation of the local mass flux of the scalar is positively biased. To compensate for this error, a pre-multiplied histogram of the logarithmic concentrations of the normal-plane measurements (normalized by the source concentration) was used to determine a threshold for each set of images. The bandwidth of the in-sheet dye concentration was distinct from the background noise (even at the farther downstream distances where the peaks of the histogram shifted towards lower concentration values whereas the background noise remained essentially unchanged), while it overlapped with the out-of-sheet dye concentrations in lower values. The threshold was selected such that the area under the in-sheet curve below the threshold was equal to the area under the out-of-sheet curve above the threshold, hence conserving the mass of the in-sheet dye in the thresholding procedure. This way, a bias of 5-8% was removed out of a 20-30% bias (if uncorrected) in the mean concentration measurements. Similarly, Baj et al. (2016) showed that the secondary fluorescence error could exceed 50%, depending on several factors such as size of the experimental facility and the spatial topology of the scalar field. Their result suggested that the secondary fluorescence is responsible for a smooth transition in the scalar field from its peak values to the uniform background level, an effect that should be distinguished from molecular diffusion, which is far too weak to develop such large structures (Sc = 2500).

Chapter 3

Experimental methods

The effect of ambient turbulence on a turbulent axisymmetric jet and on an momentumless scalar patch was investigated. A random jet array was used to produce an approximately isotropic homogeneous turbulence with no mean flow in the ambient. Planar laser induced fluorescence (PLIF) was used to visualize the flow and measure the the passive scalar fields of the turbulent jet and the momentumless scalar patch. The evolution of the passive scalar field of the jet and the momentumless scalar patch was analyzed to study the structure, entrainment and mixing of the jet, and the diffusion of the momentumless scalar patch due to the RJA-generated turbulence. The following paragraphs provide a detailed description of the experimental facility (Sec. 3.1), PLIF apparatus for the turbulent jet experiments (Sec. 3.2), the modifications for the turbulent diffusion tests (Sec. 3.3), and the data acquisition and post processing procedures (Sec. 3.4).

3.1 Experimental facility

The experiments were carried out in the Environmental Hydraulics lab at the Department of Civil Engineering at McGill University. The lab is equipped with (i) a large water tank, a random jet array (RJA), an axisymmetric jet, and its hydraulic system, and (ii) planar laser-induced fluorescence apparatus, including a continuous wave laser, a laser scanning

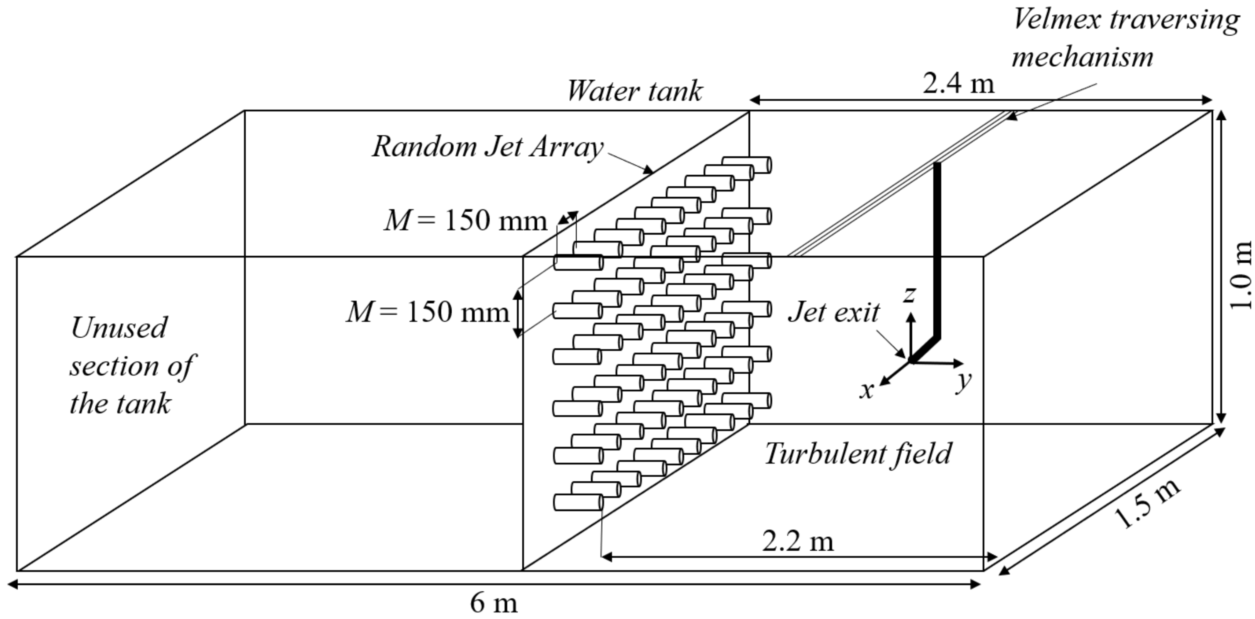

Figure 3.1: Schematic of the experimental facility (water tank, RJA, and the jet apparatus) (not to scale).

device, a digital camera and optics that form the data acquisition setup to observe and record the flow. Figure 3.1 shows a schematic view of the water tank, the RJA, and the jet apparatus.

3.1.1 Water tank

The PLIF experiments were conducted in a large water tank, with its top open to the ambient air. The tank is $1.5 \times 6 \times 1 \text{ m}^3$ in dimension, and a $1.5 \times 2.4 \times 1 \text{ m}^3$ section was used for the experiments (filled to a depth of 0.9 m). The side walls of the tank are single panes of 19.05 mm thick tempered glass. Two 19.05 mm panes, giving a total thickness of 38.1 mm, are used for the bottom to support the hydro-static pressure of the water. The assembly of glass panes is supported by a steel frame at a height of 0.7 m to give visual access from the bottom of the tank. The experimental facility is located in a dark room with its walls, floor and ceiling painted in matte black to reduce the reflections of the excited fluorescent dye and the scattered light from the laser to ensure the background light level is negligible.

3.1.2 Ambient water conditions

The experiments were carried out in one of two background conditions corresponding to the jet in (i) a quiescent ambient, and in (ii) an approximately homogeneous isotropic turbulent ambient. For both ambient conditions, the tank was cleaned and filled with fresh water, mixed from the hot and cold water supply, at the ambient temperature to prevent differential expansion of joints and possible leakage, or stratification in the tank. For the quiescent ambient, sufficient time (about 6 hours) was given for the water to come to a rest and to a thermal equilibrium with the ambient air temperature. During the settling time, tiny bubbles of oxygen were either dissolved into the water due to a rise in temperature or settled on the sides of the tank. The bubbles on the sides of the tank were carefully wiped off, as by scattering the laser light, they could be a source of error in the LIF experiments.

The turbulent ambient was created using a random jet array (RJA) to generate an approximately homogeneous, isotropic turbulent (HIT) field with negligible mean flow inside the tank. The RJA was an array of 6 rows and 10 columns of water jets (Fig. 3.2), based on that initially used by Variano and Cowen (2004) in a smaller size. The jets were created with sixty bilge pumps (Rule 25D, 500GPH) mounted on a $1.5 \times 1\ \mathrm{m}^2$ polyethylene sheet and having a uniform horizontal and vertical spacing with a center-to-center distance (M) of 15 mm, and symmetry with respect to the tank sides to reduce secondary circulation (Fernando and De Silva, 1993; Variano and Cowen, 2004; Variano et al., 2008). The pumps' outflow was perpendicular to the RJA plate with the outflow of the jet positioned at a distance of 0.24 m from the RJA sheet using a a PVC elbow (Spears 1404-010) and a 0.15 m long PVC extension connected to the pump outflow. The suction and the discharge of each pump occurred simultaneously into the same fluid volume, creating a negligible net mass flow rate. Downstream of the jet array, the jets merged creating a

Figure 3.2: Random jet array (RJA).

quasi-homogeneous isotropic turbulence, in planes parallel to the RJA, with negligible mean flow, whose turbulence intensity decreases with distance from the RJA.

The RJA was operated by independently and randomly turning the pumps on and off, under the control of a LabVIEW program. Previously in this lab, different driving algorithms were tested on the RJA to determine the closest approximation to a homogeneous isotropic turbulence with zero mean flow (Lavertu et al., 2008; Khorsandi et al., 2013; Perez-Alvarado et al., 2016). The RANDOM algorithm, similar to that proposed by Variano et al. (2008), generated the highest turbulence intensity and and closest approximation to isotropic homogeneity downstream of the RJA. In this algorithm, each pump was operated individually with its on and off time selected randomly from a normal distribution with (μ_{on}, σ_{on}) = (12 , 4) s, and $(\mu_{off}, \sigma_{off})$ = (108 , 36) s, resulting in approximately 10 $\%$ of the pumps operating at any arbitrary time.

3.1.3 Round turbulent jet

A round turbulent jet, supplied by a constant head reservoir, issued horizontally and parallel to the RJA sheet. The jet apparatus consisted of a supply reservoir, a pump, a constant-head reservoir, a rotameter, valves, connecting pipes, and a traversing mecha-

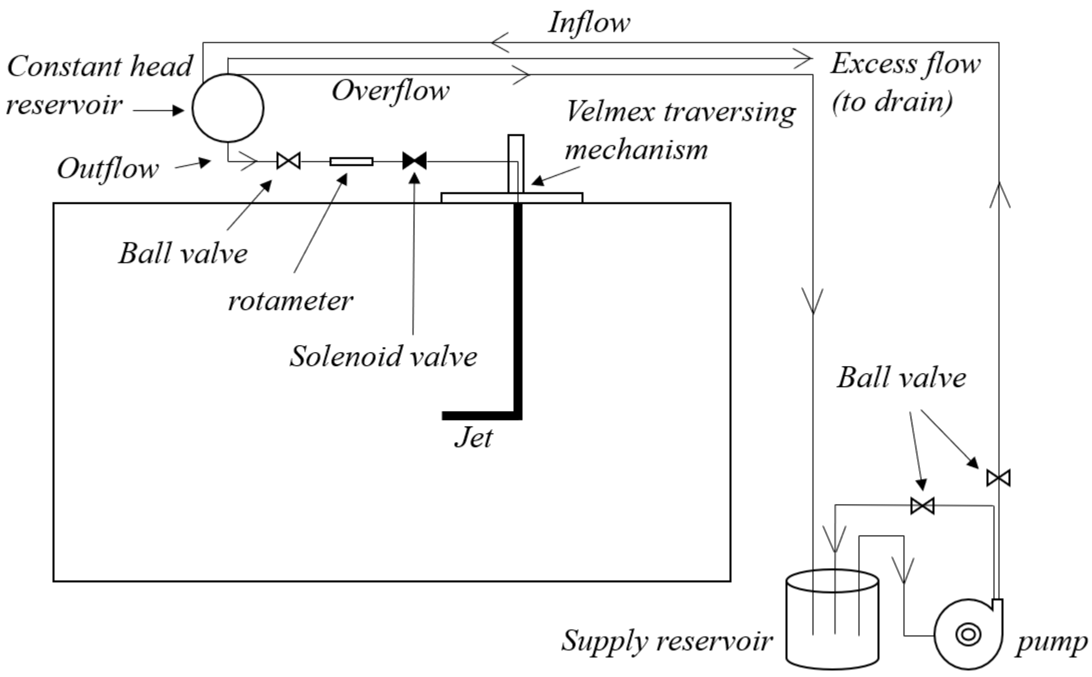

Figure 3.3: Schematic of the hydraulic system and the jet apparatus.

nism. A schematic view of the jet apparatus and its hydraulic system is illustrated in Fig. 3.3.

The jet exited from a copper tube of 8.51 mm inner diameter, extending vertically for 1.2 m, and after a 90° bend extending horizontally for 0.2 m ($\sim 24d$) to the exit, generating a fully developed flow at the jet exit. The jet discharged horizontally parallel to and at a transverse distance of 1.10 m from the RJA plane (i.e. y/M = 7.3), where the turbulent kinetic energy (TKE) of the ambient was k_{HIT} = 4.4 $\mathrm{cm}^2\mathrm{s}^{-2}$ (Khorsandi et al., 2013). The turbulence level experienced by the jet was constant along the jet axis (Khorsandi et al., 2013), although the background turbulence decayed in the direction perpendicular to the RJA plane (i.e. in y direction). The jet discharged at mid-depth (i.e. 0.45 m) and 0.5 m from the tank side wall to minimize the free surface and the boundary effects.

The jet was mounted on a Velmex traversing mechanism, allowing its position to be precisely adjusted in the streamwise (x) and the vertical (z) directions. The Velmex traversing mechanism was an array of three BiSlide assemblies allowing precise transla-

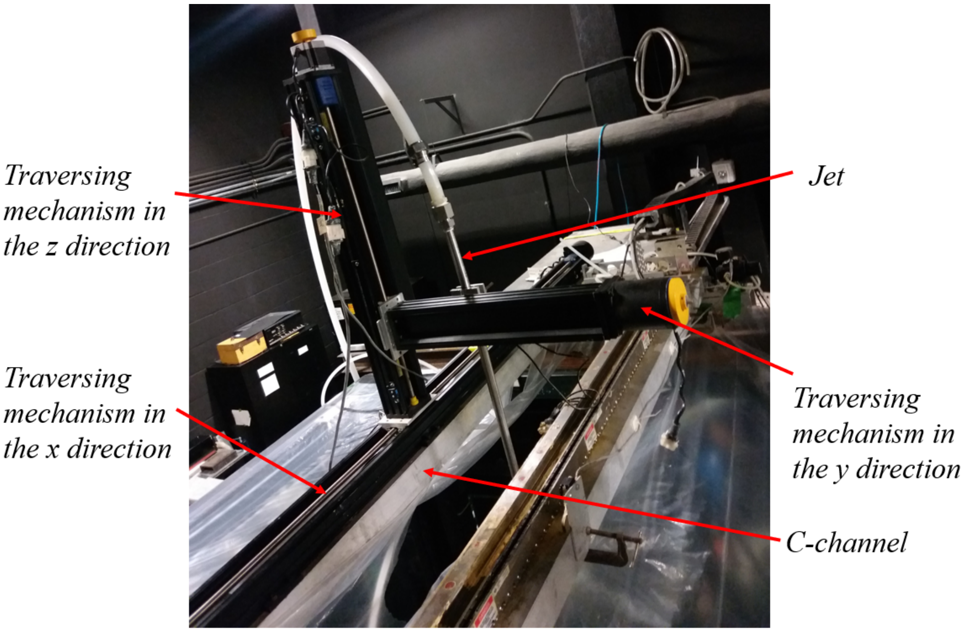

Figure 3.4: Velmex traversing mechanism.

tion in the x, y, and z directions (Fig. 3.4). Each BiSlide assembly consisted of a base, a carriage, and a lead screw driven by an electric motor. Limit switches were used to avoid a collision between the jet and the tank sides, and between the carriage and the end plates of the base. The maximum possible displacement of the mechanism was 1.30 m, 0.24 m and 0.55 m in x, y, and z directions, respectively. The traversing mechanism has a resolution of 0.05 mm in all directions, and was driven by a Velmex VXM-2 motor, which was controlled by a LabVIEW program. The traversing mechanism was mounted on a C-channel, spanning the width of the tank in the x direction, which was itself mounted on two paralell C-channels with wheels that could be manually moved along the tank (i.e. in the y direction). The lateral distance between the jet and the RJA was manually set and fixed at $y/\mathrm{M} = 7.3$, and only x and z BiSlides were used for positioning the jet.

The jet was first aligned in the vertical and the horizontal directions using a plumb bob and a magnetic level, respectively (Fig. 3.5). Then, the jet was moved as close as possible to the tank side and a large set square was used to precisely align the jet normal to the tank wall and hence parallel to the RJA plane. The alignment procedure was repeated at

Figure 3.5: Horizontal alignment of the jet.

several x and z positions, and fine adjustments to the jet orientation was applied through its connecting nuts.

The jet fluid was prepared as a homogeneous mixture of water and the fluorescent dye in the supply reservoir, a 55 liter spherical glass container. The constant-head reservoir, a 12 L spherical glass container, located approximately 3 m above the jet and continuously supplied from the supply reservoir by a 1/3 hp pump, fed the jet at a constant flow rate, and, thus, a constant jet Reynolds number. The flow rate was set through a 5 GPM rotameter (King Instrument Company), which had an error of 5 $\%$, and the flow rates of 2.3 l/min and 4.2 l/min corresponded to Reynolds numbers of $Re =$ 5800 (± 290) and 10600 (± 530), respectively. A solenoid valve, placed immediately after the rotameter, was used to turn the jet flow on and off during the experiments.

3.2 Planar laser-induced fluorescence apparatus for the turbulent jet experiments

The planar laser-induced fluorescence (PLIF) method was employed to obtain the concentration field of a passive scalar in a turbulent jet released into a quiescent ambient and a turbulent ambient. The PLIF apparatus consisted of laser sheet generation setup and signal detection system, which were aligned perpendicular to the jet axis such that the laser

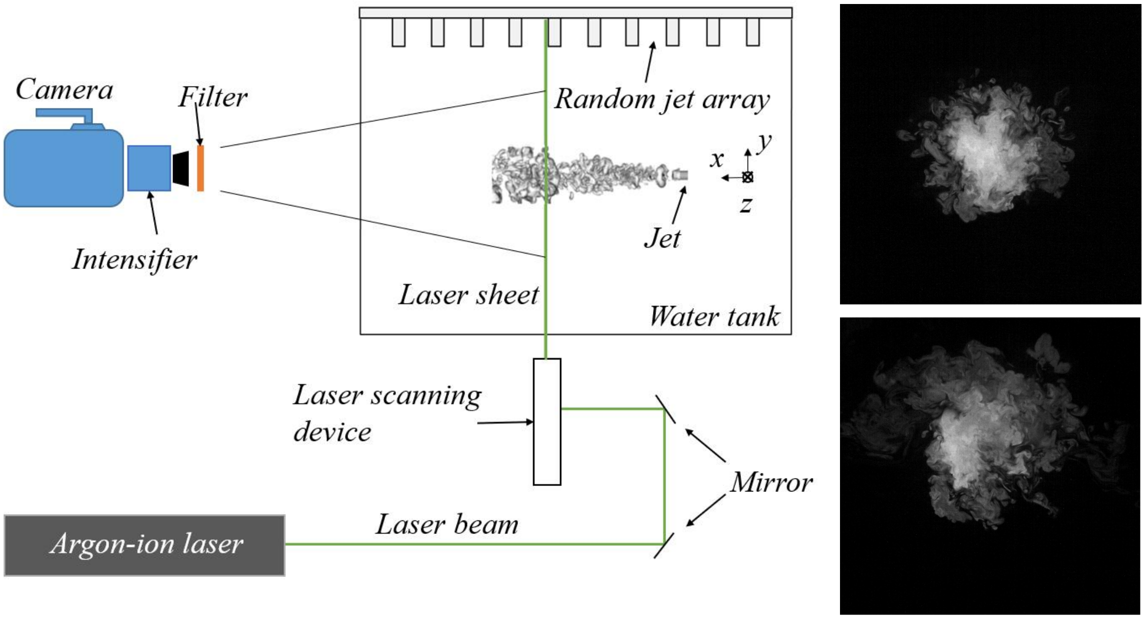

(a) (b)

Figure 3.6: (a) Schematic of the PLIF apparatus in the turbulent jet (top view), (b) examples of instantaneous jet cross-section in the quiescent (top), and the turbulent (bottom) ambient.

sheet illuminated an orthogonal cross-section of the jet. Figure 3.6 illustrates a schematic view of the PLIF apparatus, with examples of an instantaneous jet cross-section in the quiescent and in the turbulent ambient. Table 3.1 provides the experimental parameters of the PLIF setup for the turbulent jet experiments and the turbulent diffusion experiments. Details of the turbulent diffusion apparatus are provided in Sec. 3.3.

Disodium fluorescein dye ($Sc = \nu/\mathcal{D} = 2000$) was used in the the turbulent jet experiments to visualize the jet flow. It has an absorption spectrum of 430 - 520 nm with its maximum at 490 nm, and an emission spectrum of 490 - 600 nm with a peak at 510 nm (Arcoumanis et al., 1990; Crimaldi, 2008). A small volume from an initially 1 $\mathrm{g\,L^{-1}}$ stock solution of disodium fluorescein was mixed into the 55 L supply reservoir to achieve a 0.02 - 0.04 $\mathrm{mg\,L^{-1}}$ dye mixture to feed the jet. Disodium fluorescein is highly sensitive to light, and thus it was only handled and used in darkness using a low intensity red light for illumination.

Table 3.1: Experimental parameters

Parameter	Symbol	Turbulent jet tests	Turbulent diffusion tests
Reynolds number	Re	5800, 10600	540
Schmidt number	Sc	2000	2500
Dye molecular mass	- [$\mathrm{g\,mol^{-1}}$]	376.3	479
Jet exit velocity	U_0 [$\mathrm{m\ s^{-1}}$]	0.682, 1.245	0.018
Lateral jet position to RJA	y/M (M = 150 mm)	7.3	7.3
Ambient TKE at $y/\mathrm{M} = 7.3$	k_{HIT} [$\mathrm{cm^2 s^{-2}}$]	4.4	4.4
RJA operating algorithm	(μ_{on}, σ_{on}), $(\mu_{off}, \sigma_{off})$	(12, 4) s, (108,36) s	(12, 4) s, (108,36) s
Axial distance	x/d	20, 30, 40, 50, 60	–
Field of view	FOV	640×640 mm^2	260×260 mm^2
PLIF spatial resolution	–	0.4 mm	0.13 mm
Sampling frequency	–	30 Hz	50 Hz

3.2.1 Laser sheet generation setup

A continuous mode Argon-ion laser (Coherent Innova 90) generated a laser sheet to excite the fluorescent dye. The laser was operated in single-line mode at a wavelength of 514.5 nm, and in light-regulated mode to maintain a stable output power (1 W in the present study) with a precision of ± 0.5 %, estimated by the manufacturer. The laser light was stabilized by warming it up for 60 minutes prior to the start of the experiment, and its power variation during the test (monitored by a Coherent Lasermate power meter) was below 2% for all the experiments. The laser aperture was set to its minimum (3.97 mm) and the emerging beam had a Gaussian cross-section (TEM$_{00}$). The beam was directed to the laser scanning device using two mirrors (Melles Griot 02MLQ003/009) that allowed for fine adjustment the orientation of the laser sheet.

A laser scanning device was used to focus the laser beam and generate the laser sheet. The laser scanning device consisted of a 12.7 mm dielectric mirror (Newport 5151), a focusing lens with a 1.5 m focal-length plano-convex lens (PLCX-25.4-772.6-C), and a high-speed rotating mirror (Lincoln Laser Company DT-08-236-019). All the components were

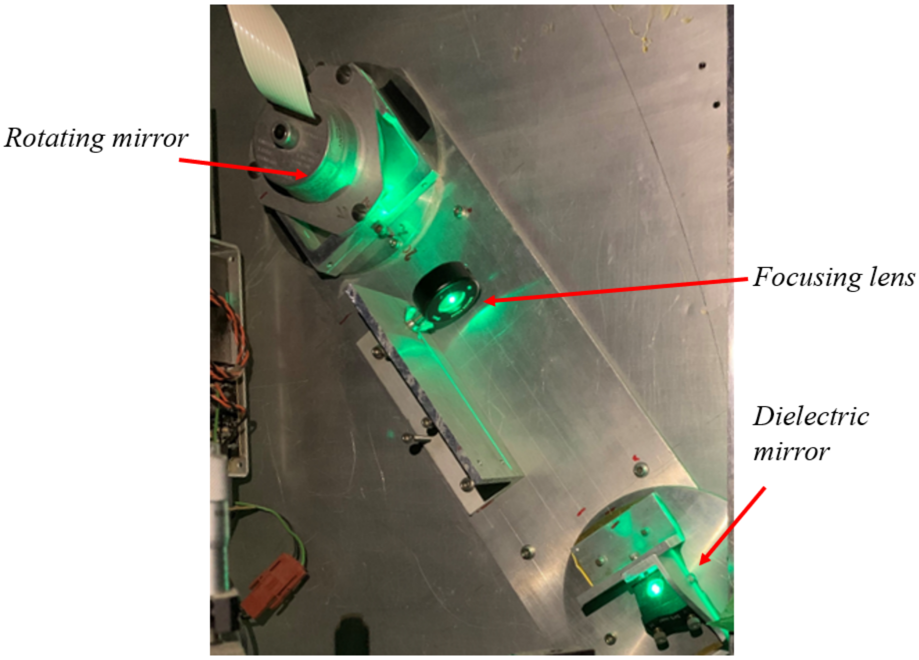

Figure 3.7: Components of the laser scanning device. The green laser beam is passing through the device.

aligned and mounted on an aluminium box (Fig. 3.7), and the laser beam passed through the dielectric mirror and the focusing lens to reach the rotating mirror. The rotating mirror was an 8-sided polygonal mirror that rotated at 12000 rpm and generated a laser sheet with 1600 beam scans per second and a 45° angle of expansion.

The laser sheet was aligned perpendicular to the jet axis. It was aligned in two steps; a rough vertical alignment using a plumb bob, and a fine horizontal and vertical alignment using the traversing mechanism. First, the plumb bob was suspended in the tank (full of water) and the laser sheet was aligned to illuminate the string of the plumb bob along its length. The jet was then placed at the measurement plane such that its tip just touched the laser sheet. The jet was then translated in the vertical (z) and the horizontal (y) directions to ensure that the tip of the jet was always just touching the laser sheet. The direction and the orientation of the laser sheet was adjusted using screws on the optical mirrors.

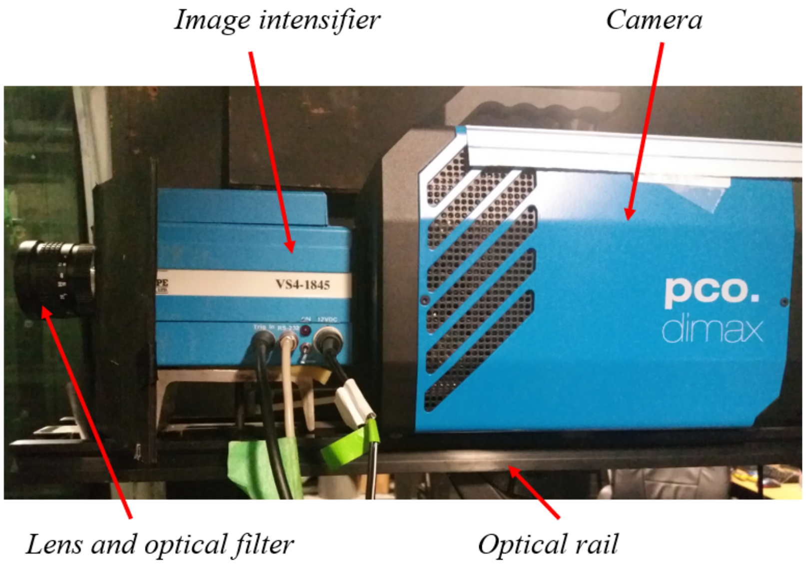

Figure 3.8: Signal detection system in the first setup.

3.2.2 Signal detection system

The signal detection system was a complementary metal oxide semiconductor (CMOS) camera equipped with an image intensifier, and an optical filter (Fig. 3.8). The system was positioned and aligned perpendicular to the laser sheet to record orthogonal cross-sections of the jet. To secure a precise alignment between the camera and the intensifier, both were fixed on a 0.69 m long optical rail, and two tripods (QuickSet 5-95534-9 and 5-95534-9A) allowed the adjustment of the position, height, and the orientation of the system.

The incident light first reached a 50 mm × 50 mm longpass color glass filter with a sharp cutoff at 550 nm (ThorLabs FGL550) attached to the camera lens to filter the scattered laser light and transmit only the light due to the fluorescence emission of the dye. Transmission of the filter at 525 nm was below 0.0004 % according to the manufacturer. The lens had a 50 mm focal length and a 43° angle of view, and its aperture was set to its maximum to allow the greatest amount of light onto the sensors.

An image intensifier (Video Scope VS4-1845) was used to increase the light sensitivity of the system. The intensifier was placed between the camera lens and the camera, and

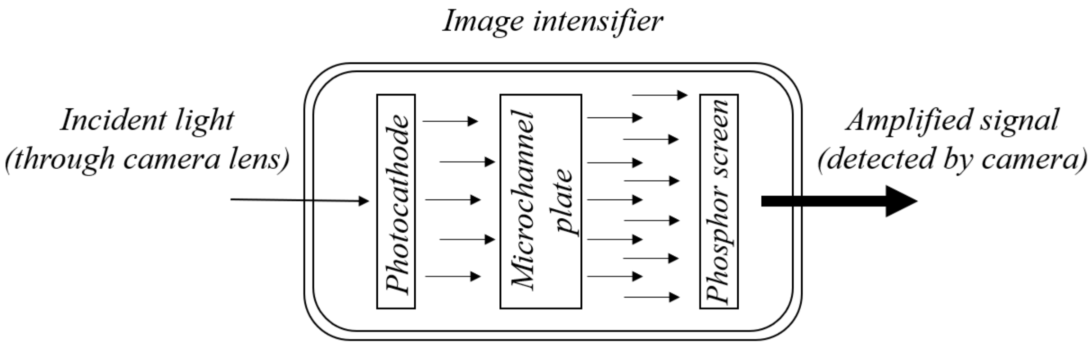

Figure 3.9: Signal intensification process.

was coupled to the camera with a C-mount adapter. The intensifier accelerated the flow of electrons using three plates at high DC voltage difference: a photocathode, a micro-channel plate and a phosphor screen. The incident light photons first reached a gallium arsenide (GaAs) photocathode and caused electron emission towards the micro-channel. The micro-channel prompted a secondary cascade of electrons towards the phosphor screen, which itself induced another flow of electrons. Thus, the number of photons was significantly increased due to successive excitation, and the final emission was an amplified light signal (Fig. 3.9).

The intensifier functioned in the range of 450 - 900 nm, which covered the rang of the filtered signal of the fluorescent light (i.e. 550 - 600 nm). The intensifier's gate, gain, and gate delay were set using the VSI image intensifier controller software provided by the manufacturer. The intensifier was operated in continuous (DC) gate mode, allowing an uninterrupted flow of electrons to the photocathode, and thus a continuous intensification process. The intensifier gain was set to 75000 and the gate delay was zero. The intensifier was only operated in darkness because its photocathode was very sensitive to light such that even normal light levels could severely damage its sensitivity.

A 12-bit, 4 MP (i.e. 2016 × 2016 pixels) monochrome CMOS camera, pco. dimax, recorded the fluorescent signal. The coupling of the intensifier and the camera reduced the size of the detection area to a central region of 1601 pixel diameter, covering a 640 mm diameter circular field of view with a spatial resolution of 0.4 mm × 0.4 mm per pixel.

The intensifier increased the light sensitivity of the central region of the image compared to the pixels at the margins. Thus, a pixel by pixel calibration was required to account for variation between the emitted signal by the fluorescent dye and that recorded on the camera pixels (details in sec. 3.2.3).

The camera system was aligned along the jet axis, such that the center of the jet coincided with the center of the image (a red cross in the controlling software of the camera, Camware) and the image was perpendicular to the jet axis. The alignment procedure was carried out in a full tank by moving the jet 0.30 - 0.40 m in the $\pm x$ direction to ensure that the jet axis remained always at the center of the image. Necessary adjustments in height and orientation of the optical system was achieved by adjustment screws and handles on the tripods. Finally, the focus of the camera was adjusted by placing the jet in the measurement plane with its tip just touching the laser sheet.

3.2.3 Calibration

The laser power was constant at 1 W during the PLIF experiments, however, the laser light intensity, defined as the ratio of the laser power to area, decayed due to the laser sheet expansion. In addition, the light sensitivity of the central region of the camera was higher compared to the edges due to the lens curvature and the image intensifier, such that 2^{12} discrete values could be detected at the central pixels, whereas only about 2^{11} values were discerned at the pixels at the margins. Thus, a pixel by pixel calibration was performed for each PLIF setup (i.e. for the turbulent jet experiments and for the turbulent diffusion experiments) to account for inhomogeneity of the pixel sensitivity to the incident light.

The relation between the fluorescence intensity and the dye concentration is, in general, non-linear (Guilbault, 1973):

$$I_f = \Psi I_{f_0}\{1 - \exp(-\beta b \phi)\}, \tag{3.1}$$

where I_f is the fluorescence intensity, Ψ is the quantum efficiency, I_{f_0} is the incident radiant intensity, β is the molar absorptivity, b is the path length of the cell, and ϕ is the dye concentration. When the concentration is very low and the absorptivity is less than about 0.05, the exponential term becomes very small ($\beta b \phi << 1$), and it can be replaced with the first two terms of its Taylor expansion, such that

$$I_f = \Psi I_{f_0} \beta b \phi. \tag{3.2}$$

Therefore, for a constant laser power and small levels of the dye concentration, a linear function demonstrates the relationship between the dye concentration and the fluorescence intensity. The typical use of PLIF remains in the linear range of the concentration-intensity relationship, which makes the calibration process and data analysis simpler. To further simplify the concentration-intensity relation in the linear range, a linear curve fit can be applied as below:

$$\phi_{i,j} = A_{i,j} I_{i,j} + B_{i,j}, \tag{3.3}$$

where ϕ and I are corresponding dye concentration and laser intensity at any arbitrary pixel (i, j), respectively, and A and B are the slope and the I-intercept of the linear regression for that pixel. Eq. 3.3 is used to convert the pixel light intensity to actual concentration value for the analysis. Figure 3.10 shows the linear relationship between the dye concentration and the intensity counts for a central pixel and one at the margins. It shows that the light sensitivity in the central region is higher than that in the pixels at the margins.

Calibration process

The calibration test was consisted of six successive PLIF tests using homogeneous mixtures of known and increasing dye concentrations (including zero concentration to determine the background intensity level) in a calibration box, placed at the measurement

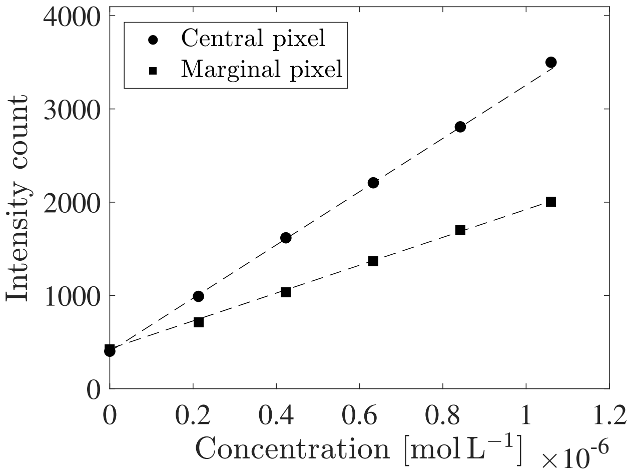

Figure 3.10: Examples of linear calibration fits to a central pixel and a marginal pixel.

location. The calibration box was a 0.31 × 0.43 × 0.75 m^3 container (Fig. 3.11), with 25.4 mm thick panes of plexiglass at its top and bottom, and 6.3 mm panes of tempered glass at the side walls. The top of the tank had a cutaway opening to allow access for filling and mixing the dye.

The calibration box was placed inside the large tank on top of two PVC supports to provide access to the drain holes, and to place it so that it extended over the full measurement region. The jet was placed inside the calibration tank to circulate the dyed fluid, and the connecting hoses were adjusted such that the calibration box served as the supply and the overflow reservoir of the jet. Figure 3.12 is a schematic of the hydraulic system of the calibration process. The small volume of the calibration box compared to the large tank had two benefits; first, it reduced the required fluorescent dye for calibration, and second, it minimized the possibility of laser attenuation and trapping (see 3.2.4), since the laser sheet passed through clear water before it reached the calibration tank.

The laser sheet entered the large tank through a slot to block any scattered laser light. The sides of the the calibration box and the large tank were covered with matte black plastic panels to ensure a dark background and a minimum light reflection. Both were filled with water to the same level, and a known dilute concentration of the fluorescent dye (e.g. 0.01 mg/L) was added to the calibration box for each test. The dye was thor-

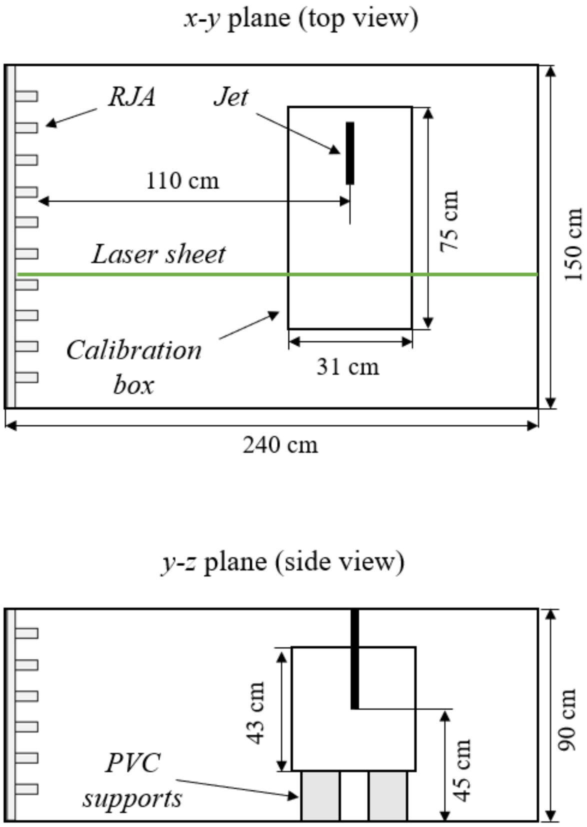

Figure 3.11: Calibration setup (not to scale).

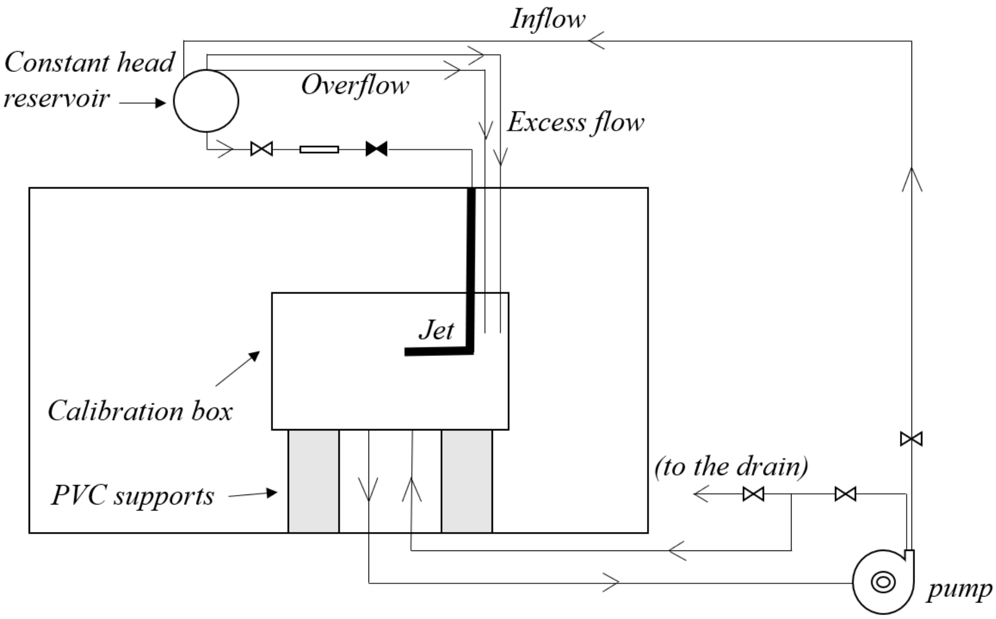

Figure 3.12: Schematic of the calibration hydraulic setup. x-z plane.

oughly mixed into the water by running the jet for a few minutes, and after a settling period of 20 minutes, the light intensities were recorded by the camera. The calibration test was repeated for progressively higher dye concentrations until the non-linear range of the concentration-intensity relationship was reached.

3.2.4 Potential errors in planar laser-induced fluorescence

The calibration test verified the linear relationship between the dye concentration and the light intensity for the calibrated range of the concentrations, which were used for selecting the jet exit concentration, ϕ_0, in the PLIF experiments. Also, the calibration process provided a context in which the potential sources of errors, including attenuation, trapping, thermal blooming, photobleaching and inertial effects can be assessed. This section describes the tests and the measurements taken to minimize the PLIF errors and their impact on the experimental results.

Attenuation of the laser beam is a situation at which the laser light passes through large volumes of dyed fluid, which absorb (a part of) the laser energy prior to reaching to the measurement location. This situation causes a non-linear relationship between the dye concentration and the light intensity. In the present experiments, the dye concentration was low, and the calibration process confirmed the linear relationship between the fluorescent signal and the actual concentrations, and hence attenuation of the laser beam was minimal.

Trapping of the fluorescent light occurs when the emitted fluorescence at the measurement location is absorbed by dye in another location, for example by the dye between the laser sheet and the camera, causing the camera to detect only a portion of the actual light intensity. Perez-Alvarado (2016) performed a test in the same experimental facility as in the present study (similar to a test by Lavertu (2006) in a punctual LIF setup) to determine the effect of trapping in the PLIF experiments. A small glass container was placed inside the large tank between the calibration box and the camera. First, a no trapping test was carried out with a known concentration of dye (within the calibrated range) in the calibration box and fresh water in the small glass container. Then, a known dilute concentration of the same dye was added to the small glass container, and the fluorescent signal was collected. Perez-Alvarado's results showed that the trapping effect was negligible in the present setup ($< 1\%$) in the calibrated range of the dye concentrations.

Thermal blooming occurs when the laser beam heats the dyed fluid and causes a temperature rise and a lower fluorescent signal due to heat absorption. Photobleaching explains the reduction in fluorescence emission of a dye due to continuous irradiation. In the present experiments, thermal blooming and photobleaching were minimized by rapidly spinning the rotating mirror to scan the laser beam at a rate of 1600 scans per second (i.e. a residence time of 625 μs for each beam scan), and thus long periods of beam irradiation were avoided.

Inertial effects and buoyancy are caused by density or temperature variation between the jet fluid and the ambient. The temperature variation was already eliminated by feeding the jet from the tank water. The possibility of heating of the jet fluid by the laser beam was also negligible. The density variation between the jet and the ambient was minimized by using dilute concentrations of the fluorescent dyes. The maximum concentration of disodium fluorescein and Rhodamine 6G at the jet exit was 1.1 $\times$ 10^{-7} $\mathrm{mol\,L^{-1}}$ and 3.15 $\times$ 10^{-8} $\mathrm{mol\,L^{-1}}$, respectively. The molecular masses of the two species are 376.3 g$\,\mathrm{mol}^{-1}$ and 479 g$\,\mathrm{mol}^{-1}$ for disodium fluorescein and Rhodamine 6G, respectively. Therefore, the density difference between the dyed fluid and the ambient water (ρ = 1000 kg$\,m^3$) was calculated to be less than 3 $\times$ 10^{-5} % and 4.3 $\times$ 10^{-5} %, respectively, and thus the inertial effects were negligible during the experiments.

3.3 Modifications to the apparatus for the turbulent diffusion tests

The second objective was to study the diffusion of a momentumless patch of a passive scalar due to the turbulence created by the RJA. It was of interest because the turbulent jet experiments showed that the eddies of the HIT ambient destroy the jet structure at some critical downstream distance, beyond which turbulent diffusion by the ambient eddies becomes the only mechanism to transport the passive scalar in the ambient fluid (see Ch. 4 of the present thesis and previous results by Khorsandi et al. (2013) and Perez-Alvarado (2016)). The evolution of the concentration field of the momentumless patch of the passive scalar is due to molecular diffusion in the quiescent ambient, and due to turbulent (and molecular) diffusion in the turbulent ambient.

The large field of view in the turbulent jet experiments, required to capture the full extent of the jet in the HIT ambient, was not required for the turbulent diffusion tests. Therefore, the camera was moved closer to the tank and the intensifier was detached, resulting in a smaller field of view (260 $\times$ 260 mm^2) and a higher spatial resolution (0.13 mm $\times$ 0.13 mm per pixel). The laser was replaced with a 1.5 W, 532 nm Diode laser (Dragon Lasers), generating a 2 mm-diameter Gaussian beam with a divergence of $<$ 1.5 mRad, according to the manufacturer. The laser was placed on the same table as the laser scanning device, and the alignment process was performed as described in Sec. 3.2.1. The camera was aligned perpendicular to the laser sheet, with its image center coinciding with the jet axis (ref. Sec. 3.2.2). The laser was operated at 1 W and a power meter was used to examine its power stability by measuring the laser power prior to and at the end of each test.

Rhodamine 6G dye (95$\%$ purity, Sigma-Aldrich Company Ltd.) was used as the passive scalar tracer for the turbulent diffusion tests to remain within the excitation range of the Diode laser. Rhodamine 6G has a molecular diffusivity of $\mathcal{D} = (4 \pm 0.3) \times 10^{-4}\,\mathrm{mm}^2\,\mathrm{s}^{-1}$ and a Schmidt number of $Sc = 2500 \pm 300$ (Gendron et al., 2008; Vanderwel and Tavoularis, 2014a). The absorption spectrum of the Rhodamine 6G lies between 460 - 560 nm with its maximum at 530 nm matching the emission wavelength of the laser (532 nm), and its emission spectrum is between 540 - 660 nm with its peak at 554 nm (Würth et al., 2012), so that the high pass optical filter ($>$ 550 nm) blocks the light from the laser sheet. This dye has a relatively high quantum efficiency within a wide range of concentrations

(Penzkofer and Leupacher, 1987), and is highly resistant to photobleaching and rarely sensitive to temperature and pH change (Crimaldi, 1997, 2008). Dye solutions were prepared by first mixing Rhodamine 6G powder with distilled water to make a 1 g L^{-1} stock solution. Then, very dilute solutions were prepared for the experiments by mixing 0.8 mg L^{-1} of dye into the water supply reservoir.

3.3.1 Generating a momentumless scalar patch

Generating a momentumless patch of the passive scalar was essential to isolate the effect of the HIT ambient eddies on the diffusion process. This was achieved by releasing the jet isokinetically; that is, to slowly tow the jet backwards while it was being discharged, at the same speed at which the dyed fluid exited the jet. In this way, the relative velocity between the released dyed fluid and the ambient was almost zero and a (relatively) momentumless, shear-free patch of a passive scalar was achieved.

Towing the jet (i.e. the one used in the jet in a turbulent ambient experiments with an 8.51 mm diameter) backwards in the ambient fluid, generated a wake that propagated towards the laser sheet and causing disturbances in the measurement location. These disturbances, induced by vortex shedding, could be reduced by lowering the towing speed of the jet. Lowering the towing speed (and equally the jet exit velocity), however, caused flow discontinuities during the jet discharge. These problems were resolved by using a larger jet (with 29.97 mm inner diameter) to maintain a sufficient flow rate at the lowest possible exit velocity (i.e. 18 mm/s, achieved by trial and error) that produced a continuous jet flow. Using a large-diameter jet and towing it at an optimally-selected low speed had some benefits: i) it deposited a sufficient amount of dye at a low exit Reynolds number, causing less disturbances at the measurement location, ii) increased the travel time of the jet across the tank width, which allowed a better control of the experiments, and iii) improved the relative spatial resolution of the experiments by increasing the integral length scale of the passive scalar field.

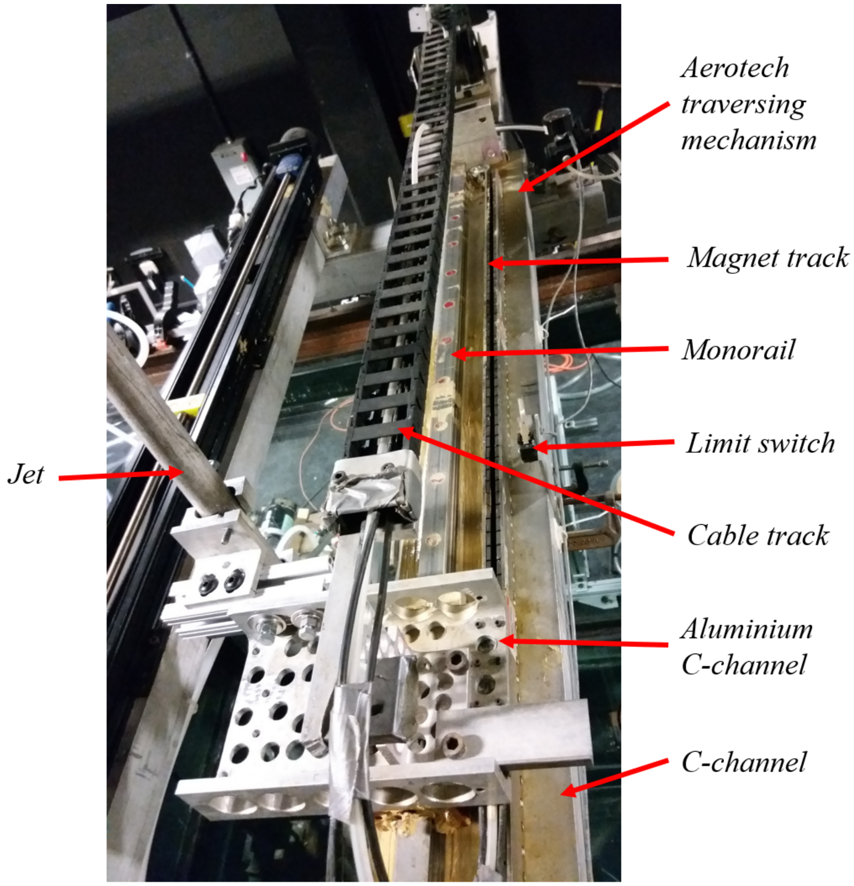

Figure 3.13: Aerotech traversing mechanism.

The new jet, a 29.97 mm inner diameter steel tube, was mounted on an Aerotech high-precision linear traversing mechanism (Fig. 3.13), which allowed precise movement of the jet with a wide range of speeds. The Aerotech traversing mechanism consisted of a carriage (on which the jet was mounted) moving along a monorail (with a built-in encoder to send position feedback to controller), and a linear motor guided by a U-channel magnet track paralell to the monorail (schematic view in Fig. 3.14), spanning the tank width. The motor provided the driving force in the direction of motion, overcoming the friction of the carriage, the drag of the jet and the acceleration/deceleration forces, while the carriage bore the normal load due to weight of the components. The assembly operated as a whole by integrating the carriage and the linear motor, which also allowed the encoder to send the position feedback to the controller system.

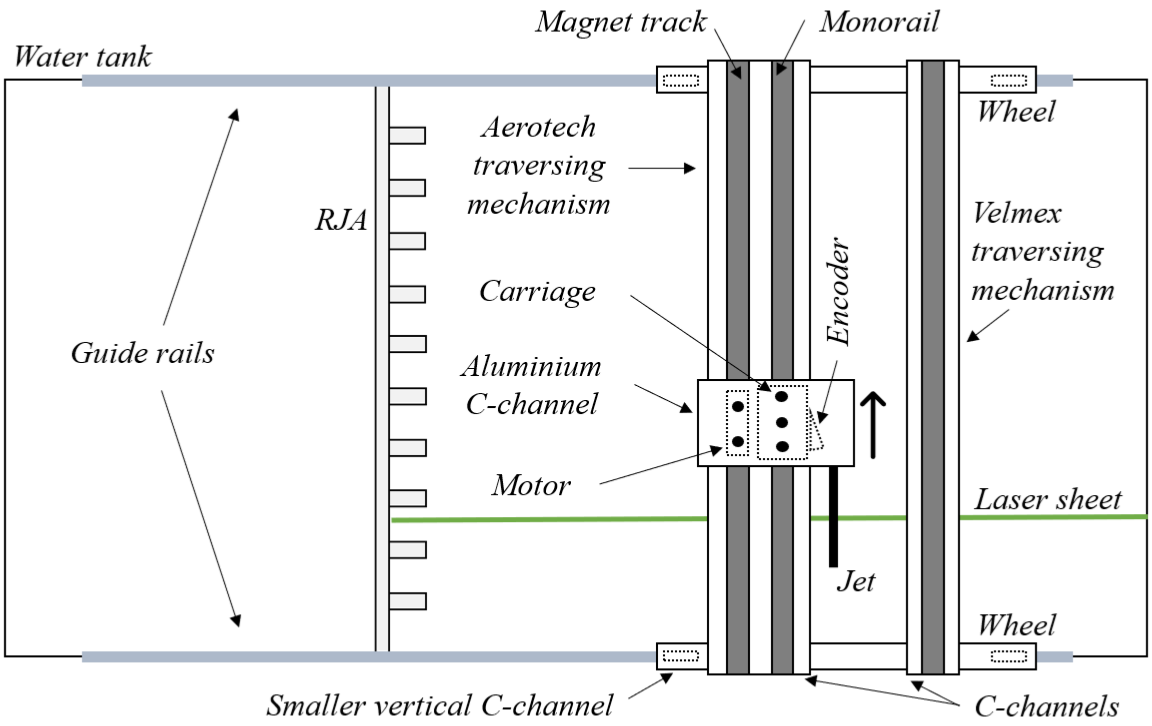

Figure 3.14: Schematic of the Aerotech and Velmex traversing mechanisms above the tank - top view (not to scale).

The monorail and the magnet track were mounted on an aluminium C-channel in parallel that was parallel to another C-channel on which the Velmex traversing mechanism (used for positioning the jet in the first setup) was mounted (sec. 3.1.3). Both C-channels were fixed perpendicularly on top of two smaller C-channels that could roll along the tank on two guide rails. The traversing mechanisms were positioned parallel to the RJA plane and could be moved manually along the tank. Two limit switches one at each end of the Aerotech traversing mechanism avoided collisions between the jet and the tank side walls.

The motor and the carriage were connected with a short aluminium C-channel, screwed on top of the both components. Holes were drilled on the C-channel to reduce its weight and hence the load on the assembly. The Aerotech traversing mechanism was controlled by an Aerotech SOLOIST CP10 controller that drove the linear motor along the magnet

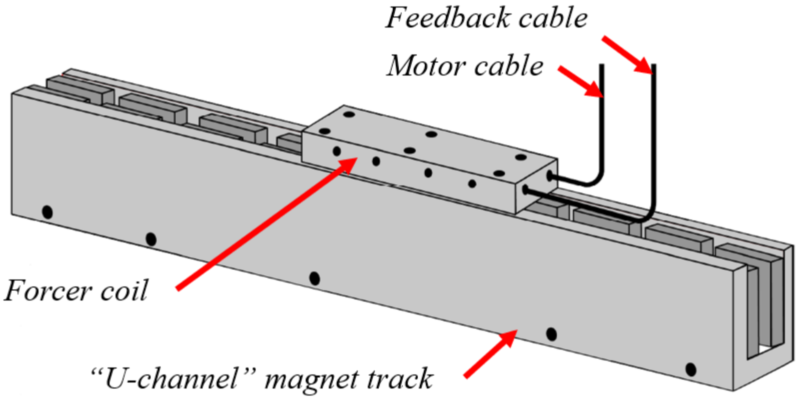

Figure 3.15: Aerotech BLMUC-143-A linear DC motor and magnet track.

track. The carriage position data was read by the encoder and sent to the controller as the position feedback signal, without which the controller did not work.

The motor was an Aerotech BLMUC-143-A linear DC motor - a moving forcer coil assembly (with Hall-effect devices) that provided horizontal force along the U-channel magnet track induced by its magnetic field (Fig. 3.15). The motor moved along the magnet track and drove the carriage (and hence the jet) along the monorail. The force was applied in the direction of the motion and thus the motor did not bear normal loads. The forcer coil assembly was a compact, reinforced ceramic epoxy structure that moved along the U-channel magnet track without contacting the channel, therefore eliminating the wear problems and maintenance. The U-channel magnet track consisted of 3 MTUC416 tracks in series with 52.0 mm × 20.8 mm cross-section and 1248 mm in length. There was an air supply to cool the motor, although it could provide a continuous force up to 39.8 N without the air supply. A thermal sensor stopped the forcer in case of overheating.

The monorail/carriage system was a Schneeberger Monorail AMSD-4A (Fig. 3.16) which consisted of a linear bearing carriage to bear the normal load with an integrated differential digital encoder to read the carriage position, and a monorail on which the carriage was traversed. The absolute position of the jet was measured by the encoder reading a fully integrated measuring strip on the monorail. The measuring strip was a fine incre-

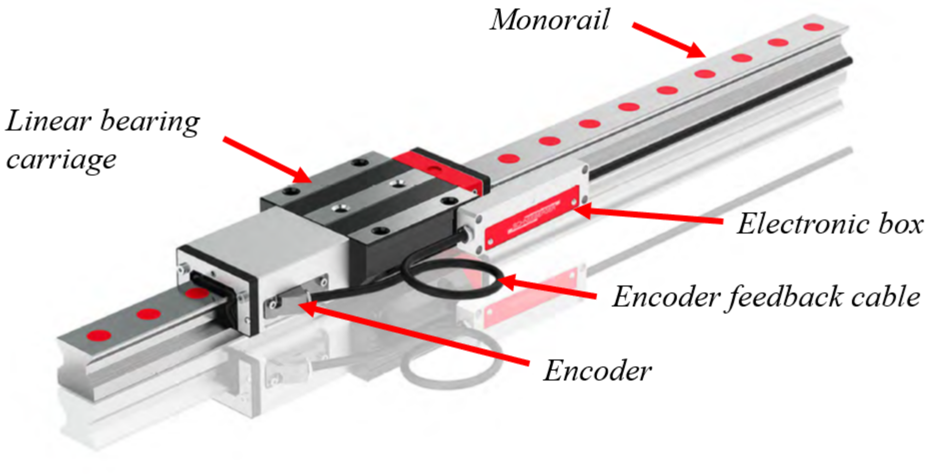

Figure 3.16: Schneeberger Monorail AMSD-4A.

mental track with alternate N and S poles at 200 μm intervals, and reference marks at 20 mm spaces. Any relative movement between the encoder sensor and the measuring scale changed the field strength, causing measurable change in electrical resistance. The resolution of the encoder was 1 μm. Occasional lubrication of the linear bearing in the carriage was required.

The motor power cable, the motor control signal cable, the air line for cooling the motor, and the encoder signal cable were passed though and protected by an Igus plastic cable track. The cable track was fixed to the short aluminium C-channel and moved with the carriage. The motor power cable was directly connected to the SOLOIST CP10 controller. The cables for the motor control signal, the encoder signal and the limit switches were connected to a terminal block which was connected to the feedback of the controller. The controller was connected to the USB port of a computer system. The SOLOIST CP10 controller parameters (such as acceleration and deceleration) were set by the Soloist Configuration Manager software, and a LabVIEW code was used to control the distance and the speed at which the jet was traversed.

The jet was positioned and aligned on the Aerotech traversing mechanism the same way as that in the turbulent jet experiments (Secs. 3.1.3 and 3.2.2). The horizontal extension of the jet was 450 mm (15d) to allow the jet flow to develop, and to minimize the flow disturbances by placing the vertical extension of the jet always behind the laser sheet. The jet was fed through a 25.4 mm diameter plastic tubing (19 mm inner diameter) that entered directly at the base of the horizontal extension of the jet and extended for 50 mm, which was sealed by o-rings to prevent any leakage. The jet flow rate was adjusted using a ball valve and was measured using a flow meter (Blue-White F400) with a ±5% error.

During a test drive, it was important to ensure a continuous dyed fluid at the jet exit by running the jet for a few seconds prior to the start of the towing. The recording was triggered once the tip of the jet crossed the laser sheet, and the jet flow was stopped at the end of its traversing distance to avoid a momentum-driven jet flow. The optimal flow rate, achieved by considering the minimum jet exit velocity that generated a continuous jet flow, was 0.757 l/min. The acceleration/deceleration of the jet towing was $1\ \mathrm{m/s^2}$, and the traverse speed and the traverse time were 18 mm/s and 35.5 s, respectively.

3.4 Data acquisition and post-processing

The data from the turbulent jet experiments are used to study the dynamics and mixing of a turbulent jet in a HIT ambient. In the second set of experiments, the diffusion of a momentumless patch of a passive scalar in the HIT ambient is investigated. In this section, the data acquisition process and the post processing methods are described for both sets of experiments.

3.4.1 Data sampling

The instantaneous fluorescent signals were recorded on a 12-bit, 4 MP monochrome CMOS camera (pco.dimax), controlled by the Camware software, with which the acquisition rate, exposure time, and exposure delay were set. The acquisition rate (i.e. temporal resolution) was set to 30 Hz and 50 Hz in the turbulent jet experiments and the turbulent diffusion experiments, respectively. The acquisition time consisted of an exposure time (i.e. 30 ms and 19.9 ms for 30 Hz and 50 Hz, respectively) and a short interval to convert the detected light to intensity counts in the camera (3.33 ms and 0.1 ms for 30 Hz and 50 Hz, respectively). The exposure delay was set to zero to minimize the discrepancies between the incident signal and the recorded intensity. The laser sheet was generated at 1600 Hz with each beam scan lasting for 625 μs, hence 48 and 32 beam scans were captured during the 30 ms and 19.9 ms of the exposure time per image in the turbulent jet experiments and in the turbulent diffusion experiments, respectively. Each image was a 2016$\times$2016 matrix whose elements captured the fluorescent light intensity.

In the turbulent jet experiments, the PLIF tests were carried out at axial distances of x/d = 20, 30, 40, 50, and 60 for two jets with Re = 10600 and 5800 in a quiescent and in a HIT ambient. The length of each experiment was determined by the required number of images to reach convergence for the first- and-second-order scalar concentration, and was limited by the finite storage capacity of the camera. Each 9 seconds of an experiment (with a 30 fps rate) was a full Tagged Image File Format (TIFF or TIF) image, consisting of 263 PLIF images, occupying a 1.99 GB space on the camera memory. The lengths of the experiments were selected as a multiplies of 9 seconds for more convenient data analysis and post-processing. In the quiescent ambient, data sets for a period of 27 s, 45 s, 63 s, 81 s, and 100 s were obtained resulting in a total of 789, 1315, 1841, 2367, and 2893 PLIF images, respectively, while in the HIT ambient, five sets of PLIF tests, each obtained for 170 seconds containing 4997 images, were taken at each axial position. Figure 3.17 shows an example of the centerline concentration convergence in the quiescent and in the HIT ambient at x/d = 50 for the Re = 5800 jet.

In the turbulent diffusion experiments, it was ideal to remove the advective transport of the passive scalar, which was approximately achieved at the beginning of the test before the vortex shedding caused by towing of the jet disturbed the measurement plane. The duration of the tests was limited by vortices disturbing the measurement plane, and also by the scalar patch being advected out of the field of view in the turbulent ambient. The concentration field of the scalar patch was obtained for $0 \leq t \leq 4$ s, at a sampling rate of 50 fps, resulting in 200 PLIF images (t = 0 denotes the time at which the tip of the jet

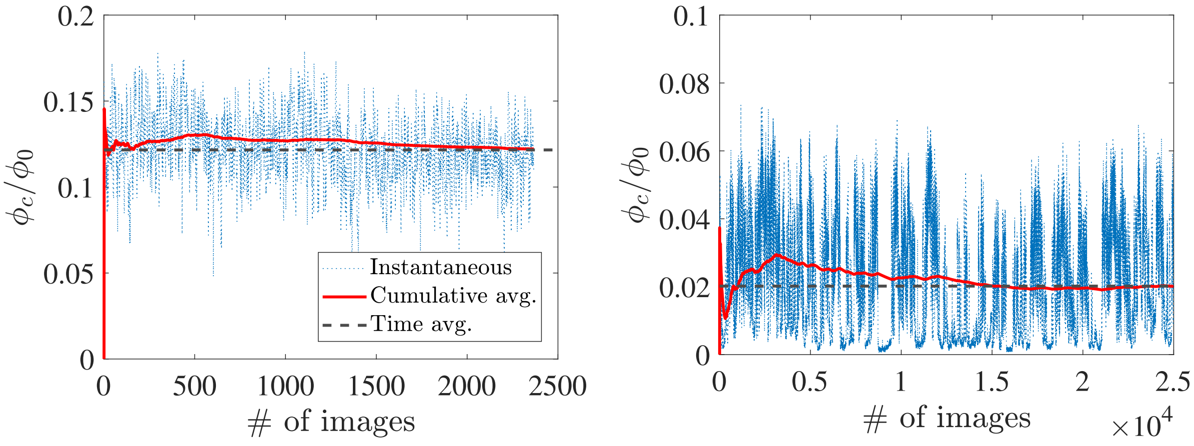

(a) **(b)**

Figure 3.17: Example of convergence of the jet centerline concentration in the (a) quiescent, and the (b) HIT ambient. Data for $Re = 5800$ at $x/d = 50$.

crossed the laser sheet). One and six PLIF tests were conducted in the quiescent ambient and in the turbulent ambient, respectively. The evolution of the concentration field of the patch is obtained at $t = 0.2, 1, 1.8, 2.6, 3.4$ s, using the average of 6 and 20 PLIF images at each time for the quiescent and for the turbulent ambient cases, respectively, to smooth the fluctuations of the instantaneous concentration field.

3.4.2 Post processing

Data analysis and post-processing were performed on a 64-bit system with Intel (R) Core (TM) i7-8700 CPU @ 3.20 GHz processor and a 64 GB RAM. First, the background intensity level was subtracted from the images and the calibration coefficients were applied to convert the intensity counts to the actual concentration values in each pixel. Custom MATLAB codes were employed to obtain the statistics of the passive scalar field of the turbulent jet and the scalar patch in the quiescent and in the HIT ambient. For the turbulent jet experiments, the analyses were carried out on a profile equidistant from the RJA plane, passing through either the jet centerline (i.e. the jet axis) or the jet centroid (see Sec. 3.4.3), which was subject to an approximately constant level of the ambient turbulence intensity. For the turbulent diffusion tests, the analyses were performed for all the radial profiles passing through the jet centroid to account for the non-axisymmetric spatial variation of the scalar patch in the turbulent ambient (see Sec. 5.2.2).

In the turbulent jet study (Ch. 4), the evolution and structure of the jet, as well as the entrainment and mixing of the jet in the HIT ambient are compared to those in the quiescent ambient. To this end, the mean concentrations, the rms concentrations and the concentration half-width of the jet are studied. The self-similarity and the self-preservation of the jet in the HIT ambient are assessed in terms of the power-law constants and the shape of the radial profiles. The statistics of the scalar mixing in the HIT ambient have been assessed based on the intermittency, the probability density functions (PDFs) and the cumulative density functions (CDFs) of the scalar concentrations. A discussion on the entrainment of the jet in the HIT ambient is carried out based on the present passive scalar data and velocity data from Khorsandi et al. (2013).

In the turbulent diffusion experiments (Ch. 5), the passive scalar field of the momentumless scalar patch is studied in terms of its mean concentration, the rms concentration, the characteristic width of the concentration field, the intermittency, and the PDFs/CDFs of the centroidal concentrations. The temporal evolution of the passive scalar field in the turbulent ambient is compared to that in a quiescent ambient. In the discussion, the results of the turbulent diffusion of the scalar patch are related to the dispersion and mixing of the turbulent jet (beyond breakup) in the HIT ambient.

3.4.3 Analysis method

To obtain the statistics of the passive scalar fields of the jet and the scalar patch, an Eulerian averaging and a centroidal averaging are used for the jet, and only the centroidal averaging for the scalar patch. The Eulerian method is a classical spatial average that provides the ensemble-averaged concentrations at a particular location relative to the jet axis. The centroidal method is a conditional average, conditioned on the location of the instantaneous centroid of the jet or the momentumless scalar patch. The centroidal analysis is applied because the previous studies of the jet in the HIT ambient showed that the jet path meanders due to lateral advection by the large ambient eddies, and that the position of the instantaneous centroid of the jet varies significantly from that of the jet in a quiescent ambient (i.e. the jet axis) (Khorsandi et al., 2013; Perez-Alvarado, 2016; Lai et al., 2019).

While the large eddies in the HIT ambient advect the jet laterally and cause its path to meander, the smaller eddies modify the jet structure and mixing. The Eulerian average includes the composite effects of the different-sized eddies on the jet dynamics, and thus obscures the details of the jet structure. However, the centroidal average, by following the meandering path of the jet (and the scalar patch), includes primarily the influence of the smaller eddies on the jet. In the centroidal average, the structure of the jet can be effectively deduced and a more accurate assessment of the dynamics of the jet in the HIT ambient is attainable (Gaskin et al., 2017). It is noted that at high levels of turbulence intensity of the background, the effect of the large eddies could not be fully removed due to possible discontinuities in the jet structure.

Chapter 4

The dynamics of an axisymmetric turbulent jet in ambient turbulence interpreted from the passive scalar field statistics

In this chapter, dynamics of an axisymmetric turbulent jet in ambient turbulence have been interpreted from the passive scalar field statistics. The results of this chapter are published in a paper entitled as ”The dynamics of an axisymmetric turbulent jet in ambient turbulence interpreted from the passive scalar field statistics” in Physics of Fluids.

Abstract

The effect of approximately homogeneous isotropic turbulence on the dynamics of an axisymmetric turbulent jet (Re = 10600 and 5800) in an ambient with a negligible mean flow is interpreted from the statistics of the passive scalar field. The ambient turbulence is generated by a random jet array and scalar concentrations are measured in orthogonal cross sections of the jet using planar laser-induced fluorescence. Statistics of the scalar field of the jet in a turbulent ambient are compared to those in a quiescent ambient, us-

ing classical Eulerian averages and those conditioned on the jet centroid. A two-region model for the jet structure in ambient turbulence is proposed based on the centroidal statistics. Following the developing region of the jet, the ambient turbulence disrupts the jet structure, due to modulation of the jet interface, meandering of the jet by large eddies, and entrainment of the turbulent ambient fluid, resulting in a faster concentration decay and reduced entrainment compared to the quiescent ambient. Further downstream, once the ambient turbulence has destroyed the jet, only molecular and turbulent diffusion modify the scalar concentrations. The regions' relative lengths depend primarily on the relative turbulence intensity (ξ) between the ambient and the jet, as assessed using centroidal analysis, which removes the effect of the relative length scale ($\mathcal{L}$) on the jet behavior in the turbulent ambient. The centroidal scalar statistics reveal self-similarity and self-preservation in mean scalar properties before jet breakup, which occurs abruptly once $\xi > 0.5$. The smaller scales of ambient turbulence modulate the jet boundary and, when entrained, lead to a wider range of centerline concentrations and root mean square concentrations, which are hypothesized to increase local concentration gradients within the jet and reduce jet mixing.

4.1 Introduction

Scalar mixing in turbulent shear flows (jets, plumes, wakes, and boundary layers) is of interest in industrial and environmental contexts and has been studied extensively in a quiescent ambient. A jet in a quiescent ambient, after a zone of flow establishment, is self-similar and its mean momentum drives entrainment into the jet with a global entrainment velocity, E_v, that is proportional to the characteristic jet velocity (Morton et al., 1956) with a constant of proportionality, α, of (0.1) (e.g. see van Reeuwijk and Craske (2015)). Entrainment, the transport of ambient fluid into the turbulent shear flow, occurs by engulfment, a large-scale inviscid process (Townsend, 1966; Dahm and Dimotakis, 1987) and by nibbling at the jet/ambient interface, a small-scale viscous diffusion process

(Corrsin and Kistler, 1955; Mathew and Basu, 2002). The entrainment of ambient fluid results in an outward propagation of the interface between the jet and the ambient fluid at a boundary velocity, E_b (da Silva et al., 2014).

It has long been assumed (and is still often maintained) that the release of a jet into a turbulent ambient flow will increase its rate of dilution through superposition of jet-driven entrainment and turbulent diffusion. This was an expedient approach simplifying modeling in practical applications to predict, for example, air/fuel ratios for combustion or dilution for pollutant dispersion. Despite challenges in producing ambient turbulence for a laboratory study, Gaskin et al. (2004) demonstrated experimentally that turbulence in ambient flows serves to disrupt the jet flow, resulting in reduced dilution. This was the first experimental evidence in support of Hunt's argument in 1994 (Hunt, 1994), that any forcing, such as turbulence in the ambient, tending to break up a jet or plume would reduce entrainment. The reduced entrainment shown experimentally for a jet in a shallow co-flow (Gaskin et al., 2004) was confirmed for an axisymmetric jet (Khorsandi et al., 2013; Perez-Alvarado, 2016) and a buoyant jet (Lai et al., 2019).

Breakup of the jet, defined as the condition at which momentum-driven entrainment of the jet stops, is hypothesized to occur once the jet or plume turbulence has decreased to that of the ambient Hunt (1994), which has been observed in jets and plumes (Ching et al., 1995; Guo et al., 2005; Cuthbertson et al., 2006; Khorsandi et al., 2013; Perez-Alvarado, 2016; Lai et al., 2019). In experiments, in which a jet issues toward an oscillating grid-generated turbulence field, the breakup is very rapid due to a simultaneous decrease in jet turbulence as the ambient turbulence increases (Ching et al., 1995; Guo et al., 2005; Cuthbertson et al., 2006). In jets and plumes, the turbulence in the ambient increases the rate of decay of the mean centerline velocity and passive scalar concentration, and increases the root mean square (rms) of the velocity and the concentration. The rate of width growth is increased (but less than the increase in the rate of decay of the mean centerline properties) (Law and Wang, 2000; Gaskin et al., 2004; Khorsandi et al., 2013; Perez-Alvarado, 2016; Lai et al., 2019), while the mass flow rate decreases (Perez-Alvarado, 2016). Similarly, the velocity deficit in a wake decays more quickly (Legendre et al., 2006; Amoura et al., 2010) and its width growth increases once the integral scale of the ambient turbulence is larger than the width of the wake (Eames et al., 2011b).

The effect of the relative turbulence intensity and the relative length scale between the ambient and the flow was initially observed for boundary layers (Hancock and Bradshaw, 1989). In wakes, the ambient turbulence intensity is the dominant factor (Pal and Sarkar, 2015; Kankanwadi and Buxton, 2020). There is hypothesized to be little effect of the ambient turbulence on the jet or plume flow close to the exit, where it is less intense than the jet turbulence. However, its increasing impact with downstream distance due to an increasing relative turbulence intensity will result, at some point, in the breakup of the jet and destruction of its structure (Hunt, 1994). After the jet structure is destroyed, a passive scalar will then only disperse due to detrainment by turbulent and molecular diffusion (Gaskin et al., 2004; Khorsandi et al., 2013; Perez-Alvarado, 2016). It should be noted that a maintained jet structure refers to the preservation of the jet mean momentum and, therefore, its large-scale vorticity structures. These large structures, in turn, induce the global entrainment velocity, E_v (Philip and Marusic, 2012).

A jet, whose integral scale (i.e., width) is less than the largest length scale of the ambient turbulence, is advected by the large scales causing its path to meander, while the jet structure/entrainment is affected by the smaller scales (Hunt, 1994; Gaskin et al., 2017). Studies of jets and plumes in ambient turbulence, using Eulerian averaging (all to date), include both the effect of large scales advecting the jet and the effect of the small scales of the ambient turbulence. An increase in jet spreading observed in Eulerian averages of strong jets in a coflow with low levels of ambient turbulence has been interpreted as increased entrainment citing the superposition of jet-driven entrainment and ambient turbulent diffusion (Wright, 1994; Moeini et al., 2020). Jet entrainment (or resulting dilution) is driven by the jet's mean momentum (Morton et al., 1956), whereas detrainment by turbulent diffusion is driven by the scalar concentration gradient and facilitated by the ambient turbulence diffusivity. Experimental observations of jets in ambient turbulence have not found self-similarity of first-order properties (Eulerian averages) (Khorsandi et al., 2013; Perez-Alvarado, 2016), although, in a strong jet in a coflow with very low relative turbulence intensity, self-similarity was observed up to a relative length scale of the ambient to the jet of one (Moeini et al., 2020).

In real flows, turbulence is generally inhomogeneous and anisotropic. However, the study of shear flows in homogeneous isotropic turbulence (HIT) allows for analysis in a simplified laboratory context. That being said, despite being a simple concept, HIT is challenging to realize in a laboratory due to the necessity of a mean velocity gradient for the initial production of turbulent kinetic energy (TKE) (Perez-Alvarado, 2016). Researchers have used different methods to create the closest approximations to HIT, such as oscillating grids (De Silva and Fernando, 1994), active/passive grids (Mydlarski and Warhaft, 1996; Lavoie et al., 2007), and loudspeakers (Webster and Brathwaite, 2004). However, grid-generated turbulence suffers from large mean flows, and the loud speaker systems can maintain the HIT in only a very small region. The introduction of the random jet array (RJA) enhanced the quality of the turbulence, minimizing the mean flow and increasing the extent of the HIT region (Variano and Cowen, 2004; Variano et al., 2008; Carter et al., 2016).

In the current study, the effect of the different intensities of HIT on the evolution and structure of an axisymmetric turbulent jet is investigated through a study of the passive scalar field, building on the work of Khorsandi et al. (2013) and Perez-Alvarado (2016) (same turbulence properties and jet Reynolds numbers). Scalar statistics of the flow are analyzed using (i) a classical Eulerian average—which is a stationary spatial average—and (ii) an average conditioned on the centroid of the instantaneous jet cross section, hereafter referred to as Eulerian average and centroidal average, respectively. While the Eulerian average provides information on the spatial dispersion of the scalar concentration relative to the jet axis, the centroidal statistics provide information on the jet dynamics by separating the effect of the larger scales, which advect the jet causing its path to meander, from the smaller scales, which disrupt jet entrainment and mixing (details in Sec. 4.3).

The experimental set-up of a jet issuing into a HIT with negligible mean flow generated with an RJA is described in Sec. 4.2. The passive scalar field of the jet is experimentally measured using the planar laser induced fluorescence (PLIF) method – as detailed in Sec. 4.2 and analyzed using centroidal averages and Eulerian averages, Sec. 4.3. In Sec. 4.4 the measurement technique is validated. Section 4.5 presents the results, and a discussion of the effect of the HIT ambient on the jet dynamics as compared to the jet in a quiescent ambient is provided. Section 4.6 summarizes the conclusions.

4.2 Experimental methods

A turbulent axisymmetric jet was released into a quiescent and a HIT ambient with negligible mean flow. The PLIF method was used to observe the evolution of the passive scalar field in cross sections of the jet. A detailed description of the experimental facility, the implementation of the PLIF method, and the data acquisition follows. Figure 4.1 is a schematic view of the experimental apparatus, and examples of instantaneous jet cross sections in the quiescent and the HIT ambient are shown.

4.2.1 Experimental facility

The experiments were carried out in a 1.5 m × 2.4 m × 1 m subsection of a large glass water tank (1.5 m × 6 m × 1 m) open at the top (i.e. the free surface is at ambient pressure). The water in the tank was either quiescent, after being left to settle for sufficient time after slow filling, or turbulent (HIT). An approximately homogeneous and isotropic turbulence with negligible mean flow was generated in the tank by a random jet array (RJA) (Variano and Cowen, 2004; Variano et al., 2008), but at a larger scale (Perez-Alvarado et al., 2016). The RJA is an array of six rows and ten columns of bilge pumps (Rule 25D, 500 GPH) mounted on a $1 \times 1.5\ \mathrm{m}^2$ vertical sheet of high-density polyethylene. The uniform spacing of the pumps in the horizontal and vertical directions (M = 150 mm, center to center distance), and a reflective boundary condition reduces the occurrence of secondary flows (Fernando and De Silva, 1993; Variano et al., 2008).

The turbulence was generated by the RJA using an algorithm to individually turn the jets on and off for periods of time randomly selected from a normal distribution with a $(\mu_{on}, \sigma_{on}) = (12, 4)$ s and $(\mu_{off}, \sigma_{off}) = (108, 36)$ s (Variano et al., 2008; Perez-Alvarado et al., 2016). Thus, 10 % of the pumps operate on average at any given time. Downstream of the RJA, the jets merge and create an approximately HIT ambient. As the intake and discharge of each pump occur simultaneously into the same control volume, there is zero net mass flow rate through each pump, resulting in an overall zero-mean flow in the tank. The random algorithm for the RJA generated a flow that most closely approximated a zero-mean flow HIT as compared to several alternative algorithms (Khorsandi et al., 2013; Perez-Alvarado et al., 2016).

4.2.2 Jet apparatus

A round turbulent jet with Re = 10600 and 5800 issued into the water tank parallel to the RJA sheet, such that the turbulence level was constant along the jet centerline in the downstream direction. The jet issued from a copper tube with 8.51 mm inner diameter (d), which extended vertically for 1.2 m and, after a 90° bend, extended horizontally for 0.2 m ($\sim 24\,d$) achieving a fully developed flow at the exit. A constant-head reservoir—located 3m above the jet—fed the jet flow, maintaining a constant flow rate and, thus, a constant Reynolds number. The jet was turned on and off with a solenoid valve, while a ball valve was used to adjust the flow rate, measured using a flow meter (Omega FL50002A). The jet measurements were made at orthogonal cross sections of the jet located at downstream distances of x/d = 20, 30, 40, 50, and 60. The jet was mounted on a traversing mechanism to precisely adjust its position in the streamwise (x) and vertical (z) directions. The jet discharged parallel to the RJA sheet at a transverse distance of 1.10 m (i.e. y/M = 7.3), where the turbulent kinetic energy (TKE) of the ambient was k_{HIT} = 4.4 $\mathrm{cm^2 s^{-2}}$ (Khorsandi

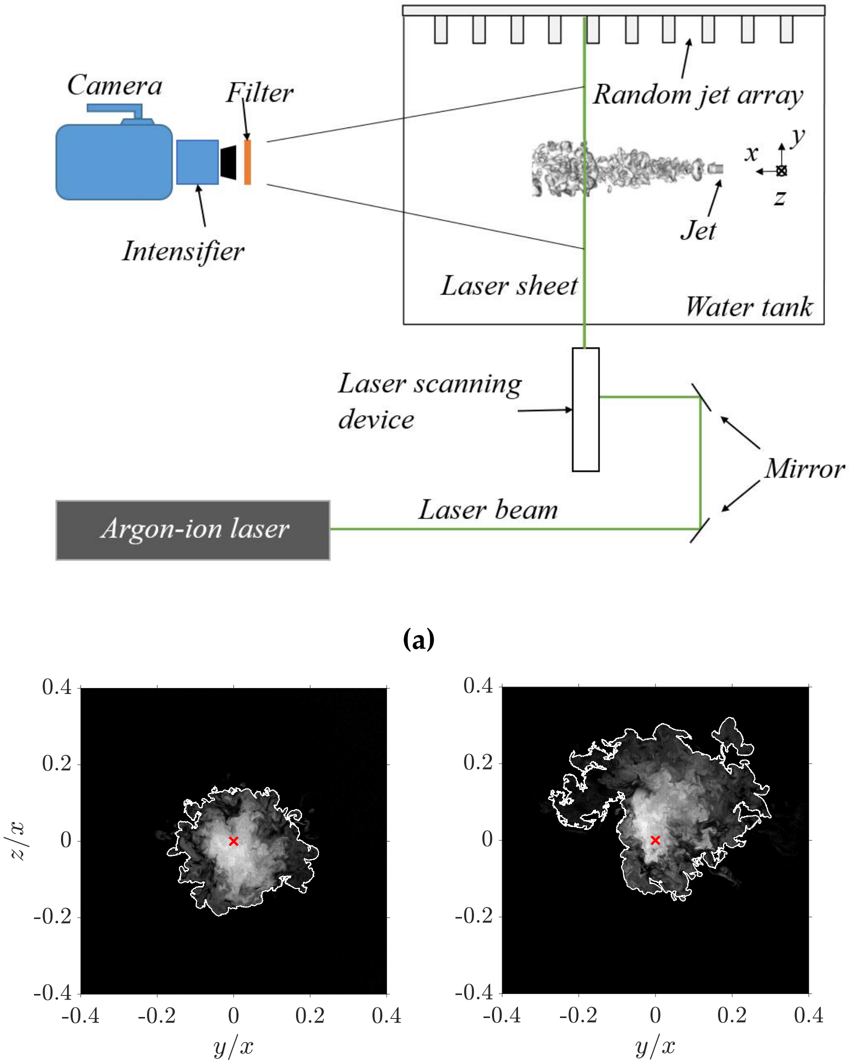

(a)

(b)

(c)

Figure 4.1: (*a*) Schematic of the PLIF apparatus, and examples of instantaneous jet cross-section in (*b*) the quiescent, and (*c*) the turbulent ambient. The jet/ambient interface is shown with white contours using a threshold value of $\phi_t = 0.15\ \overline{\phi_c}$, where $\overline{\phi_c}$ is the the mean centerline concentration in the quiescent ambient, and the centroidally averaged concentration in HIT ambient, respectively (Section 4.3). Red cross denotes the jet axis.

et al., 2013). The experimental parameters are provided in Table 4.1. For more details on the RJA setup and the jet apparatus, the reader is referred to Lavertu et al. (2008), Khorsandi et al. (2013), and Perez-Alvarado (2016).

Table 4.1: Experimental parameters. Note that $Re = U_0 d/\nu$, and $Re_{\lambda,\,HIT} = \left(\sqrt{150}\,k_{HIT}\,L_{HIT}/\nu\right)^{1/2}$. Here $\mathcal{L}_{5800}$ and ξ_{5800} denote the length scale and turbulence intensity ratios of HIT to Re = 5800 jet at the five cross-sections, respectively. Similarly, $\mathcal{L}_{10600}$ and ξ_{10600} are defined for Re = 10600 jet.

Jet Reynolds number	Re	5800, 10600
Schmidt number	Sc	2000
Jet exit velocity	U_0	0.682, 1.245 m s^{-1}
Jet exit inner diameter	d	8.51 mm
Lateral jet position to RJA	y/M (M = 150 mm)	7.3
Ambient TKE (at $y/\mathrm{M} = 7.3$)	k_{HIT}	4.4 $\mathrm{cm}^2\mathrm{s}^{-2}$
Ambient length scale (at $y/\mathrm{M} = 7.3$)	L_{HIT}	110 mm
Ambient turbulent Reynolds number	$Re_{\lambda,\,HIT}$	168
RJA operating algorithm	(μ_{on}, σ_{on}), $(\mu_{off}, \sigma_{off})$	(12, 4) s, (108, 36) s
Axial position of cross-sections	x/d	20, 30, 40, 50, 60
Length scale ratio	$\mathcal{L}_{5800}$	5.8, 4.1, 2.9, 2.5, 2.2
	$\mathcal{L}_{10600}$	6.3, 4.5, 3.1, 2.5, 2.2
Turbulence intensity ratio	ξ_{5800}	0.29, 0.39, 0.52, 0.58, 0.73
	ξ_{10600}	0.16, 0.21, 0.31, 0.34, 0.43
PLIF spatial resolution	-	$4.7\eta - 1.4\eta$, $7.3\eta - 2.2\eta$
Field of view	FOV	640 mm × 640 mm
Sampling frequency	-	30 Hz

At this point, it is worth mentioning the range of ratios of, the HIT to the jet, of the length scales ($\mathcal{L}$) and the turbulence intensities (ξ). The relative length scale is approximated by

$$\mathcal{L} = L_{HIT}/b_{\phi,1/2}, \tag{4.1}$$

where L_{HIT} is the integral length scale of the HIT ambient at $y/\mathrm{M} = 7.3$ and $b_{\phi,1/2}$ is the concentration half-width of the jet in the quiescent background (Sec. 4.4). In the current study, $L_{HIT} = 110$ mm and is estimated using

$$L_{HIT} = \int_0^\infty \frac{\overline{u_{HIT}(\mathbf{x})\,u_{HIT}(\mathbf{x} + r e_x)}}{u^2_{rms,HIT}}\,\mathrm{d}r, \tag{4.2}$$

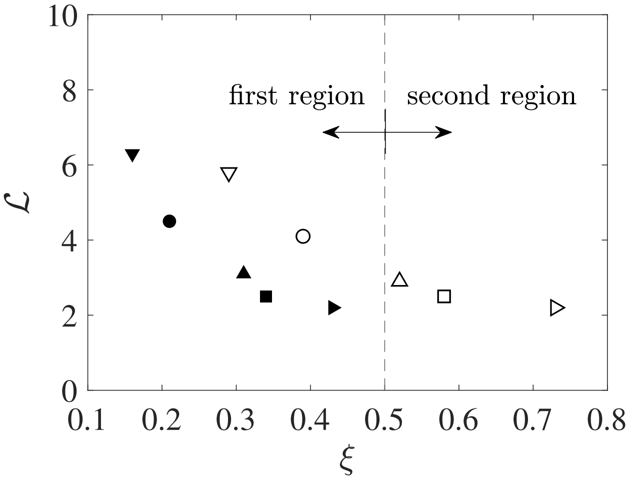

Figure 4.2: Variation of the relative turbulence intensity and the relative length scale at each downstream location of the two jets. Filled symbols: $Re = 10600$, open symbols: $Re = 5800$. ▽, x/d = 20; ○, x/d = 30, △, x/d = 40; □, x/d = 50; ▷, x/d = 60.

where u_{HIT} is the axial velocity fluctuation of the RJA turbulence and re_x denotes some displacement lag r in the direction of the x-coordinate unit vector (Khorsandi et al., 2013). The relative turbulence intensity is defined as

$$\xi = u_{rms,HIT}/u_{rms,jet}, \tag{4.3}$$

where the velocity information is taken from the study of Khorsandi et al. (2013). The two selected jet Reynolds numbers allowed us to study the jet behavior above and below the transition Reynolds number, i.e., $Re = 10^4$ (Dimotakis, 2000). Also, it granted a wide range of relative turbulence intensity (0.16 < ξ < 0.73) and relative length scale (2.2 < $\mathcal{L}$ < 6.3) ratios between the HIT ambient and the jet (Table 4.1). Figure 4.2 depicts the variation of $\mathcal{L}$ versus ξ at each downstream location for the two jets. The ratios of length scale and turbulence intensity between the HIT ambient and jet approach unity ($\mathcal{L}$ from larger values and ξ from smaller values) as the jet develops downstream, increasingly disrupting the jet structure (Hunt, 1994).

4.2.3 PLIF apparatus

The PLIF method was employed to obtain the concentration field of a passive scalar in the jet in orthogonal cross sections. A small quantity of fluorescent dye (disodium fluorescein, Sc = 2000) was mixed into the jet water supply. A continuous mode 1W argon-ion laser (Coherent, Innova 90) was used to illuminate the flow cross sections with an excitation wavelength of 514.5 nm. The laser beam was directed into a laser scanning device consisting of (i) a 12.7mm dielectric mirror (Newport 5151), (ii) a focusing lens with a 1.5m focal length, plano-convex lens (PLCX-25.4-772.6-C), and (iii) a high-speed rotating mirror (Lincoln Laser Company DT-08-236-019). The eight-sided polygonal rotating mirror rotated at 12 000 rpm, generating a laser sheet with 1600 scans per second of the laser beam over the measurement area. The use of a high-speed rotating mirror to generate the light sheet and low dye concentrations minimized potential sources of PLIF errors, such as photobleaching, thermal blooming, and attenuation (Lavertu, 2006; Perez-Alvarado, 2016).

Instantaneous fluorescence signals were recorded using a 12 bit CMOS camera (pco. dimax). The camera had a resolution of 2016 $\times$ 2016 pixels, and the acquisition frequency was set to 30Hz. The incident light first reached a 50mm diameter 550 nm longpass color filter (ThorLabs FGL550) attached to the camera lens (Pentax 50mm f/1.4) to filter any scattered laser light and, therefore, transmitted only the fluorescence signal through the camera lens. An image intensifier (Video Scope VS4-1845) was placed between the camera and the camera lens to increase the light sensitivity of the system. The coupling of the intensifier and the camera reduced the size of the detection area to a central circle with 1601 pixel diameter, covering a circular field of view (FOV) with a diameter of about 640 mm. The rather large FOV was necessary to capture the complete orthogonal spatial extent of the jet subjected to the HIT ambient at large downstream distances. The spatial resolution of the PLIF experiments was about 0.4 mm $\times$ 0.4 mm per pixel (Table 4.1). This resolution corresponds to $1.4\eta - 4.7\eta$ for Re = 5800 and $2.2\eta - 7.3\eta$ for Re = 10600, where $\eta = (\nu^3/\overline{\epsilon})^{1/4}$ is the centerline Kolmogorov length scale for the quiescent background case. It is worth noting that the Batchelor microscale is the appropriate length scale for resolving the scalar field at high-*Sc* flows, which was not attained in the present experimental setup. However, resolution comparable to η has been shown to be sufficient to capture the mean and rms concentration profiles (Kohan and Gaskin, 2020). The lowest resolution occurs at the closest downstream distance ($x/d = 20$) since the turbulent length scales, including η, increase as the jet develops (van Reeuwijk and Holzner, 2014). ν and $\overline{\epsilon}$ denote the kinematic viscosity ($10^{-6}\,\mathrm{m^2\,s^{-1}}$ for water) and mean centerline dissipation rate, respectively. The latter is calculated using the empirical relation of Friehe et al. (1971)

$$\overline{\varepsilon} = 48\frac{U_0^3}{d}\left(\frac{x - x_0}{d}\right)^{-4}, \tag{4.4}$$

where U_0 and x_0 denote the nozzle exit velocity and the virtual origin (see Sec. 4.4), respectively. It should be noted that the estimated values of $\overline{\epsilon}$ (and therefore η) are only used to calculate the PLIF pixel spacing at each measurement station (Table 4.1).

Although the laser power was constant during the experiments, the laser intensity, defined as the ratio of the laser power to the cross section of the laser sheet, decayed with the laser sheet expansion (angle of expansion of 45°). Furthermore, the image intensifier caused higher light sensitivity in the central region of the image as compared to the edges. The images were, therefore, calibrated pixel by pixel to convert the light intensity levels to dye concentration values. Over a large range, the relationship between the dye concentration and the emitted light intensity is nonlinear (Guilbault, 1973); however, at low concentration levels (as is in the present PLIF experiments), the intensity–concentration relationship is linear. Therefore, a linear curve can be fitted such that $\phi = AI + B$, where I is the light intensity value of the pixel, A and B are the calibration coefficients extracted from the calibration test, and ϕ denotes the concentration value. Details of the calibration and PLIF tests can be found in Perez-Alvarado (2016).

PLIF is prone to measurement errors, including attenuation, photobleaching, trapping, thermal blooming, and inertial effects. Attenuation of the laser beam occurs when (a part of) the laser energy is absorbed by the fluorescent dye when the laser beam crosses through non-negligible volumes of dyed fluid before it reaches the measurement location. Photobleaching is the reduction in fluorescence intensity due to constant laser irradiation. Trapping occurs if the emitted fluorescence light at the measurement section is absorbed by dye at some other location, e.g., at the space between the laser sheet and the camera. Thermal blooming describes the condition in which the laser beam diverges due to fluid density variation because of heating of the dyed medium by the laser. Variation in fluid temperature and/or density would also cause buoyancy and inertial effects.

A series of tests were conducted by Lavertu (2006) and Perez-Alvarado (2016) on a similar experimental apparatus (the latter having the same PLIF setup) to evaluate and minimize the above errors using technical and theoretical measures. According to Perez-Alvarado (2016), the maximum attenuation of the laser beam for a 10 cm spanwise shift of the dyed fluid (for concentrations within the calibrated range) toward the beam source was less than one percent. Estimating the attenuation across the jet profile results in an error of less than 1% (this is due to the very low concentrations of dye used in experiments). Photobleaching and thermal blooming were reduced to negligible values by using a high revolution rate rotating mirror, at which the residence time of a single beam in the volume covered by each camera pixel was approximately 2 μs, while 200 μs was required for the fluorescence signal to reduce by 2% due to constant irradiation of the dyed fluid (Lavertu, 2006). It should be noted that Lavertu (2006) used punctual LIF, which is subject to a much higher possibility of constant irradiation of the dyed fluid compared to the present PLIF measurements. Trapping of the laser light was shown to be less than one percent for the calibrated range of concentration values (Perez-Alvarado, 2016). Furthermore, the inertial effects were negligible during the experiments because of the use of very low concentrations of disodium fluorescein (maximum $7.66 \times 10^{-7}\ \mathrm{mol\,L^{-1}}$) having a molecular mass of 376.3 $\mathrm{g\,mol^{-1}}$, which introduces a density variation of less than 2.8×10^{-5} % between the jet fluid and the ambient water. Therefore, common errors in the PLIF measurements are minimal in the present study.

4.3 Data processing

The passive scalar field of the two jets with Re = 10600 and 5800 issuing into the turbulent ambient is compared to those in a quiescent ambient. The PLIF images were obtained at axial distances of x/d = 20, 30, 40, 50, and 60. In order to achieve first- and second order scalar concentration convergence at these axial positions in the quiescent ambient case, data sets over a period of 27, 45, 63, 81, and 100 s resulting in a total of 789, 1315, 1841, 2367, and 2893 PLIF images, respectively, were obtained, while in the HIT ambient case, five sets of PLIF experiments, each obtained for 170 s containing 4997 images, were taken for each axial position. Custom MATLAB codes were employed to obtain scalar concentration statistics of the jet cross section in the turbulent and the quiescent ambient cases.

Instantaneous images of the jet cross section show greater irregularity when the jet is released into a turbulent ambient. The jet is also displaced laterally by the large eddies of the ambient turbulence (see Fig. 4.1*c*). The isocontours of the joint probability density function (JPDF) of the position of the jet centroid for the jet in the HIT ambient for Re = 10600 and 5800 jets are presented in Fig. 4.3. The mean radius of the jet in the quiescent ambient is approximately $r/x = \sqrt{y^2+z^2}/x = 0.2$ centered at zero (See Appendix A). The jet centroid in the HIT ambient is displaced over an area greater than that occupied by the jet in the quiescent ambient.

The standard deviation of the position of the jet centroid in the quiescent and HIT ambient is depicted against the axial position in Fig. 4.4. In the quiescent ambient, the standard deviations range between $0.004 < \sigma/x < 0.010$ and $0.005 < \sigma/x < 0.011$ for the Re = 10600 and Re = 5800 jets, respectively, while in the turbulent ambient, the standard deviations increase to $0.11 < \sigma/x < 0.15$ and $0.17 < \sigma/x < 0.22$ for the Re = 10600 and Re = 5800 jets, respectively. Therefore, in the quiescent ambient, the jet is almost always centered on the jet axis, while in the turbulent ambient, the position of the jet centroid varies significantly, which is more noticeable in the low-Re jet (higher ξ). Large standard

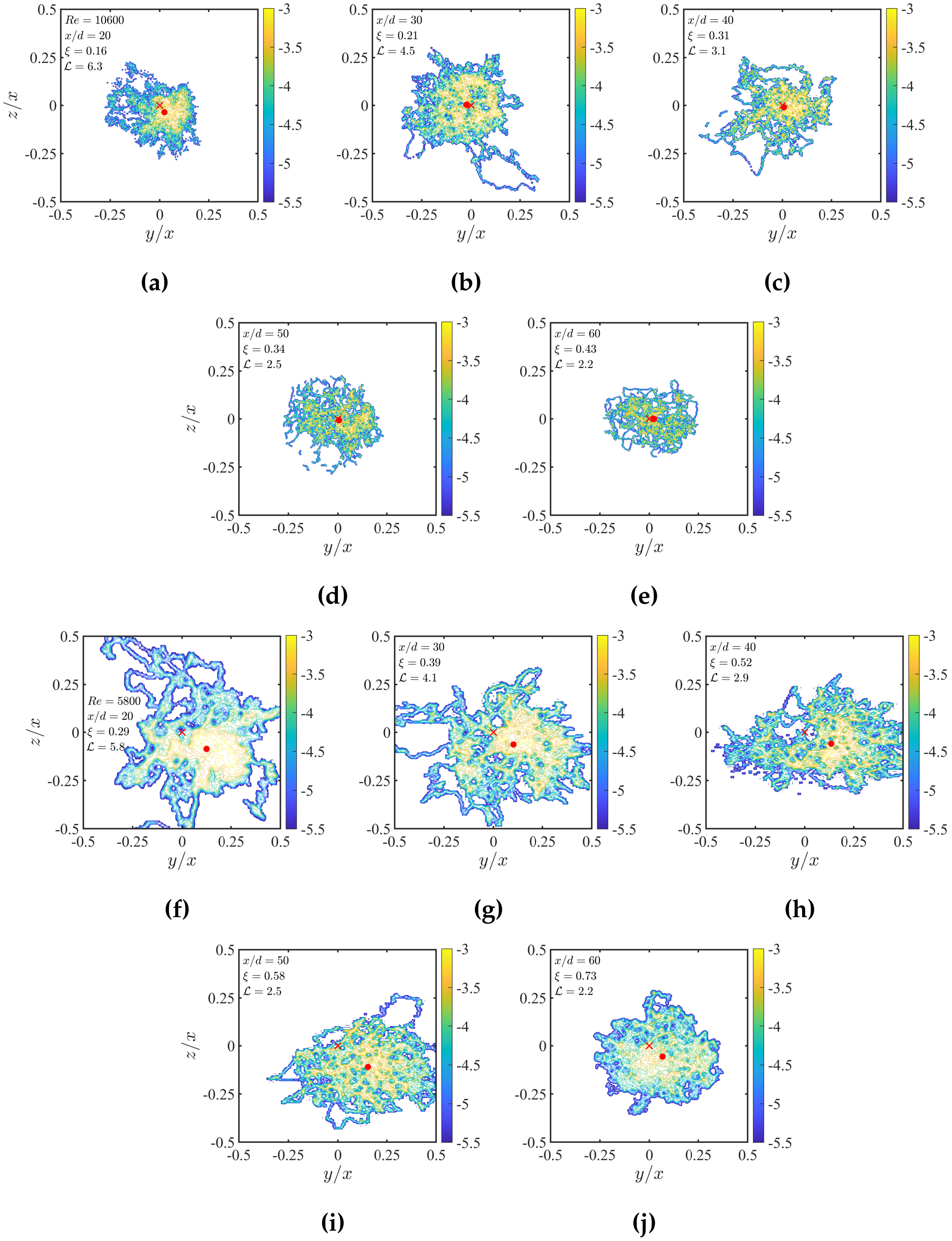

(a) **(b)** **(c)**

(d) **(e)**

(f) **(g)** **(h)**

(i) **(j)**

Figure 4.3: Isocontour of the JPDF of the jet centroid position in the HIT ambient. The red cross shows the jet axis, while the red circle denotes the mean position of the jet centroid in the turbulent ambient. For Re = 10600 jet at (*a*) x/d = 20, (*b*) 30, (*c*) 40, (*d*) 50, and (*e*) 60. Similarly, for Re = 5800 jet at (*f*) to (*j*) for x/d = 20 to 60. Note that the RJA acts on the right side of the images. The colorbars are logarithmic.

deviations of the position of the jet centroid indicate a meandering path of the jet in the turbulent ambient (schematic view in Fig. 4.5), while the jet path in the quiescent ambient is almost a straight line. The meandering path of the jet is due to lateral advection of the jet by the large ambient eddies, and is more noticeable closer to the jet exit, where $\mathcal{L} \gg 1$. As the jet grows in the downstream direction, the relative length scale between the ambient and the jet decreases, and hence the large eddies of the HIT ambient are less able to advect the jet. This is evident in the generally decreasing standard deviation of the jet centroid position with the axial distance in Fig. 4.4. Particularly, beyond x/d = 40 for both jets where $\mathcal{L} \approx$ 3.0, the role of the large-scale ambient eddies on the jet motion is less dominant. However, at x/d = 20 of Re = 10600 jet, the standard deviation has a local minimum due to the strong structure of the jet that resists the external forcing advecting the jet path. Similar meandering due to turbulence in the ambient was observed in wakes (Kankanwadi and Buxton, 2020). It should be noted that in the present study, the only apparent role of the relative length scale ($\mathcal{L}$) on the jet behavior in the HIT ambient is to cause the jet path to meander, which is effectively removed in the centroidal analysis of the data. Therefore, in the following sections only the effect of the turbulence intensity ratio on the jet behavior in HIT ambient is discussed.

The time-averaged characteristics of the jet are obtained from Eulerian averages and centroidal averages of the instantaneous images. The Eulerian average provides the ensemble-averaged concentration at a particular location (geometric position) relative to the jet axis, which includes the composite effects of the large and small scales of the ambient turbulence on the jet at a particular location in space. The second approach, by being conditioned on the centroid of the jet cross section, excludes the effect of the larger scales translating the jet laterally, and includes primarily the influence of the smaller scales of the ambient turbulence, which modify the internal jet structure and dynamics (Hunt, 1994; Gaskin et al., 2017). However, it should be noted that at high levels of turbulence intensity, the effect of large-scale eddies is not fully removed due to the meandering of the jet resulting in a discontinuity in the jet structure. The analyses are carried out on

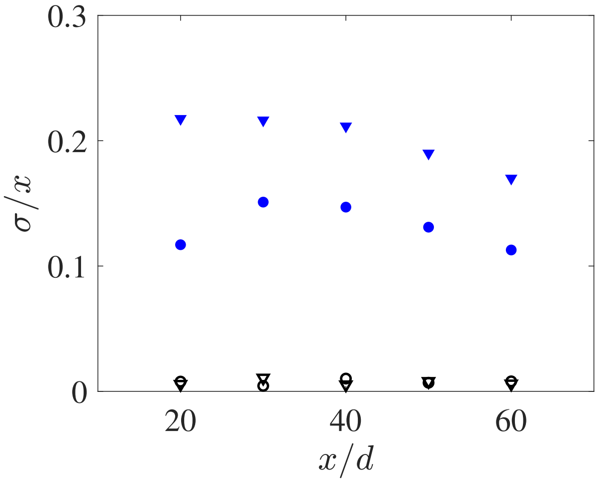

Figure 4.4: Standard deviation of the jet centroid with the axial distance in the quiescent and in the turbulent ambient. Symbols: ○ Re = 10600 quiescent; ● Re = 10600 HIT; ▽ Re = 5800 quiescent; ▼ Re = 5800 HIT.

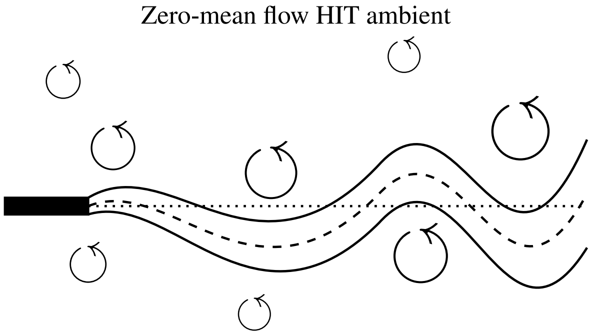

Figure 4.5: Schematic of the jet structure in the ambient turbulence, showing the jet axis (dotted line), and the jet centroid (dashed line). Large scale eddies of the HIT ambient cause the jet to meander.

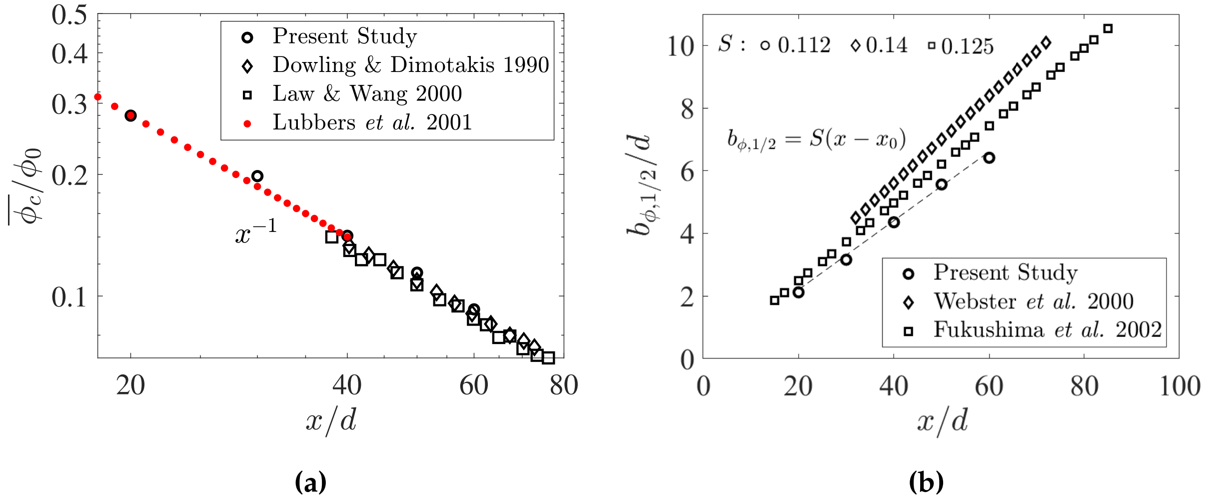

Figure 4.6: Downstream evolution of the (*a*) mean centerline concentration, and (*b*) concentration half-width of an axisymmetric jet at $Re = 5800$ issued into a quiescent ambient.

a profile equidistant from the RJA plane, passing through the centerline or the centroid, which is subjected to an approximately constant level of ambient turbulence at any given downstream position. A similar approach was previously adopted in axisymmetric (Burridge et al., 2017) and line (Parker et al., 2019) plumes in order to eliminate the effect of large-scale meandering by considering the flow characteristics in the plume coordinates, i.e., following the instantaneous turbulent/non-turbulent interface (TNTI) of the plume. It is worth noting that the centroidal origin ($r = 0$) in the current study is positioned on the mass center of the bulk of the flow within the FOV, whereas the origin of the plume coordinates in the aforementioned studies is the middle point of the left and right TNTI at each downstream distance. We note that although the FOV is fairly large, the calculation of the centroid position is affected to a small extent by the amount of dye going out of the FOV due to meandering of the jet path. A sensitivity analysis is carried out in Appendix 4.7 to quantify the dependence of the mean centroid location on scalar concentrations above a range of thresholds.

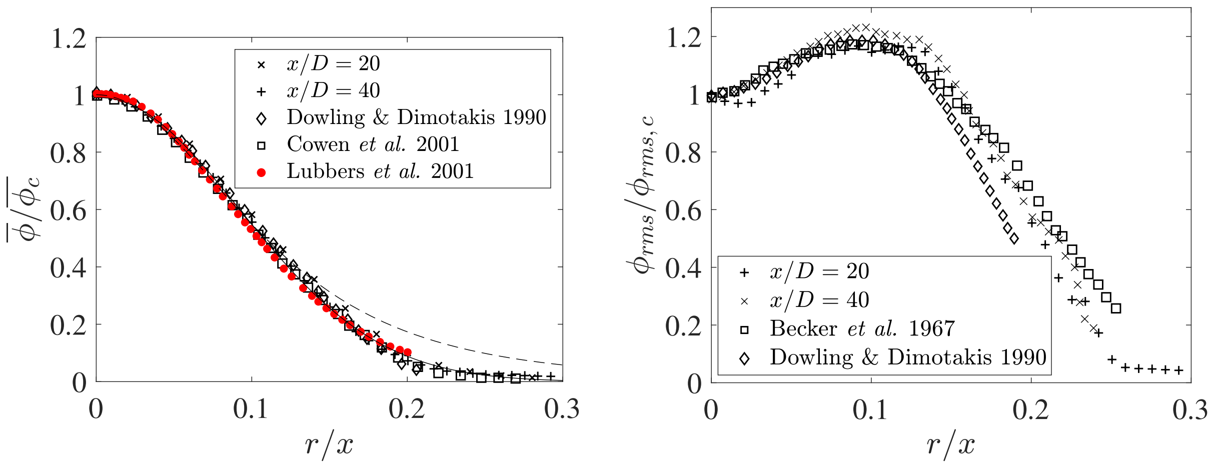

(a) **(b)**

Figure 4.7: Radial profiles of (*a*) mean concentration, and (*b*) rms concentration fluctuations of an axisymmetric jet at Re = 5800 issuing into a quiescent ambient. The solid line and the dashed line in (*a*) show the Gaussian fit and the analytical solution of the round jet, respectively.

4.4 Measurement validation

Measurements of the scalar field of the jet in a quiescent ambient show a self-similar behavior in the mean and rms concentration profiles (Fischer et al., 1979), similar to those in the velocity field (e.g. see Hussein et al. (1994)). The scalar concentration measurements of the jet issued into a quiescent ambient of the current work are validated by a comparison to those reported in the literature using different experimental methods: Mie scattering (Becker et al., 1967), Rayleigh scattering (Dowling and Dimotakis, 1990), PLIF (Law and Wang, 2000; Webster et al., 2001; Cowen et al., 2000; Fukushima et al., 2002), and by direct numerical simulation (DNS) of a turbulent jet (Lubbers et al., 2001).

The downstream evolution of the mean centerline concentration, $\overline{\phi_c}$, normalized by the jet exit concentration, ϕ_0, for the jet in a quiescent ambient is shown in Fig. 4.6(*a*). Along the jet centerline, $\overline{\phi_c}$ varies inversely with the downstream distance as $\overline{\phi_c} = \kappa_\phi \phi_0 (\frac{x-x_0}{d})^{-1}$, where κ is the decay constant, and the position of the virtual origin, x_0, is 2.4 d in the present work. The current work shows a power law decay of x^{-1} as predicted theoretically and previously observed (Pope, 2000; Dowling and Dimotakis, 1990; Law and Wang, 2000; Lubbers et al., 2001). The decay constant, κ, depends slightly on Reynolds number and on the initial conditions (Mi et al., 2001), and its value here ($\kappa = 5.4$) lies within the reported range of $4.48 < \kappa < 5.59$ in Dowling and Dimotakis (1990). A comprehensive review of the asymptotic behavior of κ is presented in Table 1 of Mi et al. (2001).

The downstream evolution of the concentration half-width, $b_{\phi,1/2}$, defined as the radial position at which the concentration reduces to half of its centerline value, is shown in Fig. 4.6(*b*). In a quiescent ambient in the self-similar region of the jet, $b_{\phi,1/2}$ is a linear function of the downstream distance, $b_{\phi,1/2}(x) = S(x - x_0)$, where *S* is the spreading rate of the scalar field in the jet. Experimental data show that *S* is independent of Reynolds number, and varies between $0.101 < S < 0.156$ (Fischer et al., 1979). In the present work, *S* is about 0.112.

The radial profiles of the mean concentration normalized by their respective centerline value are shown in Fig. 4.7(*a*). The analytical solution for the mean concentration profile of a round jet is given by $\overline{\phi}/\overline{\phi_c} = \{1 + a(r/x)^2\}^{-2}$, where a is a constant, $a = (\sqrt{2} - 1)/S^2$ (Pope, 2000). The analytical solution and a Gaussian fit to the experimental data are also shown in Fig. 4.7(*a*). The profiles at x/d = 20 and 40 show a good agreement with the previous experimental results (Dowling and Dimotakis, 1990; Cowen et al., 2000), a DNS study (Lubbers et al., 2001), and the Gaussian fit. The profiles at x/d = 30, 50, and 60 also show a good agreement and are not included here for brevity. It is noted that the analytical solution overestimates the concentration values near the edges of the jet (Pope, 2000) as a constant turbulent diffusivity is assumed across the flow, while it is, in fact, lower near the edges due to external intermittency.

The radial profiles of rms concentration fluctuations normalized by their respective centerline values at $x/d = 20$ and 40, are also shown in Fig. 4.7(*b*). The profiles are self-similar and behave similarly to those reported in the literature (Becker et al., 1967; Dowling and Dimotakis, 1990). The rms profiles at x/d = 30, 50, and 60 also show a good agreement.

4.5 Results and discussion

The effect of ambient turbulence on the jet characteristics is determined by the relative magnitudes of the turbulence intensity, ξ, and the integral length scales, $\mathcal{L}$, between the the HIT ambient and the jet (Hunt, 1994; Gaskin et al., 2004). While in the present study $\mathcal{L} > 1$ and $\xi < 1$ at all measurement stations (see Table 4.1), they both approach unity at the furthest downstream locations and become $\mathcal{O}(1)$. This is the condition at which the ambient turbulence affects the jet structure and changes the entrainment process and the subsequent scalar mixing. Note that it is mainly the intense smaller eddies of the ambient that alter the jet structure, while the larger eddies serve to advect the jet, resulting in a meandering path (Hunt, 1994). Also, it should be noted that once $\mathcal{L}$ and ξ become $\mathcal{O}(1)$, the effect of ξ has a dominant effect on the jet behavior, causing the jet to break up at a critical axial distance. For example, Kankanwadi and Buxton (2020) recently showed the predominance of ξ as compared to $\mathcal{L}$ in the context of entrainment into a cylinder wake in a homogeneous turbulent ambient. Therefore, the following discussion of the results covers only the effect of ξ on the jet behavior in HIT ambient (note that the role of $\mathcal{L}$ is to cause the jet path to meander, and its effect has been essentially removed in the centroidal data analysis.)

The growth, structure, and statistics of the passive scalar field of an axisymmetric turbulent jet issuing into a turbulent ambient are presented and compared to those of the jet in a quiescent ambient. The TKE of the ambient turbulence is k_{HIT} = 4.44 $\mathrm{cm}^2\mathrm{s}^{-2}$, and the jet Reynolds numbers are Re = 10600 and 5800. Five orthogonal cross sections in the self-similar zone of the jet in a quiescent ambient have been studied (x/d = [20, 30, 40, 50, 60]). Variation of ξ and $\mathcal{L}$ for each downstream location of the two jets results in ten different case studies, as depicted in Fig. 4.2. To present the results, first, the evolution and structure of the jet will be discussed in terms of the mean concentration, the concentration half-width, and the rms concentration. Then, the self-similarity of the scalar field will be studied. Finally, statistics of the scalar mixing will be presented using the intermittency

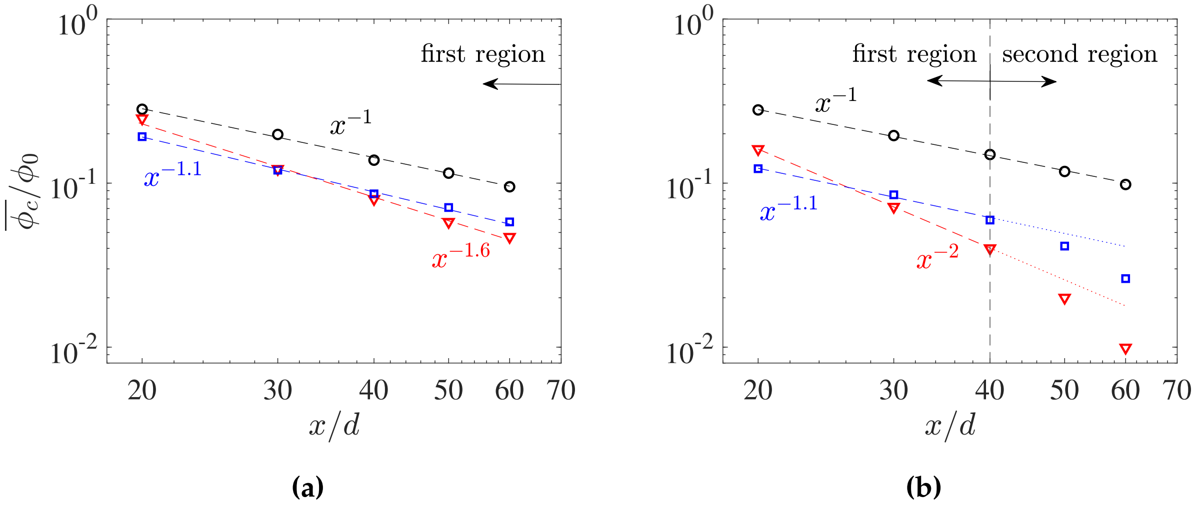

Figure 4.8: The effect of ambient turbulence on the downstream evolution of the mean centerline concentration. (*a*) $Re = 10600$, and (*b*) $Re = 5800$. Symbols: ○ quiescent ambient; □ centroidal, and ▽ Eulerian averaging in HIT ambient. Figures are in log-log coordinates.

factor, probability density functions (PDFs), and the cumulative distribution functions (CDFs) of the centerline concentration. It should be noted that the variation between the centroidal and the Eulerian analyses in the quiescent ambient was negligible for the mean profiles (less than 1%), and was less than 4% and 7% for the PDFs and the rms profiles, respectively. Therefore, in the following figures, only the centroidal analysis of the jet in a quiescent ambient is provided.

4.5.1 Evolution and structure of the jet

The turbulent jet issuing into HIT ambient is subject to an increasing impact from the intensity of the ambient turbulence (i.e. increasing ξ) and a decreasing impact from the length scale of the ambient turbulence (i.e. decreasing $\mathcal{L}$) as its own turbulence intensity decreases and length scale increases, while those of the ambient turbulence are constant with downstream distance. In ambient turbulence, jet entrainment is reduced as the jet flow is progressively disrupted. Two regions of behavior of the jet are identified, based on the jet statistics conditioned on the jet centroid, which allow the jet structure to be assessed. The regions reflect the increasing impact of the ambient turbulence intensity and are characterized by (1) a perturbed jet structure—downstream of the developing jet region—and, further downstream, (2) a destroyed jet structure. The relative lengths of these regions depend on the relative turbulence intensity between the ambient and the jet. In this study, region 1 is observed in the Re = 10600 jet, while regions 1 and 2 are observed in the Re = 5800 jet, for x/d = 20 to 60.

The downstream evolution of the mean jet centerline concentration ($\overline{\phi_c}/\phi_0$) of the jet issuing into a turbulent ambient results in lower concentrations and a faster decay as compared to the jet in a quiescent ambient. Hereafter, $\overline{\phi_c}$ denotes the mean concentration of the geometric centerline (i.e., jet axis) in the Eulerian averaging method, while it represents the ensemble average of the instantaneous centroid scalar concentration values in the centroidal averaging procedure. The concentration decay initially follows a power law for both the centroidal and Eulerian averages of the jet in a turbulent ambient, as shown in Fig. 4.8. The decay exponents are, $\overline{\phi_c}/\phi_0 \propto x^{-1.1}$ for both jets for the centroidal average and $\overline{\phi_c}/\phi_0 \propto x^{-1.6}$ and x^{-2} for Re = 10600 and 5800 jets, respectively for the Eulerian average. The uncertainty in measurements is three orders of magnitude smaller than the mean values due either to the low variance (in quiescent ambient) or the high number of samples (in HIT ambient). The power-law region is the perturbed jet region in the two-region jet model. The effect of ambient turbulence is greater at larger values of relative turbulence intensity (ξ), which is inversely proportional to Re, i.e. $\xi_{5800} > \xi_{10600}$ at each downstream distance. This is evident in the relative lengths of the power-law regions of the jets, which is up to x/d = 60 for Re = 10600 (the jet was observed to break up at x/d = 70 for the Eulerian average in Perez-Alvarado (2016)), while in the Re = 5800 jet, it is only valid up to x/d = 40, beyond which the concentration decay accelerates, and where it is later shown that the jet structure has been destroyed. Eulerian averaging shows a faster concentration decay as compared to averaging because the effect of jet meandering, causing low concentrations to appear at the geometric axis, is included in the Eulerian average.

Table 4.2: Power law exponents for the jet in quiescent and HIT ambient.

Background condition	Averaging method	Re = 10600			Re = 5800		
		$\overline{\phi_c}/\phi_0$	$b_{\phi,1/2}/d$	$\phi_{rms,\,c}/\phi_0$	$\overline{\phi_c}/\phi_0$	$b_{\phi,1/2}/d$	$\phi_{rms,\,c}/\phi_0$
Quiescent	Centroidal	x^{-1}	x^{1}	$x^{-0.7}$	x^{-1}	x^{1}	$x^{-0.7}$
Turbulent	Centroidal	$x^{-1.1}$	$x^{1.1}$	$x^{-0.94}$	$x^{-1.1}$ $(x/d \leqslant 40)$	$x^{1.1}$ $(x/d \leqslant 40)$	$x^{-0.92}$ $(x/d \leqslant 40)$
	Eulerian	$x^{-1.6}$	$x^{1.2}$	$x^{-0.73}$	x^{-2} $(x/d \leqslant 40)$	$x^{1.5}$ $(x/d \leqslant 40)$	$x^{-0.83}$ $(x/d \leqslant 40)$

The power-law region of the jet (i.e., first region) starts following the developing region of the jet. If the power-law behavior of the jet is extrapolated backward, it predicts that $\overline{\phi}_c/\phi_0$ = 1 at $x/d \approx$ 7 and 6 for the centroidal analysis of the Re = 10600 jet in a quiescent and HIT ambient, respectively. Similarly, $x/d \approx$ 7 and 2 is predicted for the Re = 5800 jet. This suggests that the length of the developing region of the jet is reduced in the HIT ambient, but this requires further experiments for verification. It appears that although both jet Reynolds numbers are affected, the effect is greater for the jet with higher relative turbulence intensity (i.e. Re = 5800). Table 4.2 provides the decay exponents for the mean centerline concentration in the power-law regions of the Re = 10600 and 5800 jets (as well as those for the concentration half-width and the rms concentration, discussed below).

The mean scalar concentration profiles of the Re = 10600 and Re = 5800 jets issuing into a quiescent and into a turbulent ambient are close to Gaussian in shape, as shown in Fig. 4.9. As observed for the centerline concentrations, turbulence in the ambient results in faster concentration decay leading to lower concentrations in the profiles, except in the tails, i.e., $|r/x| >$ 0.2 (for all tails but those of $x/d >$ 40 for Re = 5800 jet). The higher concentrations in the tails are due to the greater width of the profile in the HIT ambient and, for the Eulerian average, the inclusion of jet meandering. In the HIT ambient, the centroidal average concentration profiles for both jet Reynolds numbers are lower and slightly wider than those of the quiescent ambient for the perturbed jet region (x/d = 20 to 60 for the Re = 10600 jet and x/d = 20 to 40 for the Re = 5800 jet, for which all $\xi < 0.5$). For the Re = 5800 jet, beyond x/d = 40 (where $\xi > 0.5$), the profiles narrow,

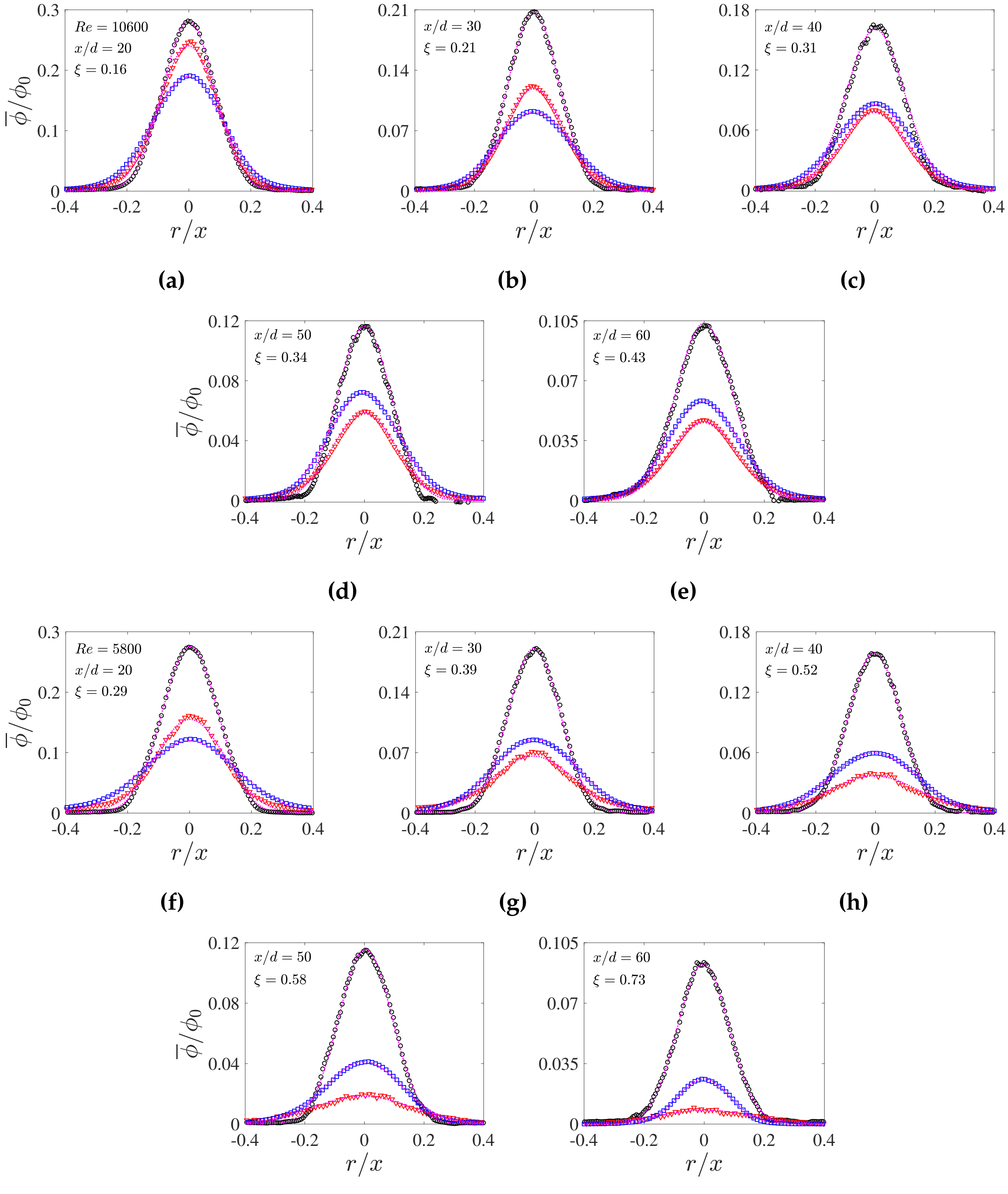

(a) **(b)** **(c)**

(d) **(e)**

(f) **(g)** **(h)**

(i) **(j)**

Figure 4.9: Radial profiles of the mean concentration. For Re = 10600 jet at (*a*) x/d = 20, (*b*) 30, (*c*) 40, (*d*) 50, and (*e*) 60. Similarly, for Re = 5800 jet at (*f*) to (*j*) for x/d = 20 to 60. Symbols: ○ quiescent ambient; □ centroidal, and ▽ Eulerian averaging in HIT ambient. Dashed magenta curves are Gaussian fit to the profiles.

indicating a greatly reduced entrainment and, therefore, a destruction of the jet structure. The Eulerian average profiles are generally lower than those of the centroidal average due to the inclusion of jet meandering. However, the maxima of the Eulerian profiles for Re = 10600 up to x/d = 30 and for Re = 5800 at x/d = 20 are higher than those of the centroidal profiles because, although the extent of the jet boundary is relatively stationary, the position of the passive scalar centroid is affected by the ambient turbulence. The Eulerian average observations of mean centerline concentration confirm those of Perez-Alvarado (2016).

The concentration half-width, $b_{\phi,1/2}$, is a characteristic length scale of the scalar field, and its downstream evolution is shown in Fig. 4.10. In the quiescent ambient, the concentration half-width grows linearly with the axial distance, x, as predicted by dimensional analysis. In the turbulent ambient, the half-width is greater than in the quiescent ambient and its rate of growth is faster ($b_{\phi,1/2} \propto x^{1.1}$) for both jet Reynolds numbers in the perturbed jet region for the centroidal average. The width growth ceases for $x/d > 40$ for the Re = 5800 jet indicating that the time-averaged entrainment into the jet has stopped (as discussed below), which implies that the jet structure has been destroyed, meeting the criteria of jet breakup. Jet breakup is, therefore, identified to occur at $x/d > 40$ for the Re = 5800 jet, and the region beyond it (where $\xi > 0.5$) is the destroyed jet region, which is only subject to turbulent and molecular diffusion (the Re = 10600 jet is destroyed at x/d = 70) (Perez-Alvarado, 2016). It is relevant to note that the scalar width of a round jet subjected to volumetric heating also ceases to grow upon disruption of the large-scale vortical structures of the jet (Bhat and Narasimha, 1996; Agrawal and Prasad, 2004). The Eulerian average data obscure the change in behavior of the Re = 5800 jet due to the inclusion of the meandering of the jet, which also results in a much higher rate of width growth ($b_{\phi,1/2} \propto x^{1.2}$ and $b_{\phi,1/2} \propto x^{1.5}$ for the Re = 10600 and Re = 5800 jets, respectively). This is consistent with the growth rates (from Eulerian average data) of the concentration half-width of jets (Perez-Alvarado, 2016), the velocity half-width of momentum-driven

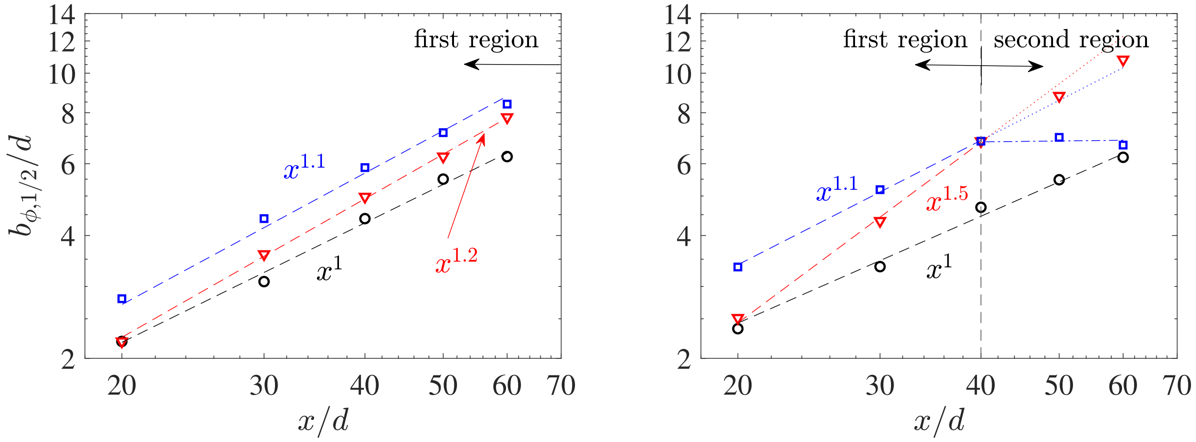

(a) **(b)**

Figure 4.10: The effect of the ambient turbulence on the downstream evolution of the concentration half-width. (*a*) *Re* = 10600, and (*b*) *Re* = 5800. Symbols: ○ quiescent ambient; □ centroidal, and ▽ Eulerian averaging in HIT ambient. Figures are in log-log coordinates. A dash-dotted line in (*b*) denotes the unchanged concentration half-width in the second region.

(Khorsandi et al., 2013) and buoyant jets (Lai et al., 2019), and of wakes (e.g. see Eames et al. (2011b) and Legendre et al. (2006)) in a HIT ambient.

The effect of the HIT ambient on the entrainment into the jet can be deduced from the integral volume flux, Q, momentum flux, M, and scalar flux, F, defined as

$$Q \equiv 2\pi \int_0^\infty \overline{U} r \, \mathrm{d}r, \quad M \equiv 2\pi \int_0^\infty \overline{U}^2 r \, \mathrm{d}r, \quad F \equiv 2\pi \int_0^\infty \overline{U\phi} r \, \mathrm{d}r, \tag{4.5}$$

where $\overline{U}$ is the mean streamwise velocity of the jet. The entrainment hypothesis (Morton et al., 1956) states that the entrainment into a jet in a quiescent ambient is a function of the entrainment velocity, E_v, which is proportional to a characteristic jet velocity, usually the mean axial velocity, i.e., $E_v \propto \overline{U}_c$. With continuous entrainment of the ambient fluid at the jet interface, the mass flow rate of the jet ($m = 2\pi\rho \int_0^\infty \overline{U} r \, \mathrm{d}r$) increases linearly with the downstream distance. In the HIT ambient, it is expected that the mass flow rate of the jet is decreased due to lower mean axial velocities compared to the quiescent ambient

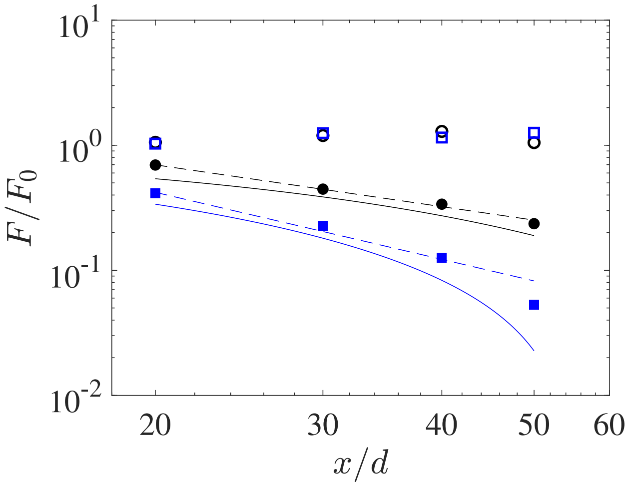

Figure 4.11: The effect of the ambient turbulence on the downstream evolution the mean scalar flux of the jet. Symbols: ○ *Re* = 10600 quiescent; ● *Re* = 10600 HIT; □ *Re* = 5800 quiescent; ■ *Re* = 5800 HIT. Dashed lines are power-law fits to the data. Solid lines show the prediction by Lai et al. (2019)'s exponential model for the scalar flux of the jet in the HIT ambient.

(Khorsandi et al., 2013). Also, one can expect that the mass flow rate of the jet does not increase beyond the jet breakup, because the mean axial velocity becomes negligible. A reduction in mass flow rate in the HIT ambient is observed for the $Re = 10600$ jet (Khorsandi et al., 2013), whose rate of increase decreases by $x/d = 70 - 80$. A second-order integral model has also been proposed, predicting a reduced volume flux ($Q = m/\rho$) in the HIT ambient that reaches a plateau at a critical downstream distance (Lai et al., 2019). A lower mass flow rate (and lower volume flux) of the jet in the HIT ambient indicates a lower entrainment into the jet compared to the quiescent ambient. The asymptotic behavior of m/m_0 and Q/Q_0 (m_0 and Q_0 denoting the jet exit mass flow rate and volume flux, respectively) indicates the cessation of entrainment into the jet beyond the jet breakup (Khorsandi et al., 2013; Lai et al., 2019).

Furthermore, the mean momentum flux and the mean scalar flux are indicators of jet entrainment. For the jet in a quiescent ambient, both M/M_0 and F/F_0 are conserved ($M/M_0 \approx 1, F/F_0 \approx 1$) and the mean momentum flux and the mean scalar flux contribute almost 90% and 92% of the jet exit momentum, M_0, and the jet exit scalar flux, F_0, respectively (Hussein et al., 1994; Wang and Law, 2002). For the jet in a turbulent ambient, however, M/M_0 and F/F_0 are less than one and increasingly so with the downstream distance (Perez-Alvarado, 2016) as the contribution of the mean fluxes decreases due to the increasing effect of the disruption of the jet structure (Fig. 4.11), while the second-order fluxes become more important (Khorsandi et al., 2013; Perez-Alvarado, 2016; Lai et al., 2019). Lai et al. (2019) argued that the conservation of the total momentum of the jet in the HIT ambient can be demonstrated only if the second-order momentum flux is included. The scalar flux is calculated using the present concentration data and the velocity data from Khorsandi et al. (2013). It is noted as only the spatially-averaged velocity data (up to $x/d = 50$) were available, the spatially averaged concentrations were used to calculate the scalar flux. The mean momentum flux (Perez-Alvarado, 2016) and the mean scalar flux (Fig. 4.11) are lower for the $Re = 5800$ jet and decrease faster compared to the $Re = 10600$ jet in the HIT ambient. This reflects the larger ratio of the turbulence intensity of the HIT to the jet, ξ, for the $Re = 5800$ jet at any given downstream position. Both M/M_0 and F/F_0 are approaching zero by $\xi = 0.58$ (i.e. $x/d = 50$ for the $Re = 5800$ jet), which is found within the destroyed jet region. Lai et al. (2019)'s exponential model has also been used to reproduce the scalar flux of the current jet in the HIT ambient in Fig. 4.11, which shows good agreement with the experimental data.

In the second region of the jet in the HIT ambient ($\xi > 0.5$) the centroidal scalar half-width stops growing (Fig. 4.10*b*, $x/d > 40$ for the $Re = 5800$ jet), which indicates the cessation of entrainment into the jet. To further investigate the entrainment in the second region, we have defined the top-hat width, b_m, and velocity, u_m, of the jet as follows:

$$b_m \equiv \frac{Q}{\sqrt{M}}, \qquad u_m \equiv \frac{M}{Q}. \tag{4.6}$$

The rate of change of the volume flux in the streamwise direction is evaluated as,

$$\frac{\mathrm{d}Q}{\mathrm{d}x} = \underbrace{b_m^2 \frac{\partial u_m}{\partial x}}_{Q^- < 0} + \underbrace{2 b_m u_m \frac{\partial b_m}{\partial x}}_{Q^+ > 0} . \tag{4.7}$$

For a jet in quiescent background, $Q^+ = 2|Q^-|$ due to the conservation of momentum, meaning that the jet is entraining the ambient fluid on average. In a HIT ambient, however, the lack of growth of the centroidal scalar half-width in the second region (Fig. 4.10*b*, $Re = 5800$ jet) implies that the rate of increase in the integral jet width with downstream distance is zero. This leads to the second term of the right-hand side of Eq. 4.7 to be zero, and, thus,

$$\frac{\mathrm{d}Q}{\mathrm{d}x} \approx b_m^2 \frac{\partial u_m}{\partial x} \leqslant 0, \tag{4.8}$$

since the characteristic velocity is decaying Khorsandi et al. (2013). Therefore, the change in the integral volume flux with distance, which is interpreted as the time-averaged entrainment rate, has ceased in the second region. A similar claim can be made for the integral momentum flux in this region, that is,

$$\frac{\mathrm{d}M}{\mathrm{d}x} \approx 2 u_m b_m^2 \frac{\partial u_m}{\partial x} \leqslant 0, \tag{4.9}$$

meaning that the mean momentum flux, M, has no means of increasing. According to Morton, Taylor, and Turner, Morton et al. (1956) the lack of global entrainment in the second region implies the absence of a mean velocity to drive the entrainment process, and this in turn demonstrates that a jet no longer exists beyond $\xi > 0.5$.

Higher rms concentration values, ϕ_{rms}, occur in the jet in the turbulent ambient as compared to the quiescent ambient, as shown in Fig. 4.12. Previously, Pal and Sarkar (2015) also reported an increased turbulence level (or equivalently an increased turbulent kinetic energy) in towed wakes subjected to isotropic turbulence, due to entrainment of background fluctuations. The rate of decay of the rms centerline concentration in the turbulent ambient of the centroidal average data is more rapid (at a rate of $\phi_{rms,c} \propto x^{-0.94}$ and

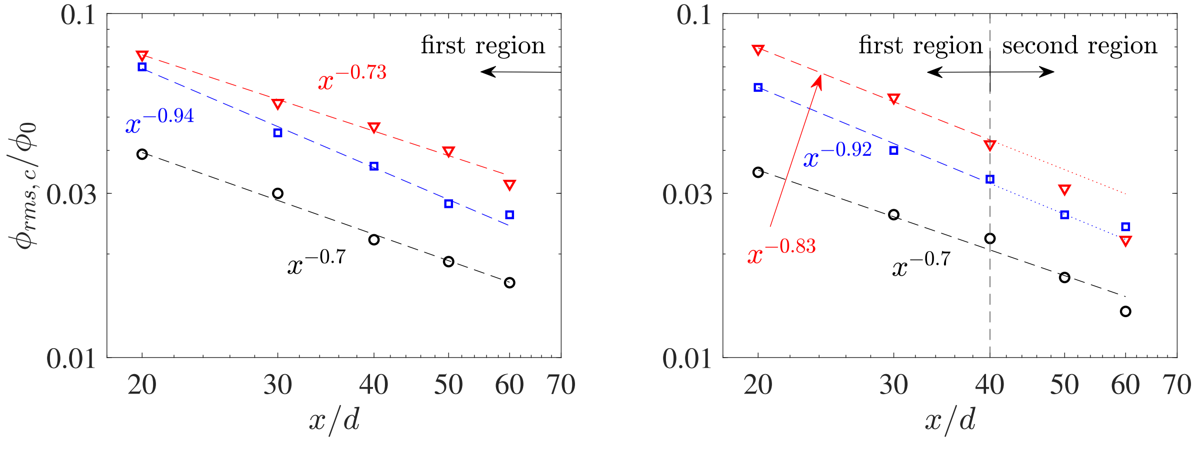

(a) **(b)**

Figure 4.12: The effect of ambient turbulence on the downstream evolution of the centerline rms concentration. (*a*) $Re = 10600$, and (*b*) $Re = 5800$. Symbols: ○ quiescent ambient; □ centroidal, and ▽ Eulerian averaging in HIT ambient. Figures are in log-log coordinates.

$x^{-0.92}$ for the $Re = 10600$ and 5800 jets, respectively) than that in the quiescent ambient (at a rate of $\phi_{rms,c} \propto x^{-0.7}$). Due to the inclusion of jet meandering in addition to the changes in rms concentration in the jet, the rms of the Eulerian average data is higher than that of the centroidal average data and has a slower rate of decay (at $\phi_{rms,c} \propto x^{-0.73}$ and $x^{-0.83}$ for the $Re = 10600$ and 5800 jets, respectively). Note that once the jet is destroyed (beyond $x/d = 40$ in the $Re = 5800$ jet), the rate of decay of the Eulerian average is more rapid than in the power-law region (perturbed jet region), as there is no longer a contribution to the scalar fluctuations from the jet structure, but only from the advection of the scalar by the HIT ambient.

The rms concentration profiles are shown in Fig. 4.13. The double peaked shape of the rms profiles in the quiescent ambient show the location of the shear layer between the jet flow and the ambient. The shear layer in the jet is preserved but weakening in the turbulent ambient for the $Re = 10600$ jet as shown by the double peaked centroidal average profiles with maximum ϕ_{rms} at $r/x \approx \pm 0.1$, similar to the jet in a quiescent ambient. By $x/d = 60$, the maximum rms concentration is observed at the centerline, implying a change in the small-scale structure of the jet, while the first-order statistic of mean concentration is still in the power-law region. For the Re = 5800 jet, on which the ambient turbulence has a greater impact, i.e. $\xi_{5800} > \xi_{10600}$, the shape of the profiles at $x/d = 20$ is two-stepped, with the first step at $r/x \approx \pm$ 0.2 corresponding to the center of the shear layer between the jet and the ambient, while the second step at $r/x \approx \pm$ 0.4 may be an indication of the effect of the ambient eddies modulating the jet/ambient interface. By $x/d = 30$, the first step is still visible and demonstrates the relatively strong jet structure despite the impact of the ambient turbulence. The width of the profile starts to decrease from $x/d = 40$, reducing to that of the quiescent case by $x/d = 60$, again indicating a decaying jet structure. Eulerian averaging obscures the detail of the jet structure and the rms concentration profiles are single peaked for both jet Reynolds numbers (beyond $x/d = 30$ for the Re = 10600 jet) and become super-Gaussian with the downstream distance, the effect being stronger in the Re = 5800 jet, confirming the results of Perez-Alvarado (2016).

To summarize, two regions of jet behavior are identified in the jet in a HIT ambient. In the first region, the perturbed jet region (which is the main focus of this study), the ambient turbulence disrupts the jet structure due to meandering of the jet and entrainment of the turbulent ambient fluid resulting in a faster decay of the jet and a lower entrainment rate than in the quiescent ambient. This region follows the developing region of the jet, and the first- and second-order properties of the scalar field show a power-law behavior. In the second region, the destroyed jet region, the ambient turbulence is comparable to the jet turbulence ($\xi > 0.5$), and the jet has been broken up and destroyed. Beyond the breakup position, the jet momentum-driven mechanism of scalar transport is replaced by molecular and turbulent diffusion by the ambient eddies. The transition between the two regions is determined by the relative turbulence intensity, ξ, and the second (destroyed) region occurs for $\xi > 0.5$.

The observations of the evolution and structure of the jet in the turbulent ambient, conditioning the average data on the jet centroid, show that the ambient turbulence serves to reduce the mean concentration, while increasing the rms concentration, and to increase the concentration half-width up to the point where the jet structure breaks up. The mean

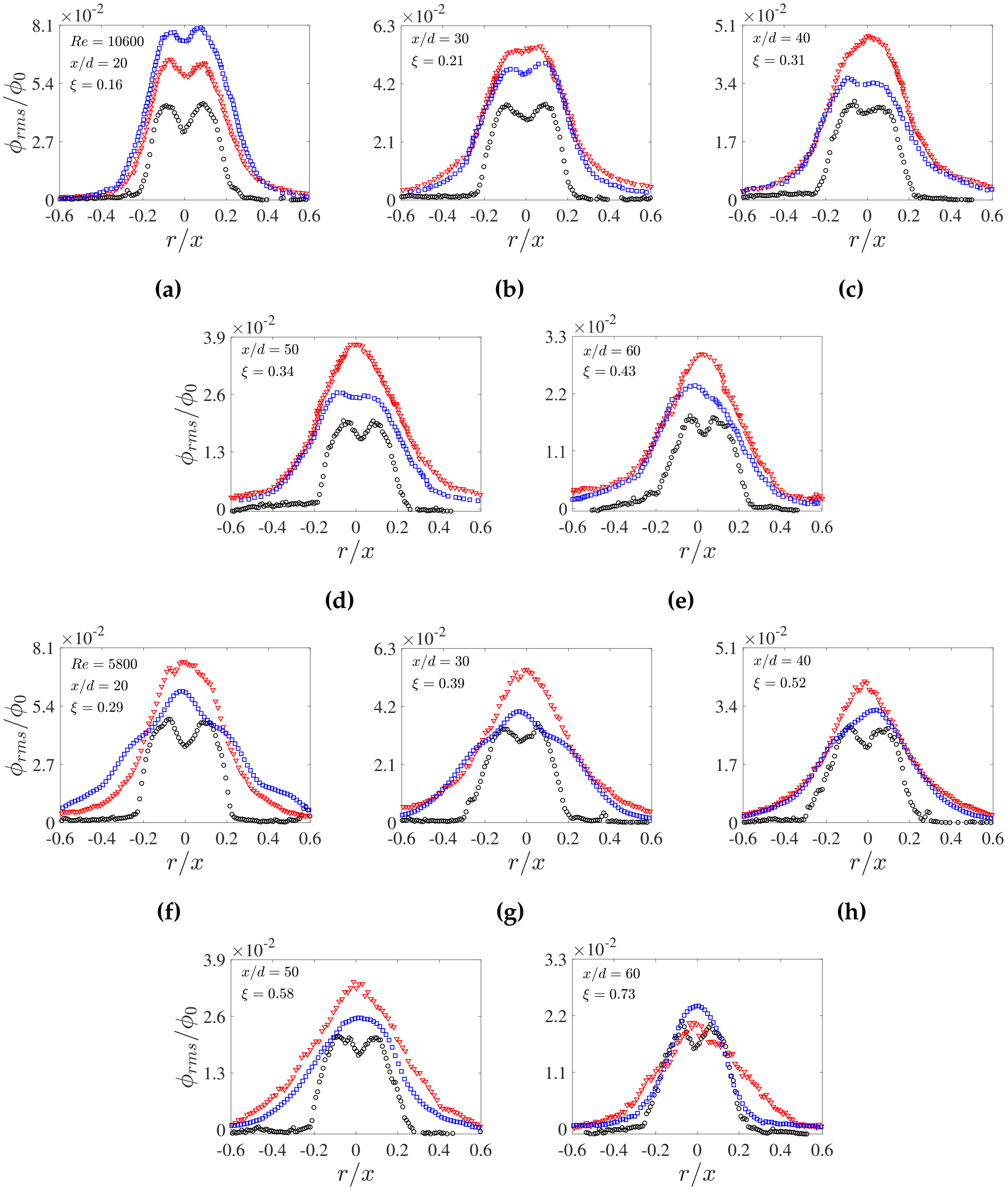

(a) **(b)** **(c)**

(d) **(e)**

(f) **(g)** **(h)**

(i) **(j)**

Figure 4.13: Radial profiles of the rms concentration fluctuations. For Re = 10600 jet at (*a*) x/d = 20, (*b*) 30, (*c*) 40, (*d*) 50, and (*e*) 60. Similarly, for Re = 5800 jet at (*f*) to (*j*) for x/d = 20 to 60. Symbols: ○ quiescent ambient; □ centroidal, and ▽ Eulerian averaging in HIT ambient.

concentration profiles maintain their Gaussian shape for both jet Reynolds numbers (up to the limit of observations), despite the external forcing. The shear layer between the jet and the ambient is found to be well preserved in the perturbed jet region before breakup. The rate of decay of the mean concentration and the growth rate of the concentration half-width are the same for both jet Reynolds numbers in the perturbed jet region. Beyond jet breakup, identified as where the relative turbulence intensity, $\xi > 0.5$, the mean concentration decays more rapidly and the half-width stops increasing. The lack of growth of the concentration half-width indicates that the jet-driven entrainment is no longer occurring, implying that the jet has been destroyed, and only molecular and turbulent diffusion is occurring (Gaskin et al., 2004). We hypothesize that when accounting for the large-scale meandering (i.e., using centroidal averaging), the evolution of the scalar field in axisymmetric jets is universal in the HIT ambient, provided the jet structure is not destroyed. Additional data over a broader range of Reynolds numbers and downstream distances (i.e. a wider range of ξ and $\mathcal{L}$) would allow us to confirm this conjecture.

4.5.2 Self-similarity and self-preservation

Self-preservation of the velocity field of an axisymmetric jet in a quiescent ambient requires that the product of the normalized mean centerline velocity, $\overline{U}_c/U_0$, and the normalized velocity half-width, $b_{u,1/2}/d$, scales to a constant (e.g. see Hussein et al. (1994)). The (first-order) self-preservation also holds for the normalized scalar concentration, $\overline{\phi_c}/\phi_0$ and the concentration half-width, $b_{\phi,1/2}/d$, in a quiescent ambient, that is, $\overline{\phi_c}/\phi_0 \times b_{\phi,1/2}/d \propto x^0$. The jet issuing into a turbulent ambient is self-preserving in the power-law region where the jet is perturbed by the ambient turbulence ($\xi < 0.5$ and before jet break-up, $\mathcal{L} =$ 2.2 - 6.3 for Re = 10600 and $\mathcal{L} =$ 2.9 - 5.8 for Re = 5800), as $\overline{\phi_c}/\phi_0 \propto x^{-1.1}$ and $b_{\phi,1/2}/d \propto x^{1.1}$ for both jet Reynolds numbers (so that $\overline{\phi_c}/\phi_0 \times b_{\phi,1/2}/d \propto x^0$), when the average is conditional on the jet centroid (see Table 4.2). Therefore, in this region, the jet maintains its evolution almost akin to the jet in a quiescent ambient, although with lower concentrations and a slightly greater spreading rate, i.e., $S =$ 0.14 and $S =$ 0.16 in the HIT ambient

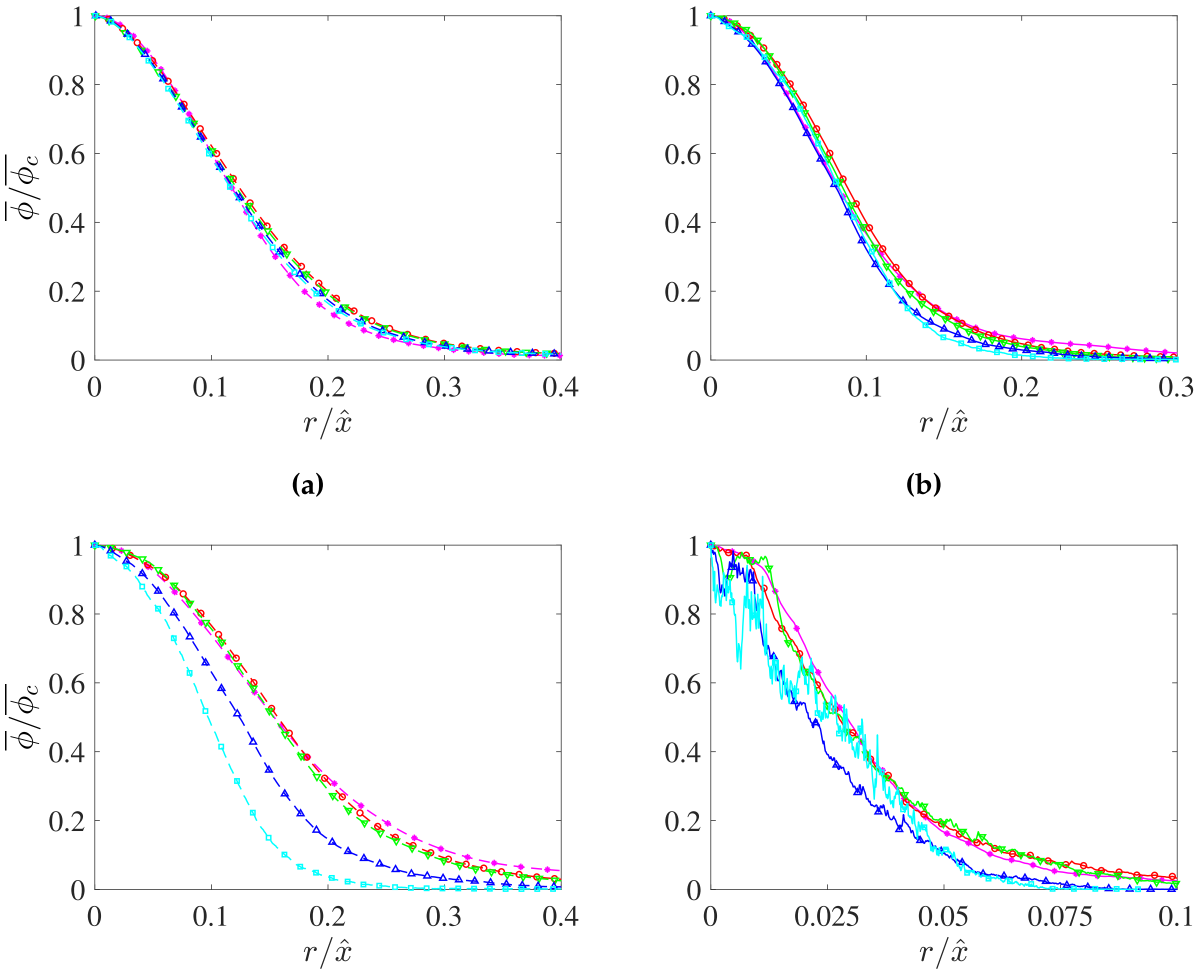

(a) (b) (c) (d)

Figure 4.14: Mean concentration profiles normalized by their centerline value. Radial distance is normalized by corresponding characteristic axial length scale, $\hat{x} = (x - x_0)^n/d^{n-1}$, where n is the growth exponent of the concentration half-width in the turbulent ambient. (a) Re = 10600 centroidal (n = 1.1), (b) Re = 10600 Eulerian (n = 1.2), (c) Re = 5800 centroidal (n = 1.1), and (d) Re = 5800 Eulerian (n = 1.5). Symbols: $*$, x/d = 20; ○, x/d = 30; ▽, x/d = 40; △, x/d = 50; □, x/d = 60.

for Re = 10600 and Re = 5800 jets, respectively, as compared to that in a quiescent ambient, $S = 0.112$.

Support for the self-similarity of the mean scalar field of the jet in a turbulent ambient, in the first or perturbed jet region, is provided by the collapse onto a single curve of the mean concentration profiles (centroidal and Eulerian averages) seen in Fig. 4.14 (for all x/ds for the Re = 10600 jet and up to jet breakup at x/d = 40 for the Re = 5800 jet), when the concentration is normalized by the mean centerline concentration, $\overline{\phi_c}$ and the radial distance by the characteristic axial length scale (LaRue and Libby, 1974), $\hat{x} = (x - x_0)^n/d^{n-1}$, where n is the growth exponent of the concentration half-width in the turbulent ambient, see Table 4.2. However, the mean scalar concentration is not self-similar in the second or destroyed jet region as seen in the centroidally averaged data [see Fig.4.13(c)]. Only the region $r/\hat{x} \geqslant 0$ is shown due to symmetry. In a similar HIT ambient generated by the RJA ($k_{HIT} = 4.4\,\mathrm{cm}^2\mathrm{s}^{-2}$), the Eulerian velocity profiles of Khorsandi et al. (2013) were reported to reveal no self-similarity of the jet flow, unlike the Eulerian concentration profiles of this study. A recent study of round jets in a turbulent coflow with very weak external turbulence (relative turbulence intensities of ξ = 0.03 to 0.23 for x/d = 45 to 105 for the case of low $k_{HIT} = 0.04\ \mathrm{cm}^2\mathrm{s}^{-2}$ and high $k_{HIT} = 0.12\ \mathrm{cm}^2\mathrm{s}^{-2}$), reported self-similarity in the Eulerian averaged profiles when $\mathcal{L} \approx 1$ (Moeini et al., 2020). The rms concentration profiles of both Reynolds number jets in HIT ambient of the current study were not self-similar, reflecting the greater vulnerability of higher statistics of the velocity and scalar fields to external forcing.

4.5.3 Statistics of the passive scalar mixing

The statistics of the passive scalar mixing are investigated in terms of the intermittency, and the PDFs (and CDFs) of the scalar concentration at the jet centerline. The intermittency of a jet describes the probability of the jet being present at a given location (allowing the structure of the jet to be deduced), and is defined as $\gamma = prob(\phi(r,x) > \phi_t)$, where ϕ_t is the scalar threshold used to define the jet/ambient interface, that is, the turbulent/non-

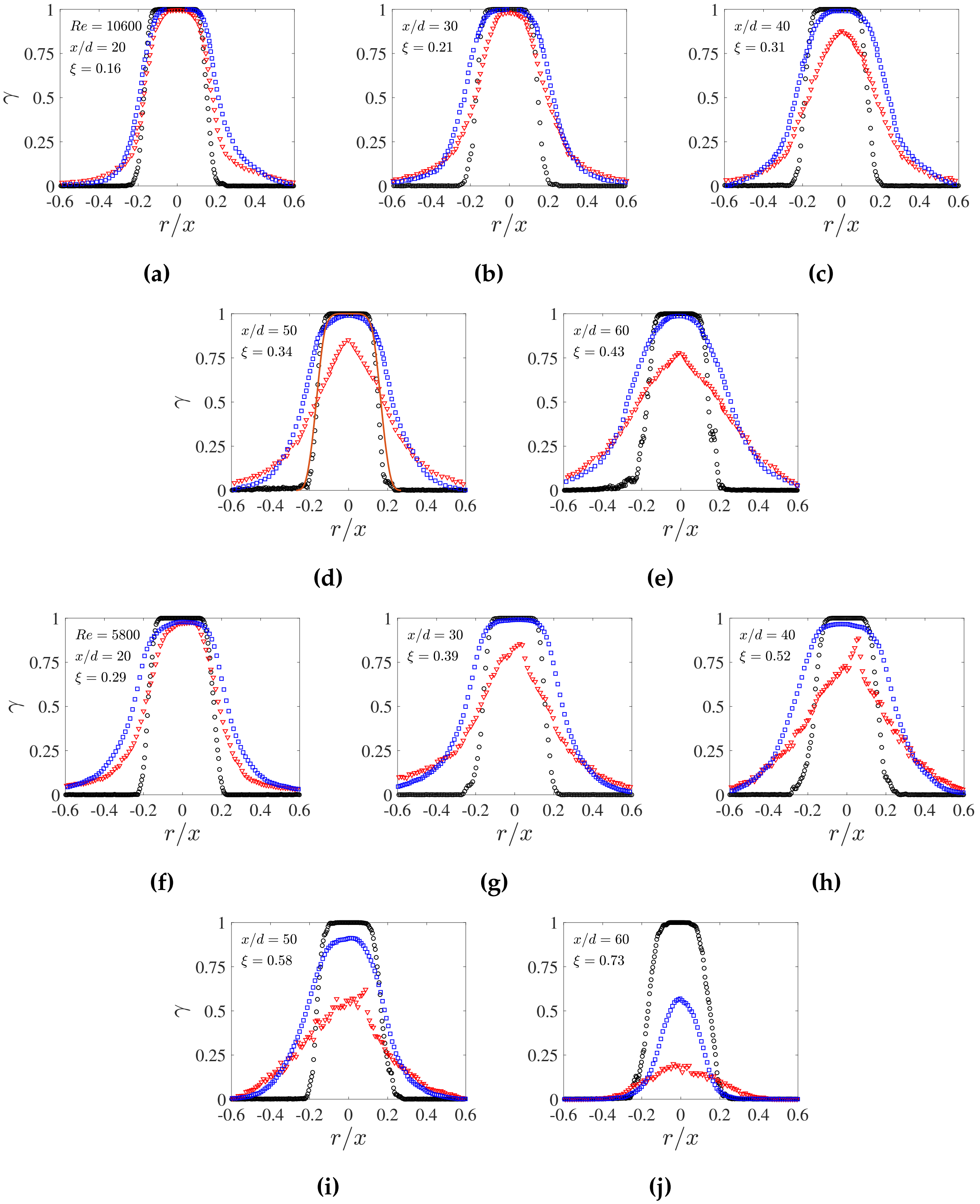

(a) **(b)** **(c)**

(d) **(e)**

(f) **(g)** **(h)**

(i) **(j)**

Figure 4.15: Radial profiles of the intermittency. For Re = 10600 jet at (*a*) x/d = 20, (*b*) 30, (*c*) 40, (*d*) 50, and (*e*) 60. Similarly, for Re = 5800 jet at (*f*) to (*j*) for x/d = 20 to 60. Symbols: ○ quiescent ambient; □ centroidal, and ▽ Eulerian averaging in HIT ambient. The solid orange line in (*d*) shows the intermittency profile in Kohan and Gaskin (2020) calculated using the cumulative distribution of the TNTI radial position.

turbulent interface (TNTI) in the quiescent ambient and the turbulent/turbulent interface (TTI) in the turbulent ambient. The interface between the inner turbulent flow and the outer ambient is usually detected by applying a suitable threshold to a flow variable, e.g., enstrophy (Bisset et al., 2002; Wolf et al., 2012), spanwise vorticity (Balamurugan et al., 2020), streamwise velocity (Khashehchi et al., 2013; van Reeuwijk et al., 2020), TKE (Chauhan et al., 2014; Kim et al., 2020), standard deviation of the velocity (Reuther and Kahler, 2018) and velocity fluctuation (Long et al., 2021), and scalar concentration (Westerweel et al., 2009; Kohan and Gaskin, 2020). Recently, several machine learning tools have also been utilized to detect the TNTI and the TTI (Wu et al., 2019; Li et al., 2020; Younes et al., 2021). In high Schmidt number flows, momentum diffusivity, ν, is much greater than scalar diffusivity, $\mathcal{D}$, resulting in a sharp interface with a distinct concentration jump, also in a turbulent ambient (e.g., see Kankanwadi and Buxton (2020) for axisymmetric wakes in a homogeneous turbulent ambient). Furthermore, the interface detected using moderate and high Schmidt number passive scalars coincides with that of the enstrophy and spanwise vorticity and, thus, reliably demarcates the turbulent flow and the ambient (Watanabe et al., 2018). The threshold value of $\phi_t = 0.15\overline{\phi_c}$ was selected empirically from the range of 0.13 $\overline{\phi_c}$ to 0.17 $\overline{\phi_c}$, for which the TNTI and TTI have only small variations (see Appendix 4.8). In a similar experimental flow, $\phi_t = 0.13\overline{\phi_c}$ was the threshold selected for the TNTI outline detection using a conditional pixel-averaged concentration method (Kohan and Gaskin, 2020).

In a quiescent ambient, the intermittency profile of the jet indicates a coherent core ($\gamma = 1$) with a width of $|r/x| <$ 0.1 and a sharply defined TNTI, whose position varies over $|r/x| =$ [0.1 - 0.2], as shown in Fig. 4.15 for jet Reynolds numbers of $Re =$ 10600 and 5800. The quiescent profile at $x/d =$ 50 for $Re =$ 10600 jet is in good agreement with a profile calculated using the cumulative distribution of the TNTI radial position (Corrsin and Kistler, 1955; Kohan and Gaskin, 2020). In the turbulent ambient, before jet breakup, the extent of the jet core is very similar to that in the quiescent ambient (when the data are centroidal averages), although the edge of the core is less distinct (γ reduces gradually

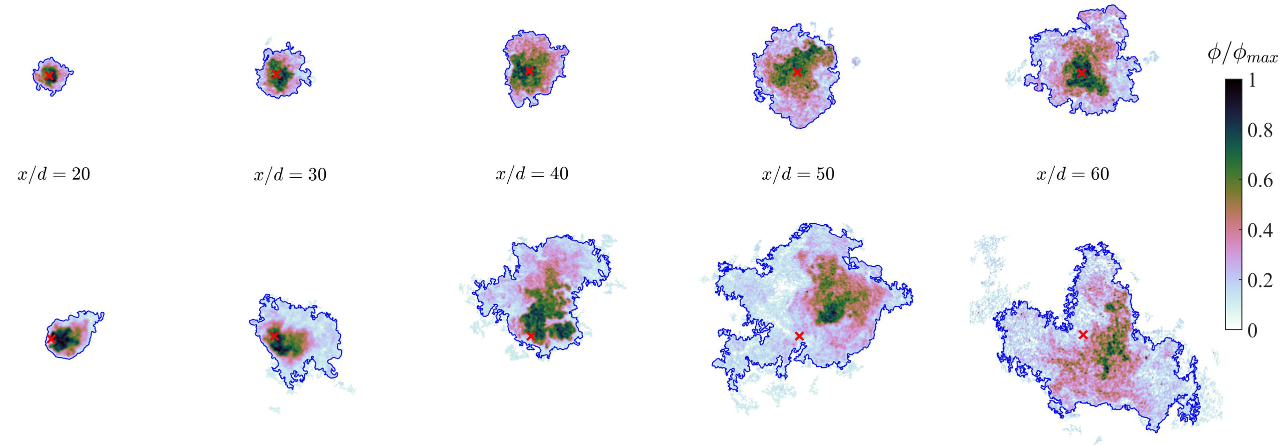

Figure 4.16: Examples of instantaneous concentration field of the jet in the quiescent (top) and the HIT (bottom) ambient for x/d = 20 - 60, Re = 5800. Each concentration field is normalized by its ϕ_{max}, as seen in the colorbar. The red cross denotes the jet axis. In the turbulent ambient, the interface is longer and more tortuous due to the interaction of small-scale eddies of the ambient on the jet interface. Note the increasing presence of very low concentrations in the jet in the HIT ambient, more noticeable beyond the jet break-up at $x/d > 40$. At x/d = 60 the core has decayed significantly.

to 0.9 over $|r/x| \approx$ [0.08 - 0.13]). After jet breakup ($x/d > 40$ for Re = 5800), the remains of the jet core region becomes less coherent, as γ decreases rapidly with downstream distance (γ_{max} = 0.9 at x/d = 50, γ_{max} = 0.6 at x/d = 60), indicating destruction of the jet structure as ambient fluid is often found in the core region. In the turbulent ambient, the jet interface (TTI) position relative to the centroid varies over a greater radial distance of $|r/x| \approx$[0.1 - 0.4] in the power-law region (i.e. the perturbed jet region before jet break-up at $x/d > 60$ for Re = 10600 and $x/d > 40$ for Re = 5800 jets). There is a low likelihood of interface excursions (increasing slightly with axial distance) between $|r/x| =$ [0.4 - 0.6] seen as the tails of the intermittency profiles. The greater range of possible radial distances of the jet/ambient interface indicates an interface that is modulated by the eddies of the ambient turbulence. The modulation results in a longer and more tortuous interface than in the quiescent ambient as seen in the flow visualization (Figs. 4.1 and 4.16). This increases the surface area of the interface over which nibbling can occur; however, as entrainment decreases in the turbulent ambient, we can reason that the local entrainment velocity is greatly reduced. Local entrainment velocity is the normal component of the relative velocity between the boundary propagation rate (E_b) and the local fluid velocity at the interface, and is often used to quantify the strength of the nibbling mechanism (Holzner and Lüthi, 2011; Mistry et al., 2016; Jahanbakhshi, 2021). As jet breakup approaches, the radial position over which the interface is located increases slightly, before decreasing rapidly after jet breakup (at x/d = 40 for Re = 5800 the radial position of the interface has narrowed to $|r/x| =$ [0 - 0.2]). The intermittency profiles obtained with an Eulerian average include the effect of jet meandering, obscuring the evidence of the jet structure, shown by the intermittency values of less than one in the jet core region and by the triangular shaped profiles.

Further understanding of the jet dynamics in a HIT ambient is obtained from the analysis of the PDFs and corresponding CDFs of the jet centerline concentrations. In the quiescent ambient, the PDFs of the centerline concentration are almost Gaussian with the lowest concentration non-zero and decreasing with the axial distance, as seen in Fig. 4.17 for the Re = 10600 and 5800 jets. By comparison, in the power-law region of the jet (x/d = 20 - 60 at Re = 10600 and x/d = 20 - 40 at Re = 5800), turbulence in the ambient results in a greater occurrence of lower concentrations as expected from the lower mean centerline concentrations (observed from the centroidal average). The PDFs become skewed toward the lower concentrations, with lower maxima and a minimum of zero. The maximum concentrations (defined by the 98th percentile of the CDF) are reduced compared to the quiescent case by 10 - 25% and 25 - 35% for the Re = 10600 and Re = 5800 jets, respectively. The wider PDFs, in general, suggest a lower scalar mixing compared to the quiescent ambient (as argued in Nedić and Tavoularis (2016)). The probability of concentrations below the threshold increases with downstream distance and is due to discontinuities in the jet due to its lateral advection by large eddies in the ambient leaving isolated islands of the scalar. After jet breakup (x/d > 40 for Re = 5800 jet), there are an increased number of lower concentrations and a sharply increasing occurrence of below threshold concentra-

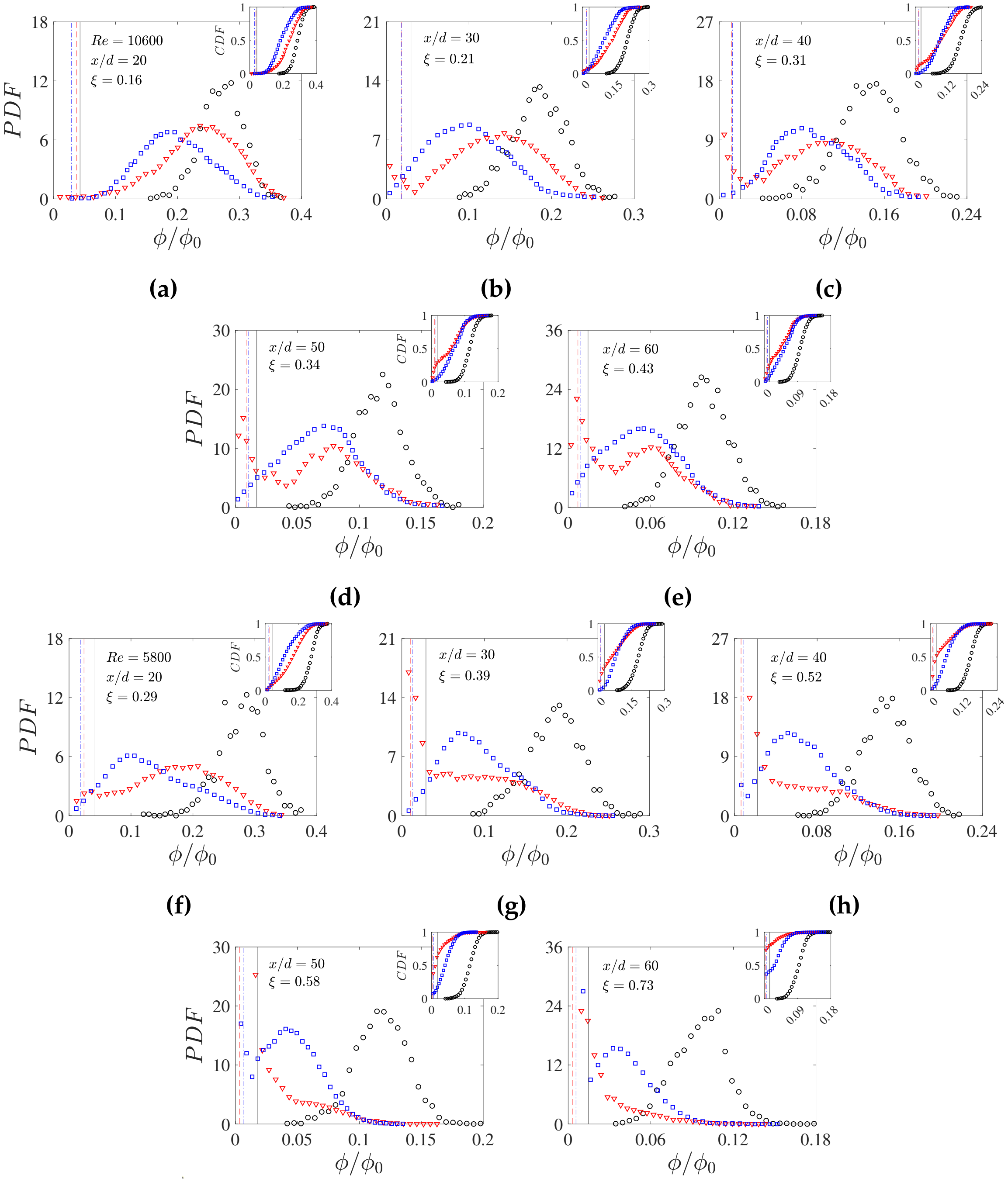

(a) **(b)** **(c)**

(d) **(e)**

(f) **(g)** **(h)**

(i) **(j)**

Figure 4.17: PDF of centerline concentration. For Re = 10600 jet at (*a*) x/d = 20, (*b*) 30, (*c*) 40, (*d*) 50, and (*e*) 60. Similarly, for Re = 5800 jet at (*f*) to (*j*) for x/d = 20 to 60. Symbols: ○ quiescent ambient; □ centroidal, and ▽ Eulerian averaging in HIT ambient. The solid, dashed and dashed-dotted lines show the corresponding threshold values, ϕ_t/ϕ_0, in the quiescent ambient, and the Eulerian and centroidal averaging methods in HIT ambient, respectively. The insets depict the corresponding CDF values in the quiescent and in the HIT ambient.

tions (12% at x/d = 50 and 40% at x/d = 60 for the centroidal average of the Re = 5800 jet). The PDFs and CDFs obtained from Eulerian averaging again obscure the detail of the jet structure, but do indicate a greater frequency of lower concentrations, while the greatly increased likelihood of below threshold or zero concentrations is due to the inclusion of the effect of jet meandering on the analysis.

We hypothesize that greater local scalar concentration gradients occur within the boundary of the jet in the HIT ambient, as compared to the quiescent case, due to entrainment of the small-scale turbulence of the ambient (see Fig. 4.16 for instantaneous concentration fields). This is plausible due to the increased rms concentrations in the jet and the increased range of the centerline concentration seen in the PDFs. The presence of increased local scalar gradients is corroborated by the greater differential diffusion observed for a jet in a turbulent ambient as compared to a quiescent ambient (Lavertu, 2006) (jet Re = 10600 and same HIT). This hypothesis could be validated by directly calculating the local instantaneous concentration gradients within the jet boundary; however, lack of sufficient spatial resolution prevents us from capturing the Batchelor microscale ($\eta_B = \eta Sc^{-1/2}$), which in turn greatly underestimates the calculation of the scalar gradients.

The time-averaged net entrainment into the jet in a HIT ambient is decreased compared to the quiescent case due to the lower characteristic jet velocity driving the entrainment (Khorsandi et al., 2013) and due to greater detrainment induced by the background turbulence (Kankanwadi and Buxton, 2020). The increased detrainment is due to the frequent and extreme outward flux of detached jet fluid into the ambient as a result of the advection of the jet by large-scale ambient eddies and due to increased turbulent diffusion at the jet/ambient interface, TTI. In the quiescent ambient, the detached scalar patches are re-entrained into the jet within an eddy turnover time (Hussain and Clark, 1981), while in the turbulent ambient, re-entrainment is much weaker and the detached patches diffuse into the ambient (as seen by visualization, Fig. 4.16). After the jet breaks up, it is no longer self-similar and its intermittency increases. The decreased width of the intermittency profile post breakup confirms that jet-driven entrainment is no longer occurring, and only turbulent and molecular diffusion is transporting the scalar. This is consistent with Hunt's hypothesis (Hunt, 1994) that forcing of a jet disrupts the jet structure and with previous experimental observations (Gaskin et al., 2004; Khorsandi et al., 2013; Perez-Alvarado, 2016; Lai et al., 2019).

4.5.4 Summary of the experimental observations

All the observations support a two-region model for the behavior of the jet in the HIT ambient, in which the regions are defined based on the ratio of the turbulence intensity between the ambient and the jet, ξ. In this study, for $\xi \leqslant 0.5$, the jet is perturbed by the HIT ambient, showing a faster decay of the centroidal mean concentration and a faster growth of the centroidal concentration half-width (both following power laws) compared to the quiescent case. Despite external forcing, the core of the jet is well preserved and the jet maintains its self-similarity and self-preservation in this region ($\xi \leqslant 0.5$). For $\xi > 0.5$, however, the decay of the mean concentration and the growth of the concentration half-width deviate from their power-law behaviors. The centroidally averaged concentration half-width stops growing, which (according to the entrainment theory) indicates that the jet-driven entrainment into the jet has stopped. The "no entrainment" status implies that the mean centerline velocity $\overline{U}_c$ and hence the global entrainment velocity, $E_v = \alpha\overline{U}_c$, are zero. This means that no "jet" exists beyond $\xi > 0.5$, and that the jet structure has been destroyed by the ambient turbulence. The destroyed jet structure for $\xi > 0.5$ is reflected in the scalar profiles in Fig. 4.14*c* no longer being self-similar, in the decayed jet core in the centroidal intermittency profiles (Fig. 4.15*i, j*), and in the increasing presence of the ambient fluid at the jet centroid of the centroidal CDFs (Fig. 4.17*i, j*). All the above discussions support the proposal of the two-region model for the jet in the HIT ambient, a sketch of which is illustrated in Fig. 4.18.

In fact, the two-region model is a refinement of the discussions from previous observations for the jet in a HIT ambient, stating that the behavior of the jet (as well as the entrainment process and subsequent scalar mixing) is different before and after the jet

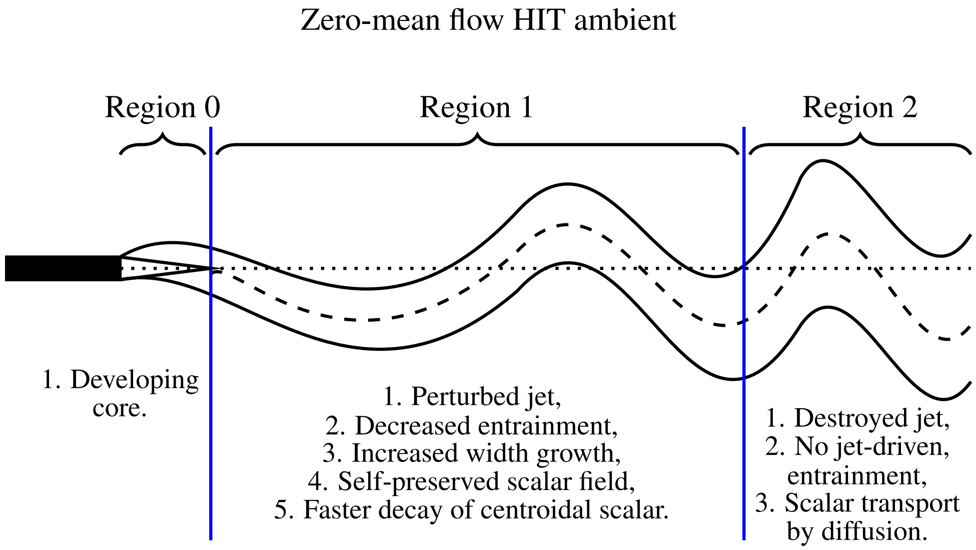

Figure 4.18: Schematic of the scalar field characteristics of a jet subjected to HIT ambient using the available data. The important properties of the two-region model is delineated with a centroidal averaging method. The jet axis and its centroid are shown with the dotted line and dashed line, respectively.

breakup (Khorsandi et al., 2013; Perez-Alvarado, 2016; Lai et al., 2019). In the present study, the centroidally averaged data allowed for the separation of the effect of the HIT ambient on the jet entrainment from the effect of the HIT causing the jet path to meander. Using this method, the structure of the jet is more apparent, and it is clearly visible that beyond $\xi = 0.5$ the jet has been destroyed by the ambient turbulence eddies and no longer exists. In Eulerian averages (of the above studies), the evolution and structure of the jet are partially obscured due to the inclusion of jet meandering.

4.6 Conclusion

The effect of an approximately homogeneous and isotropic turbulence with a negligible mean flow on the evolution of the structure and the dynamics of an axisymmetric turbulent jet, with Re = 10600 and Re = 5800, was investigated by analyzing the passive scalar field. Planar laser-induced fluorescence was used to visualize the jet and the measured scalar statistics were compared to those of the jet issuing into a quiescent ambient. The scalar statistics were conditioned on the jet centroid to separate the effects of the larger and smaller scale ambient eddies on the jet dynamics, which were also compared to classical Eulerian statistics.

Turbulence in the ambient reduces jet entrainment and results in a rapid jet breakup. This is due to the disruption of jet structure by external forcing as hypothesized by Hunt (1994), contrary to the long-held intuitive assumption that jet dilution and turbulent diffusion can be superimposed.

A two-region model for the jet evolution and structure, when released into the turbulent ambient, is proposed based on averages conditioned on the jet centroid (Fig. 4.18). In the first region, following the developing jet region, the ambient turbulence disrupts the jet structure, due to modulation of the jet interface, meandering of the jet by the large eddies, and entrainment of the turbulent ambient fluid, resulting in a faster decay of the jet and decreased entrainment. In the second region, identified as where the relative turbulence intensity $\xi > 0.5$, the ambient turbulence has destroyed the jet structure. Although scalar remains, as there is no momentum to drive the entrainment, the momentum-driven mechanism for scalar transport is replaced by turbulent/molecular diffusion by the ambient eddies. The relative lengths of the two regions depend primarily on the relative turbulence intensity, ξ, between the ambient and the jet, as assessed by the centroidal analysis, which removes the effect of the relative length scale ($\mathcal{L}$) on the jet behavior in the HIT ambient.

The first region (the perturbed jet region) is of particular interest as the jet structure is present, but its dynamics are modified by the ambient turbulence. The mean properties of the scalar remain self-similar and self-preserved when conditioned on the jet centroid (i.e., following the meandering jet path), but have greater concentration decay ($\overline{\phi_c}$) and half-width growth rate ($b_{\phi,1/2}$). The ambient turbulence increases the modulation of the jet/ambient interface. The entrainment of the ambient turbulence increases the rms concentrations and is hypothesized to increase local concentration gradients within the jet.

The same power-law behavior in the perturbed jet region for the decay of the mean centroidal concentration, concentration rms, and width growth for both jet Reynolds numbers indicates the universality of the evolution of the scalar statistics in the HIT ambient, provided the jet structure is preserved. To further investigate the effect of ambient turbulence on scalar mixing in jets, a larger range of Reynolds numbers and ambient turbulence conditions (ξ and $\mathcal{L}$) as well as simultaneous velocity and scalar measurements are recommended.

4.7 Effect of the threshold value on the position of the centroid

The mean location of the centroids exhibited by red circle markers in Fig. 4.3 are the ensemble average of the instantaneous centroids, calculated from the bulk of the flow without applying a threshold to the scalar fields. Regions characterized by intense values of passive scalar often control the position of the centroid, as evident from its definition in Eq. 4.10. However, large-scale meandering of the jet in the presence of HIT ambient often results in non-trivial values of passive scalar being pushed out of the FOV. Thus, in order to check the validity of the centroidal analysis presented throughout the manuscript, we investigate the relationship between the average location of the centroid and a wide range of scalar thresholds. The radial position, R_C, and orientation, θ_C, of the centroids calculated for regions where the local concentration is larger than the threshold value are expressed in the following equations:

$$R_C = \frac{\int \left(r \, \mathrm{d}\phi\right) |_{\phi > \phi_t}}{\int \mathrm{d}\phi|_{\phi > \phi_t}}, \tag{4.10}$$

$$\theta_C = -\tan^{-1}\left(\frac{z_C}{y_C}\right), \tag{4.11}$$

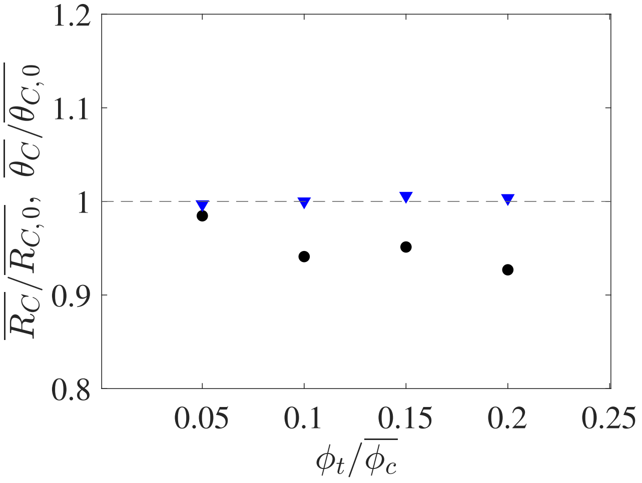

Figure 4.19: Variation of $\overline{R_C}$ and $\overline{\theta_C}$ versus $\phi_t/\overline{\phi_c}$ normalized by their respective unthresholded values. Data for Re = 5800 at x/d = 60. Symbols: ●, $\overline{R_C}$; ▼, $\overline{\theta_C}$.

where y_C and z_C denote the coordinates of the instantaneous centroids calculated from thresholded scalar fields, i.e., $R_C^2 = y_C^2 + z_C^2$.

Figure 4.19 shows the ensemble averaged radial location, $\overline{R_C}$, and orientation, $\overline{\theta_C}$, of the centroids for the worst case scenario, that is, Re = 5800 jet at $x/d = 60$ against a range of thresholds. As can be seen, the orientation is quite insensitive to the threshold value. More importantly, one can observe only slight changes in the radial location of the centroid with increasing values of the scalar threshold. Specifically, by applying $\phi_t/\overline{\phi_c} = 0.15$, which is the threshold for detecting the jet region (Sec. 4.5.3), the radial position changes by 5% relative to the unthresholded value. Furthermore, thresholding the scalar fields results in centroids being closer to the jet axis, implying the existence of intense concentration values near the geometrical centerline even in the presence of extreme meandering. Overall, we deduce that the position of the centroids are well-defined.

4.8 Effect of threshold value on the intermittency profiles

The location of the outer boundary demarcating the high-*Sc* flows and the ambient shows small sensitivity to the chosen threshold due to the weak diffusive nature of the passive

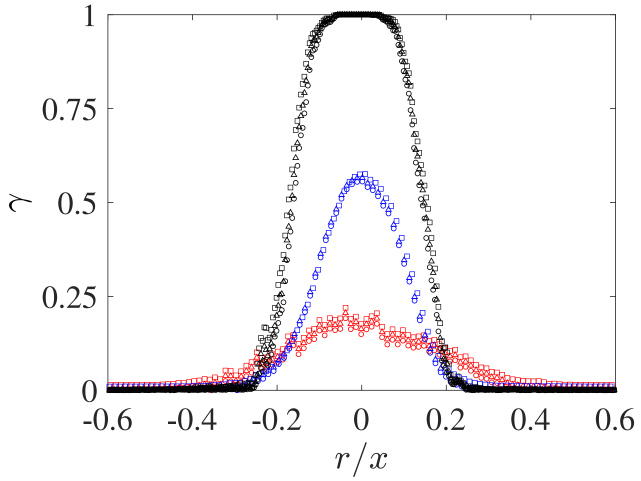

Figure 4.20: Variation of intermittency profiles versus ϕ_t. Data for Re = 5800 at x/d = 60. Symbols: □, $\phi_t/\overline{\phi_c}$ = 0.13; △, $\phi_t/\overline{\phi_c}$ = 0.15; ∘, $\phi_t/\overline{\phi_c}$ = 0.17. Black, blue, and red marker colors correspond to quiescent, centroidal turbulent, and Eulerian turbulent backgrounds, respectively.

scalar (e.g., see Westerweel et al. (2009)). However, this may not be the case in turbulent backgrounds due to the presence of appreciable amounts of passive scalar (close to the threshold concentration value) in the ambient. Here, we investigate the effect of varying the scalar threshold on the intermittency profiles presented in Fig. 4.15. To this end, we employ thresholds in the range of $\phi_t/\overline{\phi_c} = 0.15 \pm 13\%$ and recalculate the intermittency profiles in the quiescent and the turbulent background cases. Figure 4.20 shows the intermittency profiles for the worst case scenario, i.e., x/d = 60 at Re = 5800 jet. Indeed, there are only slight changes in the detected jet regions for different values of the scalar threshold, as made evident by the approximate collapse of the intermittency profiles. Therefore, we conclude the robustness of the present criterion for detecting the jet interface even when the jet is subjected to HIT ambient, independent of the averaging method, that is, Eulerian or centroidal.

References

B. R. Morton, G. I. Taylor, and J. Turner, “Turbulent gravitational convection from maintained and instantaneous sources,” *Proc. R. Soc. London, Ser. A* 234, 1–23 (1956).

M. van Reeuwijk and J. Craske, “Energy-consistent entrainment relations for jets and plumes,” *J. Fluid Mech.* 782, 333–355 (2015).

A. A. Townsend, “The mechanism of entrainment in free turbulent flows,” *J. Fluid Mech.* 26, 689–715 (1966).

W. J. A. Dahm and P. E. Dimotakis, “Measurements of entrainment and mixing in turbulent jets,” *AIAA J.* 25, 1216–1223 (1987).

S. Corrsin and A. L. Kistler, “Free-stream boundaries of turbulent flows,” Report No. NACA-TR-1244 (National Advisory Committee for Aeronautics, 1955).

J. Mathew and A. J. Basu, “Some characteristics of entrainment at a cylindrical turbulence boundary,” *Phys. Fluids* 14, 2065–2072 (2002).

C. B. da Silva, J. C. R. Hunt, I. Eames, and J. Westerweel, “Interfacial layers between regions of different turbulence intensity,” *Annu. Rev. Fluid Mech.* 46, 567–590 (2014).

S. Gaskin, M. McKernan, and F. Xue, “The effect of background turbulence on jet entrainment: An experimental study of a plane jet in a shallow coflow,” *J. Hydraul. Res.* 42, 533–542 (2004).

J. C. R. Hunt, “Atmospheric jets and plumes,” *in Recent Research Advances in the Fluid Mechanics of Turbulent Jets and Plumes* (Springer, 1994), Vol. 225.

B. Khorsandi, S. Gaskin, and L. Mydlarski, “Effect of background turbulence on an axisymmetric turbulent jet,” *J. Fluid Mech.* 736, 250–286 (2013).

A. Perez-Alvarado, “Effect of background turbulence on the scalar field of a turbulent jet,” Ph.D. dissertation (McGill University, 2016).

A. C. Lai, A. W. K. Law, and E. E. Adams, “A second-order integral model for buoyant jets with background homogeneous and isotropic turbulence,” *J. Fluid Mech.* 871, 271–304 (2019).

C. Y. Ching, H. J. S. Fernando, and A. Robles, "Breakdown of line plumes in turbulent environments," *J. Geophys. Res.* 100, 4707–4713, (1995).

Y. Guo, D. Malcangio, P. A. Davies, and H. J. S. Fernando, "A laboratory investigation into the influence of a localized region of turbulence on the evolution of a round turbulent jet," *Fluid Dyn. Res.* 36, 75–89 (2005).

A. J. S. Cuthbertson, D. Malcangio, P. A. Davies, and M. Mossa, "The influence of a localised region of turbulence on the structural development of a turbulent, round, buoyant jet," *Fluid Dyn. Res.* 38, 683–698 (2006).

H. Wang and A. W. K. Law, "Second-order integral model for a round turbulent buoyant jet," *J. Fluid Mech.* 459, 397–428 (2002).

D. Legendre, A. Merle, and J. Magnaudet, "Wake of a spherical bubble or a solid sphere set fixed in a turbulent environment," *Phys. Fluids* 18, 048102 (2006).

Z. Amoura, V. Roig, F. Risso, and A. M. Billet, "Attenuation of the wake of a sphere in an intense incident turbulence with large length scales," *Phys. Fluids* 22, 055105 (2010).

I. Eames, C. Jonsson, and P. B. Johnson, "The growth of a cylinder wake in turbulent flow," *J. Turbul.* 12, N39 (2011).

P. E. Hancock and P. Bradshaw, "Turbulence structure of a boundary layer beneath a turbulent free stream," *J. Fluid Mech.* 205, 45–76 (1989).

A. Pal and S. Sarkar, "Effect of external turbulence on the evolution of a wake in stratified and unstratified environments," *J. Fluid Mech.* 772, 361–385 (2015).

K. S. Kankanwadi and O. R. Buxton, "Turbulent entrainment into a cylinder wake from a turbulent background," *J. Fluid Mech.* 905, A35 (2020).

J. Philip and I. Marusic, "Large-scale eddies and their role in entrainment in turbulent jets and wakes," *Phys. Fluids* 24, 055108 (2012).

S. Gaskin, A. Perez-Alvarado, and L. Mydlarski, "Impact of relative turbulence scales on the effect of background turbulence on jet flows," in 4th International Symposium of Shallow Flows (2017).

S. J. Wright, “The effect of ambient turbulence on jet mixing,” in *Recent Research Advances in the Fluid Mechanics of Turbulent Jets and Plumes* (Springer, 1994), Vol. 255, pp. 13–27.

M. Moeini, B. Khorsandi, and L. Mydlarski, “Effect of coflow turbulence on the dynamics and mixing of a non-buoyant turbulent jet,” *J. Hydraul. Eng.* 147, 04020088 (2021).

I. P. D. De Silva and H. J. S. Fernando, “Oscillating grids as a source of nearly isotropic turbulence,” *Phys. Fluids* 6, 2455–2464 (1994).

L. Mydlarski and Z. Warhaft, “On the onset of high-Reynolds-number grid generated wind tunnel turbulence,” *J. Fluid Mech.* 320, 331–368 (1996).

P. Lavoie, L. Djenidi, and R. A. Antonia, “Effects of initial conditions in decaying turbulence generated by passive grids,” *J. Fluid Mech.* 585, 395–420 (2007).

D. Webster and A. Brathwaite, “A novel laboratory apparatus for simulating isotropic oceanic turbulence at low Reynolds number,” *Limnol. Oceanogr.* 2, 1–12 (2004).

E. A. Variano and E. A. Cowen, “A random-jet-stirred turbulence tank,” *J. Fluid Mech.* 604, 1–32 (2008).

E. A. Variano, E. Bodenschatz, and E. A. Cowen, “A random synthetic jet array driven turbulence tank,” *Exp. Fluids* 37, 613–615 (2004).

D. Carter, A. Petersen, O. Amili, and F. Coletti, “Generating and controlling homogeneous air turbulence using random jet arrays,” *Exp. Fluids* 57, 1–15 (2016).

A. Perez-Alvarado, L. Mydlarski, and S. Gaskin, “Effect of the driving algorithm on the turbulence generated by a random jet array,” *Exp. Fluids* 57, 20 (2016).

H. J. S. Fernando and I. P. D. De Silva, “Note on secondary flows in oscillating grid, mixing-box experiments,” Phys. Fluids 5, 1849–1851 (1993).

T. M. Lavertu, L. Mydlarski, and S. Gaskin, “Differential diffusion of high-Schmidt-number passive scalars in a turbulent jet,” *J. Fluid Mech.* 612, 439–475 (2008).

P. E. Dimotakis, “The mixing transition in turbulent flows,” *J. Fluid Mech.* 409, 69–98 (2000).

T. M. Lavertu, “Differential diffusion in a turbulent jet,” Ph.D. dissertation (McGill University, 2006).

K. F. Kohan and S. Gaskin, “The effect of the geometric features of the turbulent/non-turbulent interface on the entrainment of a passive scalar into a jet,” *Phys. Fluids* 32, 095114 (2020).

M. van Reeuwijk and M. Holzner, “The turbulence boundary of a temporal jet,” *J. Fluid Mech.* 739, 254–275 (2014).

C. A. Friehe, C. W. van Atta, and C. H. Gibson, “Jet turbulence: Dissipation rate measurements and correlations,” AGARD Turbul. Shear Flows 18, 1–7 (1971).

G. Guilbault, Practical Fluorescence: Theory, Methods, and Techniques (Marcel Dekker, 1973).

H. C. Burridge, D. A. Parker, E. S. Kruger, J. L. Partridge, and P. F. Linden, “Conditional sampling of a high Peclet number turbulent plume and the implications for entrainment,” *J. Fluid Mech.* 823, 26–56 (2017).

D. A. Parker, H. C. Burridge, J. L. Partridge, and P. F. Linden, “A comparison of entrainment in turbulent line plumes adjacent to and distant from a vertical wall,” *J. Fluid Mech.* 882, A4 (2020).

H. B. Fischer, E. J. List, R. C. Y. Koh, J. Imberger, and N. H. Brooks, Mixing in Inland and Coastal Waters (Academic Press, 1979).

H. J. Hussein, S. P. Capp, and W. K. George, “Velocity measurements in a high-Reynolds-number, momentum-conserving, axisymmetric, turbulent jet,” *J. Fluid Mech.* 258, 31–75 (1994).

H. A. Becker, H. C. Hottel, and G. C. Williams, “The nozzle fluid concentration field of the round turbulent jet,” *J. Fluid Mech.* 30, 285–303 (1967).

D. R. Dowling and P. E. Dimotakis, “Similarity of the concentration field of gas-phase turbulent jets,” *J. Fluid Mech.* 218, 109–141 (1990).

A. W. K. Law and H. Wang, "Measurement of mixing processes with combined digital particle image velocimetry and planar laser induced fluorescence," *Exp. Therm. Fluid Sci.* 22, 213–229 (2000).

D. R. Webster, P. J. Roberts, and L. Ra'ad, "Simultaneous DPTV/PLIF measurements of a turbulent jet," *Exp. Fluids* 30, 65–72 (2001).

E. A. Cowen, K. A. Chang, and Q. Liao, "A single-camera coupled PTV-LIF technique," *Exp. Fluids* 31(1), 63–73 (2001).

C. Fukushima, L. Aanen, and J. Westerweel, "Investigation of the mixing process in an axisymmetric turbulent jet using PIV and LIF," in Laser Techniques for Fluid Mechanics (Springer, 2002), pp. 339–356.

C. L. Lubbers, G. Brethouwer, and B. J. Boersma, "Simulation of the mixing of a passive scalar in a round turbulent jet," *Fluid Dyn. Res.* 28, 189 (2001).

S. B. Pope, Turbulent Flows (Cambridge University Press, 2000).

J. Mi, D. S. Nobes, and G. J. Nathan, "Influence of jet exit conditions on the passive scalar field of an axisymmetric free jet," *J. Fluid Mech.* 432, 91–125 (2001).

P. Bagchi and S. Balachandar, "Response of the wake of an isolated particle to an isotropic turbulent flow," *J. Fluid Mech.* 518, 95 (2004).

G. S. Bhat and R. Narasimha, "A volumetrically heated jet: Large-eddy structure and entrainment characteristics," *J. Fluid Mech.* 325, 303–330 (1996).

A. Agrawal and A. K. Prasad, "Evolution of a turbulent jet subjected to volumetric heating," *J. Fluid Mech.* 511, 95–123 (2004).

J. C. LaRue and P. A. Libby, "Temperature fluctuations in the plane turbulent wake," *Phys. Fluids* 17, 1956–1967 (1974).

D. K. Bisset, J. C. R. Hunt, and M. M. Rogers, "The turbulent/non-turbulent interface bounding a far wake," *J. Fluid Mech.* 451, 383–410 (2002).

M. Wolf, B. Luthi, M. Holzner, D. Krug, W. Kinzelbach, and A. Tsinober, "Investigations on the local entrainment velocity in a turbulent jet," *Phys. Fluids* 24, 105110 (2012).

G. Balamurugan, A. Rodda, J. Philip, and A. C. Mandal, "Characteristics of the turbulent non-turbulent interface in a spatially evolving turbulent mixing layer," *J. Fluid Mech.* 894, A4 (2020).

M. Khashehchi, A. Ooi, J. Soria, and I. Marusic, "Evolution of the turbulent/non-turbulent interface of an axisymmetric turbulent jet," *Exp. Fluids* 54, 1449 (2013).

M. van Reeuwijk, J. C. Vassilicos, and J. Craske, "Unified description of turbulent entrainment," *J. Fluid Mech.* 908, A12 (2021).

K. Chauhan, J. Philip, and I. Marusic, "Scaling of the turbulent/non-turbulent interface in boundary layers," *J. Fluid Mech.* 751, 298–328 (2014).

K. U. Kim, G. S. Elliot, and J. C. Dutton, "Compressibility effects on large structures and entrainment length scales in mixing layers," *AIAA J.* 58, 5168 (2020).

N. Reuther and C. J. Kahler, "Evaluation of large-scale turbulent/non-turbulent interface detection methods for wall-bounded flows," *Exp. Fluids* 59, 121 (2018).

Y. Long, D. Wu, and J. Wang, "A novel and robust method for the turbulent/non-turbulent interface detection," *Exp. Fluids* 62, 138 (2021).

J. Westerweel, C. Fukushima, J. M. Pedersen, and J. C. R. Hunt, "Momentum and scalar transport at the turbulent/non-turbulent interface of a jet," *J. Fluid Mech.* 631, 199 (2009).

Z. Wu, J. Lee, C. Meneveau, and T. Zaki, "Application of a self-organizing map to identify the turbulent-boundary-layer interface in a transitional flow," *Phys. Rev. Fluids* 4, 023902 (2019).

B. Li, Z. Yang, X. Zhang, G. He, B. Deng, and L. Shen, "Using machine learning to detect the turbulent region in flow past a circular cylinder," *J. Fluid Mech.* 905, A10 (2020).

K. Younes, B. Gibeau, S. Ghaemi, and J. Hickey, "A fuzzy cluster method for turbulent/non-turbulent interface detection," *Exp. Fluids* 62, 73 (2021).

T. Watanabe, X. Zhang, and K. Nagata, "Turbulent/non-turbulent interfaces detected in DNS of incompressible turbulent boundary layers," *Phys. Fluids* 30, 035102 (2018).

M. Holzner and B. Luthi, “Laminar superlayer at the turbulence boundary,” *Phys. Rev.* Lett. 106, 134503 (2011).

D. Mistry, J. Philip, J. R. Dawson, and I. Marusic, “Entrainment at multi-scales across the turbulent/non-turbulent interface in an axisymmetric jet,” *J. Fluid Mech.* 802, 690–725 (2016).

R. Jahanbakhshi, “Mechanisms of entrainment in a turbulent boundary layer,” *Phys. Fluids* 33, 035105 (2021).

J. Nedić, and S. Tavoularis, “Measurements of passive scalar diffusion downstream of regular and fractal grids,” *J. Fluid Mech.* 800, 358–386 (2016).

A. K. M. F. Hussain and A. R. Clark, “On the coherent structure of the axisymmetric mixing layer: A flow-visualization study,” *J. Fluid Mech.* 104, 263–294 (1981).

Chapter 5

Diffusion of a passive scalar patch in turbulent ambient

The centroidal statistics of the jet in the turbulent ambient demonstrated that the time-averaged entrainment into the jet ceases beyond breakup, and turbulent diffusion becomes the dominant mechanism to transport the scalar field. This raises the question of how efficient the dilution of the jet due only to turbulent diffusion by the ambient eddies is compared to the case when the jet is diluted due concurrently by jet-driven entrainment and turbulent diffusion. It is also of interest to compare the evolution of a momentumless scalar patch having a width smaller than the size of the integral length scale of the ambient (i.e. L_{HIT} = 11 cm) to the destroyed jet, where the width of the jet reached a level comparable to L_{HIT}.

This chapter studies the temporal evolution of a momentumless patch of a passive scalar in approximately homogeneous isotropic turbulence with zero mean flow, which is due to turbulent diffusion by the ambient eddies. The results of this chapter contribute to our information about the behavior of the turbulent jet in the HIT ambient beyond breakup (Ch. 4). The evolution of the scalar patch is analyzed using the centroidal statistics of the mean and the rms concentrations, the characteristic width of the patch, the intermittency, and the PDFs and the CDFs of the centroidal concentration. A comparison between the effect of the turbulent diffusion on the evolution of the scalar patch and the destroyed jet is provided. A qualitative discussion about the turbulent diffusivity is carried out, with recommendations for a quantitative study of the turbulent diffusivity tensor in the present setup.

5.1 Introduction

Turbulent diffusion describes the contribution of turbulent eddies in dispersion and mixing of admixtures. Dispersion of environmental pollutants and air/fuel mixing in combustion engines are common examples of turbulent diffusion. Predicting turbulent diffusion in engineering applications uses an eddy diffusivity in terms of mean concentration, which is a function of the flow turbulence. Knowledge of the evolution of the mean concentration allows for a rough estimation of the diffusivity, while in a number of applications (such as maximum exposure of humans to air pollutants and peak probability of combustion of flammable gases accidentally released into the atmosphere), statistical variation of the concentration fluctuations is also required (Roberts and Webster, 2002). An accurate estimation of turbulent diffusion can be achieved by empirical measurement of the flux of the scalar due to turbulent motions (e.g. Vanderwel and Tavoularis (2014a)).

Discussion of turbulent diffusion was initiated by Taylor in his pioneering work (Taylor, 1921), in which the variance of the displacement of fluid elements from a fixed-point source in a one-dimensional, stationary homogeneous turbulence was expressed in terms of the Lagrangian turbulence properties:

$$\overline{X^2}(t) = 2\overline{\tilde{u}^2}\int_0^t (t-\tau)R(\tau)\,d\tau \tag{5.1}$$

where X is the displacement of a fluid element in time t, $\tilde{u}$ represents the Lagrangian velocity fluctuations ($\tilde{U} = dX/dt = \overline{\tilde{U}} + \tilde{u}$), and $R(\tau)$ is the auto-correlation function of the Lagrangian velocity. Taylor (1921) estimated the rate of dispersion,

$$D(t) = \frac{1}{2}\frac{d\overline{X^2}(t)}{dt} = \overline{\tilde{u}^2}\int_0^t R(\tau)\,d\tau, \tag{5.2}$$

for two regimes of diffusion at the limits of short and long times as (Anand and Pope, 1985):

$$D(t) \approx \begin{cases} \overline{\tilde{u}^2}t & \text{for} \quad t \ll T \\ \overline{\tilde{u}^2}T & \text{for} \quad t \gg T \end{cases} \tag{5.3}$$

where $T = \int_0^\infty R(\tau)\,d\tau$ is the Lagrangian integral timescale of the turbulence. At smaller times, the turbulent convection regime occurs, during which the rate of dispersion grows linearly with time. At large enough times, in the turbulent diffusion regime, the rate of dispersion will eventually reach an asymptote, which depends only on the Lagrangian integral timescale of the turbulence and the variance of the Lagrangian velocity fluctuations.

Batchelor (1949) extended Taylor's theory to three-dimensional turbulence by defining a three-dimensional turbulent diffusivity tensor, $\mathcal{D}_{ij}(t) = \frac{\mathrm{d}\overline{X_i(t)X_j(t)}}{2\mathrm{d}t}$, in terms of the mean Lagrangian displacement tensor, $\overline{X_i(t)X_j(t)}$, of a fluid particle in a homogeneous turbulence. Theoretical arguments have been used to derive asymptotic expressions for the turbulent diffusivity in shear flows (Corrsin, 1975; Tavoularis and Corrsin, 1985; Rogers et al., 1989; Younis et al., 2005), among which Corrsin (1975) suggested the estimation of the asymptotic values of the $\mathcal{D}_{ij}$ tensor from Eulerian turbulence properties; i.e. the Eulerian integral timescale and the Eulerian velocity fluctuations.

The effect of molecular diffusion was added to Taylor's theory by Saffman (1960):

$$\overline{X^2}(t) = 2\overline{\tilde{u}^2}\int_0^t (t-\tau)R(\tau)\,d\tau + 2\mathcal{D}t, \tag{5.4}$$

where $\mathcal{D}$ is the molecular diffusivity. The role of molecular diffusion is to increase the mean square displacement of the fluid particles at the initial stages of diffusion. With time, and once the mean square displacement is of the order of the smallest eddy sizes, turbulent convection starts, and when the mean square displacement is sufficiently larger than the integral length scale, turbulent diffusion dominates the diffusion process (Uberoi and Corrsin, 1952; Sawford, 2001). Molecular diffusion is dominant close to a source, a boundary or where buoyancy effects and chemical reactions are involved (Chatwin and Sullivan, 1979), while turbulent diffusion is the main mechanism transporting the scalar in high Reynolds number flows (Saffman, 1960). It is noted that in stationary homogeneous turbulence, the interaction between molecular diffusion and turbulent diffusion reduces the overall diffusion compared to the case when they act independently and are linearly additive (Saffman, 1960).

Diffusion of a low-concentration passive scalar in a turbulent flow is governed by the Reynolds-averaged advection-diffusion equation:

$$\frac{\partial \overline{\phi}}{\partial t} + \underbrace{\overline{U_i}\frac{\partial \overline{\phi}}{\partial x_i}}_{\text{advection}} = \underbrace{\mathcal{D}\frac{\partial^2 \overline{\phi}}{\partial x_i^2}}_{\text{molecular diffusion}} + \underbrace{\frac{\partial(-\overline{\phi' u_i})}{\partial x_i}}_{\text{turbulent diffusion}} , \tag{5.5}$$

where $\overline{\phi}$ and $\overline{U_i}$ are the mean concentration and the mean velocity, respectively, and $\overline{\phi' u_i}$ is the turbulent scalar flux vector. Equation 5.5 is open in $\overline{\phi}$, and it can be closed if $\overline{\phi' u_i}$ is expressed in terms of the mean concentration using a turbulent diffusivity tensor. The first-order gradient transport model (Arya, 1999) is a common closure model for the turbulent scalar flux, i.e. $-\overline{\phi' u_i} = \mathcal{D}_{ij}\frac{\partial \overline{\phi}}{\partial x_j}$, where $\mathcal{D}_{ij}$ is the turbulent diffusivity tensor, the values of which depend on the turbulence properties of the flow (Arya, 1999; Roberts and Webster, 2002). Components of the $\mathcal{D}_{ij}$ can be defined experimentally by the measurement of the local magnitude and directions of the mean scalar derivatives and velocity–scalar covariances (Vanderwel and Tavoularis, 2014a).

Diffusion of heat and scalar concentration released from point and line sources have been studied in several turbulent flows. Examples include point source plumes in channel flow (Webster et al., 2003; Rahman and Webster, 2005; Mohaghar et al., 2020), grid turbulence (Connor et al., 2018), fan-generated flow (Halloran et al., 2014) and uniformly sheared flow (Britter et al., 1983; Vanderwel and Tavoularis, 2014a), line source in channel flow (Lavertu and Mydlarski, 2005; Lepore and Mydlarski, 2011; Germaine et al., 2014), grid turbulence (Taylor, 1935; Uberoi and Corrsin, 1952; Townsend, 1954; Warhaft, 1984; Anand and Pope, 1985; Stapountzis et al., 1986; Nedić and Tavoularis, 2016), and uniformly sheared flow (Tavoularis and Corrsin, 1981; Karnik and Tavoularis, 1989).

Experimental studies of plumes in turbulent flows show a Gaussian distribution of the mean scalar profiles (Fackrell and Robins, 1982; Webster et al., 2003; Crimaldi and Koseff, 2006; Vanderwel and Tavoularis, 2014a; Nedić and Tavoularis, 2016; Connor et al., 2018), confirming the results of the earlier turbulent diffusion studies (Taylor, 1935; Uberoi and Corrsin, 1952; Townsend, 1954). For a point source continuous plume in a uniform mean velocity turbulent flow, assuming a negligible diffusivity in the streamwise direction (x) and uniform and equal turbulent diffusivities in the cross-stream directions (y, z), the Gaussian formula (Arya, 1999) predicts that the centerline concentration decays as x^{-1} and the plume width grows with $x^{0.5}$ (Fischer et al., 1979; Arya, 1999). The Gaussian formula assumes a constant turbulent diffusivity, whereas in actual turbulent flows, the turbulent diffusivity evolves with downstream distance (Webster et al., 2003; Crimaldi and Koseff, 2006; Vanderwel and Tavoularis, 2014a), and hence the evolution of the centerline concentration and the plume width would deviate from the theoretical predictions (Warhaft, 1984; Anand and Pope, 1985; Webster et al., 2003; Rahman and Webster, 2005; Lepore and Mydlarski, 2011; Vanderwel and Tavoularis, 2014a).

The diffusion of a passive scalar in a turbulent ambient is dependent on the properties of the flow (Roberts and Webster, 2002) and the assessment of its magnitude can be only achieved through the experimental data. This study investigates the diffusion of a high Schmidt number, momentumless patch of a passive scalar in a RJA-generated HIT ambient. The turbulence properties of the HIT ambient have been previously documented by Khorsandi et al. (2013) and Perez-Alvarado et al. (2016). Statistics of the scalar field are used to analyze the temporal evolution of the passive scalar field, which is due to turbulent diffusion and molecular diffusion in the turbulent ambient and in the quiescent ambient, respectively. The motivation of this work is to better understand the effect of the RJA eddies on dilution of the passive scalar field of a turbulent jet beyond its breakup point in the HIT ambient, where the momentum-driven entrainment of the jet stops and the turbulent diffusion is the only mechanism for the scalar transport (Sahebjam et al., 2022). The objective of this study was initially to quantify the diffusivity of the scalar patch due to the ambient turbulence created with the RJA through the simultaneous measurement of the velocity and the concentration fields. However, the velocity measurements (i.e. particle image velocimetry) were not available in the lab, and therefore, only the concentration analysis is carried out, providing a qualitative measurement of turbulent diffusion.

The experimental apparatus for generating the momentumless scalar patch, the measurement technique, and the data acquisition are described in Sec. 5.2. Section 5.3 presents the results and a discussion of the diffusion of the passive scalar field in the RJA-generated HIT ambient as compared to that in a quiescent ambient, and section 5.4 summarizes the conclusions.

5.2 Experimental setup

A jet was isokinetically released into a quiescent and a turbulent ambient with zero mean velocity, and the temporal evolution of the resulting momentumless passive scalar field was measured by the PLIF technique. This section describes the experimental facility and the measurement apparatus, a schematic of which is provided in Fig. 5.1.

5.2.1 Experimental measurement

The experiments were conducted in a $1.5 \times 2.4 \times 1 \ \mathrm{m}^3$ subsection of a $1.5 \times 6 \times 1 \ \mathrm{m}^3$, free-surface glass water tank. The ambient fluid was either quiescent or turbulent. The turbulence in the ambient was generated using a random jet array (RJA) (based on that in Variano and Cowen (2004) and Variano et al. (2008), and built to a larger size) to achieve an approximately homogeneous isotropic turbulence (HIT) with zero mean flow at the

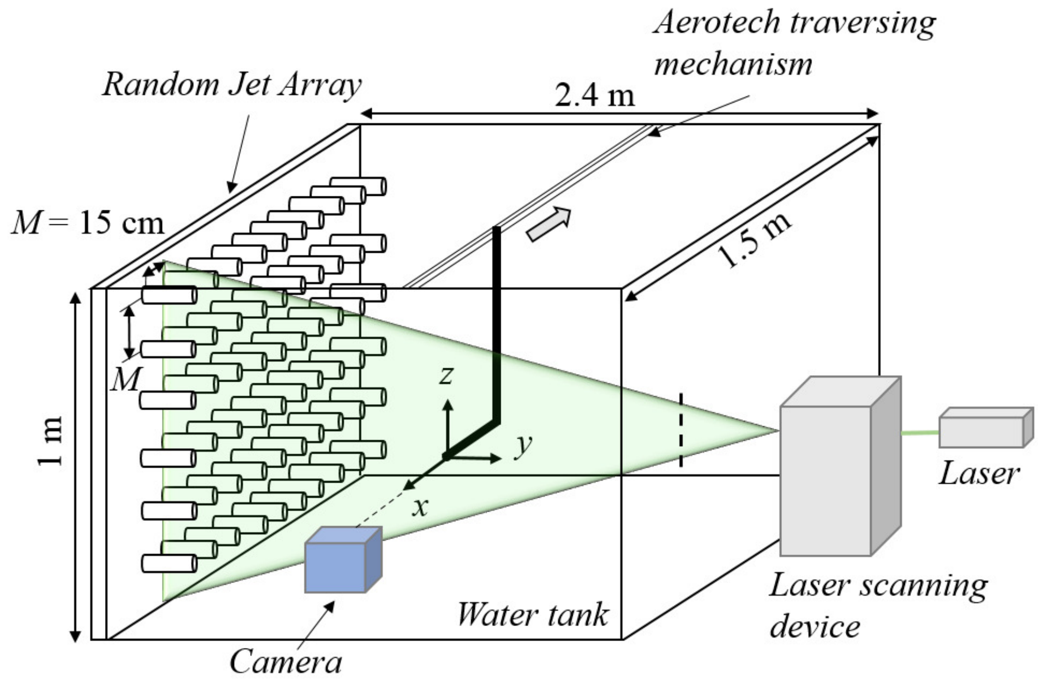

Figure 5.1: Schematic of the experimental apparatus and the PLIF setup.

measurement location (Khorsandi et al., 2013; Perez-Alvarado, 2016). The RJA has of 6 rows and 10 columns of water jets generated by bilge pumps mounted symmetrically on a 1.5 × 1 polyethylene sheet with a center to center distance of M = 150 mm. The RJA was operated by ”RANDOM” algorithm (Variano et al., 2008; Perez-Alvarado et al., 2016) to achieve a high level of homogeneity downstream of the jets, where the jet flows merge to form the HIT ambient. The RANDOM algorithm turned the jets independently on and off using parameters selected from two normal distributions with $(\mu_{on}, \sigma_{on}) = (12, 4)$ s and $(\mu_{off}, \sigma_{off}) = (108, 36)$ s, resulting in almost 10% of the pumps operating at any instant. The experimental parameters are provided in Table 5.1. For more details on the RJA setup, the reader is referred to Lavertu et al. (2008), Khorsandi et al. (2013), and Perez-Alvarado (2016).

The axisymmetric jet was released isokinetically parallel to the RJA plane to generate an approximately momentumless, shear-free patch of a passive scalar. The jet discharged horizontally at a transverse distance of y/M = 7.3 from the RJA plane, where the turbulent kinetic energy (TKE) of the HIT ambient was k_{HIT} = 4.4 $\mathrm{cm}^2\,\mathrm{s}^{-2}$ (Khorsandi et al., 2013). The jet, which extended vertically for 1 m then horizontally for 0.45 m, was towed backwards during its discharge at a speed equal to the jet exit velocity, and hence an approximately zero mean momentum of the dyed fluid relative to the ambient fluid was achieved. Towing of the jet at the same speed as the exit velocity, minimized the velocity gradient between the dyed fluid and the ambient, causing the production of turbulence due to velocity shear to be minimal (Webster et al., 2003). An Aerotech traversing mechanism was used to move the jet along a monorail (Schneeberger Monorail AMSD-4A) that spanned the tank width. The Aerotech mechanism was controlled by an Aerotech SOLOIST CP10 controller, and could operate at a range of speeds (up to 1.1 m/s), with the possibility to define the acceleration and deceleration rates of the motion.

Towing the jet (i.e. the one used in the turbulent jet tests with d = 8 mm) backwards, however, generated vortices that propagated towards the laser sheet causing disturbances at the measurement location. To minimize those disturbances, a relatively large-diameter jet (d = 29.97 mm inner diameter) was used to attain a desirable flow rate at a relatively low exit velocity (and hence a low towing speed). Also, the horizontal section of the jet was 0.45 m (15d) in length to place the vertical section well behind the laser sheet to reduce the effect of the vortex shedding in the measurement plane. The optimal jet exit velocity, and equally, the towing speed, were determined empirically such that a continuous flow of the dyed fluid was attained at the jet exit, while keeping the flow disturbances due to towing of the jet minimal. A flow rate of 0.757 $\mathrm{l}\,\mathrm{min}^{-1}$, corresponding to a towing speed of 18 $\mathrm{mm}\,\mathrm{s}^{-1}$ and a Reynolds number of Re = 540 was selected as the optimal flow rate in the present study. The acceleration/deceleration rate was set to 1 $\mathrm{m}\,\mathrm{s}^{-2}$ to achieve an approximately constant-velocity motion during the towing of the jet.

The concentration field of the momentumless scalar patch was measured using the PLIF method, with Rhodamine 6G (95% purity, Sigma-Aldrich Company Ltd.) as the passive scalar tracer. Rhodamine 6G has a Schmidt number of $Sc \approx 2500$ (Gendron et al.,

Table 5.1: Experimental parameters. Note that $k_{HIT} = (2\overline{u^2_{rms,HIT}} + \overline{v^2_{rms,HIT}})/2$, $L_{HIT} = \int_0^\infty \frac{\overline{u_{HIT}(\mathbf{x})\, u_{HIT}(\mathbf{x}+r e_x)}}{u^2_{rms,HIT}}\, \mathrm{d}r$ and $Re_{\lambda,\,HIT} = \left(\sqrt{150\, k_{HIT}}\, L_{HIT}/\nu\right)^{1/2}$.

Schmidt number	Sc	2500
Jet exit velocity	U_0	18 mm s^{-1}
Jet exit inner diameter	d	29.97 mm
Lateral jet position to RJA	y/M (M = 150 mm)	7.3
Ambient TKE (at $y/\mathrm{M} = 7.3$)	k_{HIT}	4.4 $\mathrm{cm}^2\mathrm{s}^{-2}$
Ambient length scale (at $y/\mathrm{M} = 7.3$)	L_{HIT}	110 mm
Ambient turbulent Reynolds number	$Re_{\lambda,\,HIT}$	168
RJA operating algorithm	(μ_{on}, σ_{on}), $(\mu_{off}, \sigma_{off})$	(12, 4) s, (108, 36) s
PLIF spatial resolution	-	0.128 mm × 0.128 mm
Field of view	FOV	260 mm × 260 mm
Sampling frequency	-	50 Hz

2008), and energy absorption and energy emission spectra peaks at 525 nm and 554 nm, respectively (Crimaldi, 1997). A continuous mode laser (1.5 W, 532 nm, Dragon Lasers Ltd.) was operated at 1 W, and an eight-sided polygonal mirror generated rotating at 12000 rpm generated a 1.5 mm thick laser sheet to illuminate an orthogonal cross section of the scalar patch. A 12-bit, 4 Megapixel CMOS camera (pco.dimax) with a 50 mm Pentax lens was used to record the concentration field at 50 Hz. The field of view of the camera was 260 × 260 mm^2, corresponding to a resolution of 0.13 × 0.13 mm^2 per pixel. A 550 nm longpass color filter (ThorLabs FGL550) was attached to the camera lens to filter scattered laser light and transmit only the fluorescence signal to the camera lens.

A dilute concentration of Rhodamine 6G dye (0.015 mg/L) was mixed into the jet water supply, which was pumped to a constant-head reservoir (3 m above the jet level) to feed the jet by a gravity-driven flow at a constant flow rate. For each test, the background light intensity level was recorded to be subtracted from the PLIF images. The jet flow rate was adjusted using a ball valve, and was measured with a ±5% precision flow meter (Blue-White F400). It was important to ensure the jet fluid exited the jet continuously for a few seconds prior to the start of the towing. Image recording was triggered once the tip of the jet crossed the laser sheet, and the jet flow was stopped at the end of its travel to avoid a momentum-driven jet flow.

The use of a dilute concentration of Rhodamine 6G dye ensured a linear relationship between the dye concentration and the fluorescent light intensity, the coefficients of which were obtained in a calibration test, and were used to convert the pixel light intensities to the corresponding concentration levels. Also, the calibration test confirmed that the typical LIF errors, namely, attenuation, photobleaching, trapping, thermal blooming, and inertial effects, are minimal in the present measurements. The details of the calibration test and the PLIF error measurements are provided in Perez-Alvarado (2016) and Sahebjam et al. (2022).

5.2.2 Data acquisition

One and six PLIF tests were conducted in the quiescent ambient and in the turbulent ambient, respectively. The ideal test was the one with no advective transport of the passive scalar, which was approximately obtained at the beginning of the test for $t < 4$ s, before the vortex shedding caused by towing of the jet disturbed the measurement plane. Beyond that time, the passive scalar field is dispersed not only by diffusion, but (more effectively) by advection due to the vortices shed from the vertical section of the jet. 200 images were obtained for each test for $0 \leq t \leq 4$ s, where $t = 0$ denotes the time at which the tip of the jet crossed the laser sheet. The quiescent ambient test was carried out to benchmark the experimental apparatus. Due to symmetry of the scalar field in the quiescent ambient, the analysis is carried out on all diameters passing through the instantaneous centroid of the passive scalar field; i.e. a centroidal analysis (see Sahebjam et al. (2022) and Sec. 3.4.3). The temporal evolution of the passive scalar field in the quiescent ambient is obtained at $t = 0.2, 1, 1.8, 2.6, 3.4$ s, using six successive PLIF images at each time step to smooth the instantaneous fluctuations.

The measurement time in the turbulent ambient tests, was limited not only by vortex shedding but also by the scalar patch being advected laterally out of the field of view by large ambient eddies. The passive scalar field is obtained for $0 \leq t \leq 4$ s, and is assessed at time intervals of 0.4 s at time steps of 0.4 s (including 20 PLIF images), with their average values corresponding to t = 0.2, 1, 1.8, 2.6 and 3.4 s, similar to the quiescent ambient case. The use of relatively long time intervals was to smooth the large fluctuations of the extremely patchy concentration field in the turbulent ambient, in which the peak values of the isolated pockets sometimes reached values an order of magnitude larger than the time-averaged concentration. The analysis is carried out along all the radial profiles passing through the centroid which provides a composite average of the turbulence intensity to which the scalar patch is subject to (due to the decay of the turbulence intensity with distance from the RJA) (details in Sec. 5.3.1). The concentration value at any (r, θ) is approximated using bilinear interpolation, and then, the analyses are carried out as the azimuthally averaged values at the radius r.

5.3 Results and discussion

The effect of the turbulent velocity fluctuations on the transport of the passive scalar can be isolated if the advection term in the advection-diffusion equation (eq. 5.5) is negligible:

$$\frac{\partial \overline{\phi}}{\partial t} = \mathcal{D}\frac{\partial^2 \overline{\phi}}{\partial x_i^2} + \frac{\partial(-\overline{\phi' u_i})}{\partial x_i}. \tag{5.6}$$

In a quiescent ambient, temporal evolution of the momentumless patch of the passive scalar is due to molecular diffusion only, that is, $\frac{\partial \overline{\phi}}{\partial t} = \mathcal{D}\frac{\partial^2 \overline{\phi}}{\partial x_i^2}$, whereas in the turbulent ambient, turbulent diffusion dominates the diffusion process, and the molecular diffusion term can be neglected for $Sc \gg 1$ fluids, reducing the Eq. 5.6 to $\frac{\partial \overline{\phi}}{\partial t} = \frac{\partial(-\overline{\phi' u_i})}{\partial x_i}$.

The evolution of the passive scalar field has been assessed in terms of its mean concentration, the rms concentration, the intermittency of the concentration fluctuations, the characteristic size of the patch (i.e. equivalent diameter), the probability density functions (PDFs), and the cumulative distribution functions (CDFs) of the centerline concentration. First, diffusion of a scalar patch in a quiescent ambient is tested to benchmark the exper-

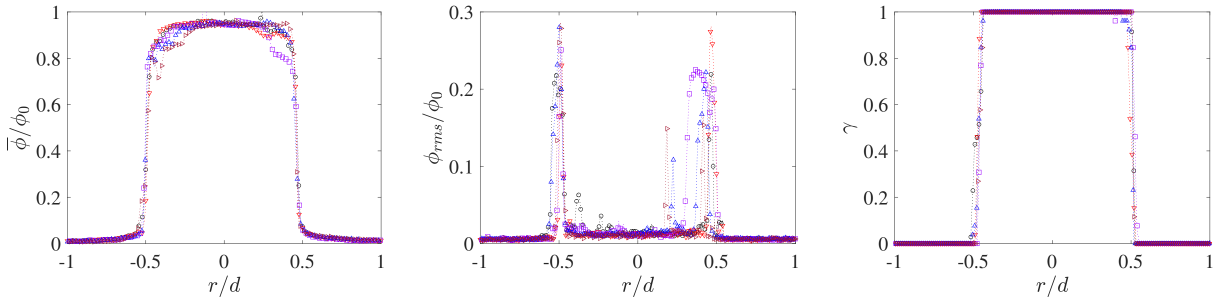

(a) **(b)** **(c)**

Figure 5.2: Radial profiles of the (*a*) mean concentration, (*b*) the rms concentration fluctuations, and (*c*) the intermittency of the scalar patch in a quiescent ambient. Symbols: ○ $t = 0.2$ s; ▽ $t = 1$ s; □ $t = 1.8$ s; △ $t = 2.6$ s; ▷ $t = 3.4$ s.

imental method. Figures 5.2 (*a*) and 5.2 (*b*) show the radial profiles of the mean concentration and the rms concentration of the momentumless patch of the passive scalar in a quiescent ambient, respectively, normalized by the initial concentration value, ϕ_0. The evolution of the passive scalar field is analyzed for $t = 0.2$, 1, 1.8, 2.6, and 3.4 s. Due to slow process of molecular diffusion, for the investigated time span, the mean concentration profiles almost collapse onto each other, having an approximately top-hat shape and a constant width. Batchelor-sized eddies act at the edges of the scalar field to smooth the profile by molecular diffusion. The rms concentration is greatest at the edges, which is an artifact of the scalar patch being advected slightly, and it is almost zero within the scalar field, indicating a homogeneous distribution of the concentration within the scalar patch. The intermittency of the scalar patch was obtained for a threshold value of $\phi_t/\phi_c = 0.15$ (Sahebjam et al., 2022), where ϕ_c is the corresponding centroidal concentration at each time interval. The intermittency profile (Fig. 5.2 (*c*)) follows a step function with a value of 1 across the width of the scalar patch and a zero value beyond it.

5.3.1 Diffusion in the turbulent ambient

The scalar field has a high spatial variation in the turbulent ambient due to stretching and folding processes associated with turbulent stirring. Turbulent stirring continues to stretch and fold the scalar patch, continually creating very steep gradients at which molecular diffusion acts to ultimately dilute and homogenize the concentration field (Webster et al., 2003). The integral time scale of the ambient turbulence, T, is a characteristic time scale in a diffusion study, based on which the asymptotic properties of the turbulent diffusion can be defined (Taylor, 1921). In the present experiments, the integral time scale of the HIT ambient in the measurement plane is almost T = 7.2 s (calculated as $T = L_{HIT}/u_{rms,\,HIT}$ using data from Khorsandi et al. (2013)), which is almost twice as long as the measurement time. Therefore, a longer measurement time (than what was achieved in the present experiments) would be required to obtain the asymptotic properties of the turbulent diffusion.

Due to short measurement time and the decay of the turbulence intensity with distance from the RJA, the time-averaged concentration field is asymmetric, and thus, the whole surface area of the scalar field has been accounted for through a radial averaging. Using a radial averaging accounts for the decay of the turbulence intensity downstream of the RJA, which is less than 5% across the scalar patch (see Appendix B). In similar studies of homogeneous turbulence, a 25% and a 17% variation of the turbulence intensity in a turbulent channel flow and a double-sided RJA, respectively, have been assumed as approximately homogeneous turbulence (Amoura et al., 2010; Bellani and Variano, 2014). Also, the evolution of the patch size in the turbulent ambient follows the analytical solution for diffusion of a point-source plume in a stationary, homogeneous turbulence (details below). Therefore, the present analysis assumes an approximate homogeneity of the ambient turbulence across the scalar patch, and presents the average effect of the decaying turbulence intensity on the scalar patch.

The radially-averaged profiles of the mean concentration and the rms concentration in the turbulent ambient at t = 0.2, 1, 1.8, 2.6, 3.4 s are presented in Figs. 5.3 (*a*) and 5.3 (*b*), respectively. The mean concentration decays quickly in the turbulent ambient and the rms concentration increases. Initially, the rms concentration increases with time, which can be attributed to disturbances due to the outline of the jet crossing the laser sheet.

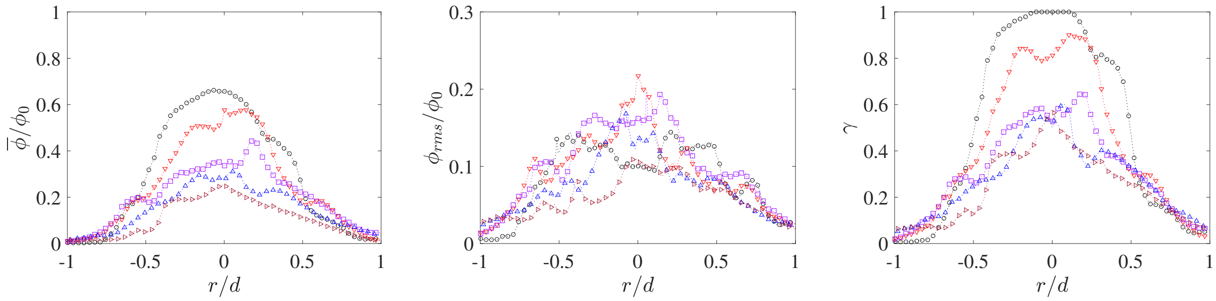

(a) **(b)** **(c)**

Figure 5.3: Radial profiles of the (*a*) mean concentration, (*b*) the rms concentration fluctuations, and (*c*) the intermittency of the scalar patch in the turbulent ambient. Symbols: ○ t = 0.2 s; ▽ t = 1 s; □ t = 1.8 s; △ t = 2.6 s; ▷ t = 3.4 s.

Beyond $t > 1.8$ s, the rms concentration decays, indicating that the scalar field is becoming more homogeneous while it is being diluted and mixed into the ambient fluid (implied by the decay of the mean concentration) (Webster et al., 2003). The rms concentrations are of the same order of magnitude as the corresponding mean values, suggesting that the flow is highly intermittent, as shown also by the intermittency profile (Fig. 5.3 (*c*)). In the turbulent ambient, the whole width of the scalar field is intermittent (i.e. $0 < \gamma < 1$), except very close to the centroid of the scalar patch at t = 0.2 s. It is noted that the time-averaged profiles in Fig. 5.3 are irregular due to shortness of the data series, and it is expected that they would become axisymmetric for long enough measurement times.

The PDFs and the CDFs of the centroidal concentration are presented in Figs. 5.4 (*a*) and 5.4 (*b*), respectively. The concentration PDFs do not resemble a Gaussian distribution, neither in a quiescent nor in the turbulent ambient. In the quiescent ambient, the PDFs are slim and almost unchanged for the studied time span due to the slow process of molecular diffusion. In the turbulent ambient, a wider range of concentrations is present at the centroid of the scalar field, moving towards progressively smaller concentrations with time. The CDFs show that the probability of very small concentrations increases with time, which is due to an increase in spatial variation of the scalar patch.

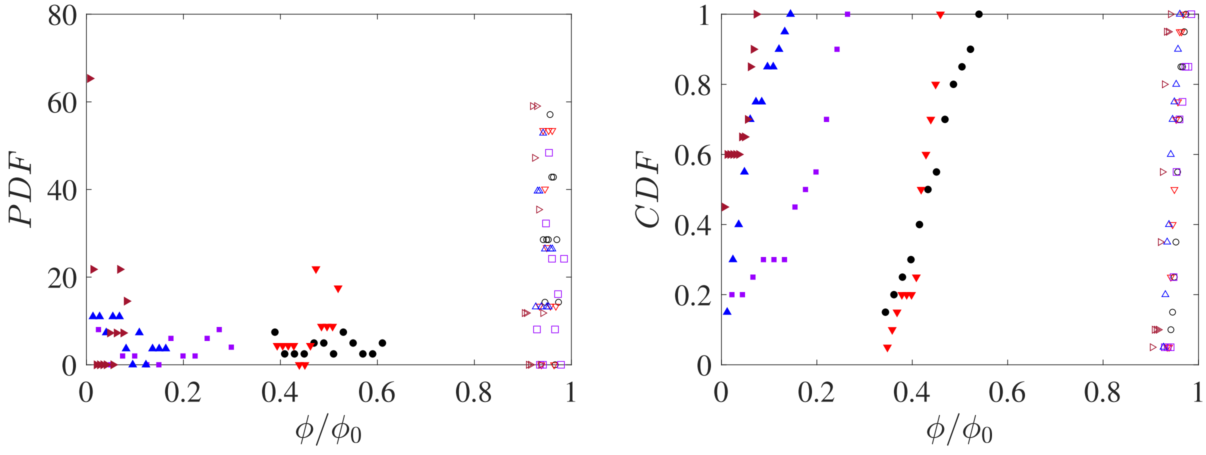

(a) **(b)**

Figure 5.4: (*a*) PDF and (*b*) CDF of the centroidal concentration in a quiescent ambient and in the turbulent ambient, respectively. Open symbols, quiescent ambient; filled symbols, turbulent ambient. Symbols: ○ t = 0.2 s; ▽ t = 1 s; □ t = 1.8 s; △ t = 2.6 s; ▷ t = 3.4 s.

Traditionally, the size of the scalar patch has been related to a turbulent diffusivity coefficient, $\mathcal{D}_t$, following the work of Taylor (1921). The turbulent diffusivity increases with the size of the scalar patch for patches smaller than the integral length scale of the turbulence, L (Taylor, 1921; Fischer et al., 1979; Webster et al., 2003). Theoretical arguments showed that the turbulent diffusivity scales linearly with the patch size (Okubo, 1972; Fischer et al., 1979), which was later supported by a number of experimental studies (e.g. for a meandering plume in a channel flow by Young et al. (2022)). Similar to the increase of the turbulent diffusivity with the patch size, $\mathcal{D}_t$ increases with time until the integral time scale of the turbulence, T, is reached. Beyond that, $\mathcal{D}_t$ approaches an asymptotic value that depends on the size of the energy containing eddies and the turbulence intensity of the ambient; i.e. $\mathcal{D}_t \approx u_{rms}L$ (Taylor, 1921; Fischer et al., 1979). In the present work, the measurement time is shorter than the turbulent time scale, and the asymptotic behavior of the scalar patch (and thus the turbulent diffusivity) is not reached.

The temporal evolution of the characteristic size of the scalar patch in the turbulent ambient is presented in Fig. 5.5. The size of the scalar patch, σ_ϕ, is proportional to the square root of the surface area of the scalar patch having concentrations above the thresh-

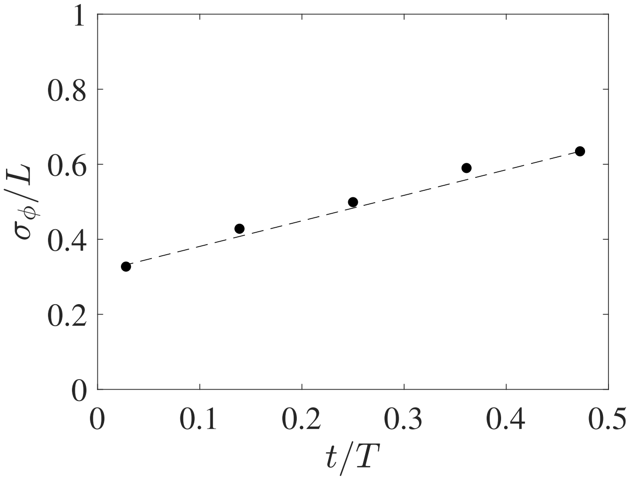

Figure 5.5: Temporal evolution of the size of the scalar patch, σ_ϕ, in the turbulent ambient, normalized by L, the integral length scale of the HIT ambient at y/M = 7.3.

old value of ϕ_t, i.e., $\sigma_\phi \approx (A_{\phi>\phi_t})^{1/2}$. The size of the scalar patch in the turbulent ambient increases almost linearly with time, suggesting that the turbulent diffusivity is increasing because the time is still smaller than the integral time scale. Assuming a linear relationship between σ_ϕ and $\mathcal{D}_t$ (Fischer et al., 1979) results in a linear growth of the turbulent diffusivity with time, which is consistent with Taylor's prediction for $\mathcal{D}_t \propto t$ in homogeneous turbulence for $t < T$ (eq. 5.3). Investigating the linearity between σ_ϕ and $\mathcal{D}_t$ for $t < T$, requires simultaneous measurements of the scalar field and the velocity field of the patch, and if so, it verifies the reliability of the assumption of "approximate" homogeneity of the present turbulent ambient across the field of view, despite the decay of the turbulence intensity. This could be a potential topic for a future work in this lab.

5.3.2 Discussion

The study of a momentumless patch of a passive scalar in the HIT ambient provides further insight of the characteristics of the axisymmetric turbulent jet in the HIT ambient beyond the jet break-up. For a turbulent jet in the HIT ambient, when the relative turbulence intensity between the ambient and the jet, ξ, exceeds 0.5, the mean scalar concentration approaches zero and the scalar field no longer grows in width; a condition that is called the jet break-up (Sahebjam et al., 2022). It was previously shown by Khorsandi et al. (2013) that the mean axial velocity profile of the jet approaches zero at the downstream distance where $\xi > 0.5$, indicating that the momentum-driven entrainment of the jet is negligible beyond the jet breakup. Therefore, turbulent diffusion by the ambient eddies becomes the only mechanism to disperse the scalar field. The statistics of the momentumless scalar field depends on the turbulent ambient properties, which is specific to particular flow geometries and experimental conditions and requires simultaneous measurement of the velocity and the concentration fields. The present experiments were initially intended to be carried out with simultaneous particle image velocimetry (PIV) and PLIF measurements, but this was not achieved as the equipment for PIV was not available.

The main challenge in a turbulent diffusion problem is to measure the concentration–velocity covariance or the turbulent scalar flux vector ($\overline{\phi' u_i}$). A turbulent diffusivity ($\mathcal{D}_{ij}$) can be defined analogous to molecular diffusivity ($\mathcal{D}$) relating the turbulent scalar flux to the gradient of the mean scalar, i.e. $-\overline{\phi' u_i} = \mathcal{D}_{ij}\frac{\partial \bar{\phi}}{\partial x_j}$. $\mathcal{D}_{ij}$ is a tensor, and its components can be obtained by simultaneous measurement of the local magnitude and directions of the mean concentration gradient and the turbulent scalar flux. A number of experimental studies, align the axis of the analysis with the local gradient of the phase-averaged concentration to cancel out the off-diagonal components of $\mathcal{D}_{ij}$ (Tavoularis and Corrsin, 1981, 1985; Karnik and Tavoularis, 1989; Young et al., 2022). Vanderwel and Tavoularis (2014a) calculated all components of the turbulent diffusivity tensor for a slender plume in a uniformly sheared flow, and Young et al. (2022) estimated the turbulent diffusivity coefficient of a meandering plume in a channel flow by measuring the transverse turbulent scalar flux and the scalar gradient. In the present setup, a planar PIV-PLIF measurement in the orthogonal plane of the jet would provide quantitative information of a 2×2 turbulent diffusivity tensor by measuring the transverse and spanwise velocity fluctuations, scalar concentration fluctuations, and radial scalar gradients.

When studying diffusion of a scalar patch, it is important to consider the state of growth of the scalar size with the local size of the turbulent eddies. For a scalar patch with a given size, turbulent eddies smaller than the patch continuously stretch and distort it, creating regions with large local concentration gradients that are smoothed out by molecular diffusion (the molecular diffusion flux is proportional to the concentration gradient). The eddies larger than the patch size, however, by only advecting the patch, do not contribute to mixing (Batchelor, 1952). In the turbulent diffusion tests, the initial size of the scalar patch is smaller than the turbulent length scale, and the scalar patch (that barely grows to $0.7L$ in the measurement time) is being simultaneously advected by the large eddies and mixed into the ambient by eddies smaller than its size. For the turbulent jet tests, the width of the scalar field remained constant once it reached the integral length scale of the turbulence by breakup of the jet. Therefore, it is expected that beyond breakup, the different-sized ambient eddies contribute only to diffusion and mixing of the scalar field (without advecting it), and that the turbulent diffusivity can be estimated by its asymptotic value that depends on large scale properties of the ambient turbulence.

5.4 Conclusion

The effect of an approximately homogeneous and isotropic turbulence with a negligible mean flow on the temporal evolution of a momentumless patch of a passive scalar is studied. The concentrations were measured by planar laser-induced fluorescence and the centroidally-averaged scalar statistics are compared to those in a quiescent ambient. The mean concentration decays quickly in the turbulent ambient and the rms concentration increases. The rms concentrations have values comparable to the mean concentration, which indicates high intermittency in the scalar field, causing a wide range of concentrations at the centroid of the scalar patch.

The size of the scalar patch in the turbulent ambient increases linearly with time for $t < T$, indicating that the turbulent diffusivity is increasing. It is expected that once the size of the scalar patch exceeds the integral length scale of the HIT ambient and once a time longer than the turbulent time scale is passed, turbulent diffusivity approaches a constant value that depends on the large scale properties of the turbulent ambient. To closely study these conjectures and to quantify the turbulent diffusivity tensor, simultaneous velocity-concentration measurement for a long enough time is required.

References

P. J. Roberts and D. R. Webster. *Turbulent Diffusion*. ASCE Press, Reston, Virginia, 2002.

C. Vanderwel and S. Tavoularis. Measurements of turbulent diffusion in uniformly sheared flow. *J. Fluid Mech.*, 754:488–514, 2014a.

G. I. Taylor. Diffusion by continuous movements. *Proc. London Math. Soc.*, 2(1):196–212, 1921.

M. S. Anand and S. B. Pope. Diffusion behind a line source in grid turbulence. *In Turbulent Shear Flows* 4, pages 46–61. Springer, Berlin, Heidelberg, 1985.

G. K. Batchelor. Diffusion in a field of homogeneous turbulence. i. Eulerian analysis. *Austral. J. Chem.*, 2(4):437–450, 1949.

S. Corrsin. Limitations of gradient transport models in random walks and in turbulence. *In Advances in geophysics*, volume 18, pages 25–60. Elsevier, 1975.

S. Tavoularis and S. Corrsin. Effects of shear on the turbulent diffusivity tensor. *Int. J. Heat Mass Transfer*, 28(1):265–276, 1985.

M. M. Rogers, N. N. Mansour, and W. C. Reynolds. An algebraic model for the turbulent flux of a passive scalar. *J. Fluid Mech.*, 203:77–101, 1989.

B. A. Younis, C. G. Speziale, and T. T. Clark. A rational model for the turbulent scalar fluxes. *Proc. R. Soc. Lond.*, 461(2054):575–594, 2005.

PG Saffman. On the effect of the molecular diffusivity in turbulent diffusion. *J. Fluid Mech.*, 8(2):273–283, 1960.

M. S. Uberoi and S. Corrsin. *Diffusion of Heat from a Line Source in Isotropic Turbulence*, volume 1142. National Advisory Committee for Aeronautics, 1952.

B. Sawford. Turbulent relative dispersion. *Ann. Rev. of Fluid Mech.*, 33(1):289–317, 2001.

P. C. Chatwin and P. J. Sullivan. The relative diffusion of a cloud of passive contaminant in incompressible turbulent flow. *J. Fluid Mech.*, 91(2):337–355, 1979.

S. Arya. *Air Pollution Meteorology and Dispersion*. Oxford University Press New York, 1999.

D. R. Webster, S. Rahman, and L. P. Dasi. Laser-induced fluorescence measurements of a turbulent plume. J. Eng. Mech., 129(10):1130–1137, 2003.

S. Rahman and D. R. Webster. The effect of bed roughness on scalar fluctuations in turbulent boundary layers. *Exp. Fluids*, 38(3):372–384, 2005.

M. Mohaghar, L. P. Dasi, and D. R. Webster. Scalar power spectra and turbulent scalar length scales of high-Schmidt-number passive scalar fields in turbulent boundary layers. *Phys. Rev. Fluids*, 5(8):084606, 2020.

E. G. Connor, M. K. McHugh, and J. P. Crimaldi. Quantification of airborne odor plumes using planar laser-induced fluorescence. *Exp. Fluids*, 59(9):1–11, 2018.

S. K. Halloran, A. S.Wexler, and W. D. Ristenpart. Turbulent dispersion via fan-generated flows. *Phys. Fluids*, 26(5):055114, 2014.

R. E. Britter, J. C. R. Hunt, G. L. Marsh, and W. H. Snyder. The effects of stable stratification on turbulent diffusion and the decay of grid turbulence. *J. Fluid Mech.*, 127:27–44, 1983.

R. A. Lavertu and L. Mydlarski. Scalar mixing from a concentrated source in turbulent channel flow. *J. Fluid Mech.*, 528:135–172, 2005.

J. Lepore and L. Mydlarski. Lateral dispersion from a concentrated line source in turbulent channel flow. *J. Fluid Mech.*, 678:417–450, 2011.

E. Germaine, L. Mydlarski, and L. Cortelezzi. Evolution of the scalar dissipation rate downstream of a concentrated line source in turbulent channel flow. *J. Fluid Mech.*, 749: 227–274, 2014.

G. I. Taylor. Statistical theory of turbulence. *Proc. of the Royal Soc. of London. Series A-Math. and Phys. Sciences*, 151(873):421–444, 1935.

A. A. Townsend. The diffusion behind a line source in homogeneous turbulence. *Proceedings of the Royal Society of London. Series A. Mathematical and Physical Sciences*, 224(1159): 487–512, 1954.

Z.Warhaft. The interference of thermal fields from line sources in grid turbulence. *J. Fluid Mech.*, 144:363–387, 1984.

H. Stapountzis, B. L. Sawford, J. C. R. Hunt, and R. E. Britter. Structure of the temperature field downwind of a line source in grid turbulence. *J. Fluid Mech.*, 165: 401–424, 1986.

J. Nedić, and S. Tavoularis. Measurements of passive scalar diffusion downstream of regular and fractal grids. J. Fluid Mech., 800:358–386, 2016.

S. Tavoularis and S. Corrsin. Experiments in nearly homogeneous turbulent shear flow with a uniform mean temperature gradient. part 1. *J. Fluid Mech.*, 104:311–347, 1981.

U. Karnik and S. Tavoularis. Measurements of heat diffusion from a continuous line source in a uniformly sheared turbulent flow. *J. Fluid Mech.*, 202:233–261, 1989.

J. E. Fackrell and A. G. Robins. Concentration fluctuations and fluxes in plumes from point sources in a turbulent boundary layer. *J. Fluid Mech.*, 117:1–26, 1982.

J. P. Crimaldi and J. R. Koseff. Structure of turbulent plumes from a momentum-less source in a smooth bed. *Environmental Fluid Mech.*, 6(6):573–592, 2006.

B. Khorsandi, S. Gaskin, and L. Mydlarski. Effect of background turbulence on an axisymmetric turbulent jet. *J. Fluid Mech.*, 736:250–286, 2013.

A. Perez-Alvarado, L. Mydlarski, and S. Gaskin. Effect of the driving algorithm on the turbulence generated by a random jet array. *Exp. Fluids*, 57:20, 2016.

R. Sahebjam, K. F. Kohan, and S. Gaskin. The dynamics of an axisymmetric turbulent jet in ambient turbulence interpreted from the passive scalar field statistics. *Phys. Fluids*, 34(1):015129, 2022.

E. A. Variano and E. A. Cowen. A random-jet-stirred turbulence tank. *J. Fluid Mech.*, 604: 1–32, 2004.

E. A. Variano, E. Bodenschatz, and E. A. Cowen. A random synthetic jet array driven turbulence tank. *Exp. Fluids*, 37:613–615, 2008.

A. Perez-Alvarado. *Effect of background turbulence on the scalar field of a turbulent jet*. PhD dissertation, McGill University, Department of Mechanical Engineering, 2016.

T. M. Lavertu. *Differential diffusion in a turbulent jet*. PhD thesis, McGill University Libraries, 2006.

P. O. Gendron, F. Avaltroni, and K. J. Wilkinson. Diffusion coefficients of several rhodamine derivatives as determined by pulsed field gradient–nuclear magnetic resonance and fluorescence correlation spectroscopy. *J. Fluorescence*, 18(6):1093–1101, 2008.

Z. Amoura, V. Roig, F. Risso, and A. M. Billet. Attenuation of the wake of a sphere in an intense incident turbulence with large length scales. *Phys. Fluids*, 22:055105, 2010.

G. Bellani and E. A. Variano. Homogeneity and isotropy in a laboratory turbulent flow. *Exp. Fluids*, 55(1):1–12, 2014.

H. B. Fischer, J. E. List, C. R. Koh, J. Imberger, and N. H. Brooks. *Mixing in Inland and Coastal Waters*. Academic press, 1979.

A. Okubo. Some speculations on oceanic diffusion diagrams. Technical report, Johns Hopkins Univ., Baltimore, Md. Chesapeake Bay Inst., 1972.

D. L. Young, D. R. Webster, and A. I. Larsson. Structure and mixing of a meandering turbulent chemical plume: turbulent mixing and eddy diffusivity. *Exp. Fluids*, 63(1): 1–11, 2022.

Chapter 6

Conclusion

This chapter provides a summary of the research and the conclusions drawn therefrom, followed by a summary of the original contributions of the research and recommendations for extending the present investigations.

6.1 Summary

The present study investigates the statistics of the passive scalar field of an axisymmetric turbulent jet and of a momentumless scalar patch in approximately homogeneous isotropic turbulence (HIT) with negligible mean flow. The turbulent ambient was generated by a random jet array, which produces an ambient turbulence close to homogeneous along the jet axis (k_{HIT} = 4.4 $\mathrm{cm}^2\mathrm{s}^2$ at y/M = 7.3) and decaying at a small rate across the jet cross-section (approximately 9% over the largest jet half-width at x/d = 60, Re = 10600). The scalar concentrations were measured in orthogonal cross-sections of the jets with Re = 5800 and 10600 between x/d = 20 to 60 using the planar laser-induced fluorescence technique. The turbulent jet experiments were carried out to study the jet entrainment and mixing in the HIT ambient and infer the jet structure to determine any changes from that in the quiescent ambient. Subsequently, the diffusion of a momentumless scalar patch was investigated qualitatively to assess the behavior of the jet in the HIT ambient after jet breakup, when scalar dispersion is only due to turbulent diffusion.

Analyses of the evolution of the scalar field in the jet were carried out following the meandering path of the jet and the scalar patch in the HIT ambient, that is they were conditioned on the centroid of the cross-section, to remove the effect of the larger ambient eddies, which advect the jet laterally, and investigate the effect of the smaller ambient eddies, which modify the jet entrainment and structure. The centroidally-averaged statistics of the passive scalar field of the jet were compared to the (commonly used) Eulerian statistics of the jet in the HIT ambient (which includes both the lateral advection of the larger eddies and the effect of the smaller eddies of the ambient turbulence) and to those of a jet in a quiescent ambient. Similarly, the centroidally-averaged statistics of the scalar patch were compared to those of the scalar patch in a quiescent ambient and to the statistics of the turbulent jet beyond breakup.

The behavior of the jet in the HIT ambient depends on the relative length scale, $\mathcal{L}$, and the relative turbulence intensity, ξ, between the ambient and the jet, which decreases and increases along the jet axis, respectively. The centroidal averaging removes the effect of the relative length scale, allowing the effect of the turbulence intensity of the background on the jet structure and mixing to be isolated. The centerline concentration and the concentration half-width of the jet followed a self-similar power-law behavior until ξ reached the critical value of 0.5, beyond which the structure of the jet was destroyed by the HIT ambient.

The mean concentration profiles of the jet in the HIT ambient were Gaussian both for the centroidal and for the Eulerian averaging. The centroidally averaged profiles collapsed onto a single curve in the power-law region, when normalized by corresponding centroidal centerline concentrations. The mean centerline concentration decayed more rapidly than that in the quiescent ambient resulting in lower concentrations in the jet. In the power-law region for both jet Reynolds numbers, the mean centerline concentration decayed as $x^{-1.1}$ for the centroidal averaging, which is close to the x^{-1} decay in a quiescent ambient, while, for the Eulerian averaging, the mean concentration decay was Reynolds number dependent and greater than that for the centroidal averaging (due to the inclusion of the lateral advection of the jet by the turbulent ambient eddies).

The jet was wider in the HIT ambient and the half-width of the scalar field increased more rapidly than the linear growth of the jet in a quiescent ambient. The half-width of the centroidally-averaged concentration profiles evolved as $x^{1.1}$ for both jet Reynolds numbers, whereas the Eulerian averaging showed higher exponents for the concentration half-width growth in the HIT ambient, which increased with decreasing Reynolds number. A higher concentration half-width of the centroidally averaged profile in the HIT ambient can be attributed to enhanced radial transport of the scalar by the turbulent ambient eddies.

The first-order statistics of the scalar field were found to be self-preserving and self-similar in the power-law region of the jet in the HIT ambient. This is shown by the product of the decay of the centroidally averaged concentration and the growth rate of the concentration half-width scaling to a constant ($x^{-1.1} \times x^{1.1} = x^0$). This is supported by the collapse of the centroidally averaged mean concentration profiles onto a single (Gaussian) curve. The Eulerian statistics of the passive scalar did not show self-similarity.

The time-averaged entrainment of the jet in the HIT ambient is reduced in the power-law region, and it ceases beyond jet breakup. The reduced entrainment is implied by a lower mass flow rate of the jet in the HIT ambient, as well as lower mean momentum flux and lower mean scalar flux of the jet compared to those in a quiescent ambient. After the jet breaks up, the centroidal half-width of the concentration stops growing, indicating that the integral volume flux and the momentum volume flux are no longer increasing with downstream distance.

The rms concentrations of the jet increased in the HIT ambient due to entrainment of background fluctuations. The centroidally-averaged rms profiles were initially double-peaked for the Re = 10600 jet in the HIT ambient, indicating a relatively strong shear layer between the jet and the ambient. The profiles became single-peaked with increasing modulation of the jet structure by small ambient eddies (by x/d = 60, where ξ = 0.43). For the Re = 5800 jet, the centroidally-averaged rms profiles were initially two-peaked showing the modified (but still preserved) shear layer, and became single-peaked beyond breakup, for $\xi > 0.5$. The Eulerian rms profiles obscured the jet structure by inclusion of the effect of the jet meandering, showing higher magnitudes compared to the centroidally-averaged profiles, and being single-peaked, except close to the jet exit for the high Re number jet, where the relative turbulence intensity was low and the jet structure was well preserved.

The intermittency profile of the jet increases in width in the turbulent ambient due to a wider width of the jet. The core of the jet is preserved in the centroidally-averaged profiles (i.e. γ = 1) to just before breakup, whereas the intermittency of the Eulerian profiles is greater, indicating the presence of ambient fluid, even at the centerline, close to the jet exit (due to inclusion of the fluctuations due to the meandering path).

The probability density function (PDF) and the cumulative density function (CDF) of the centerline centroidal concentrations show a wider range of concentrations at the centerline of the jet compared to those of the jet in a quiescent ambient. The PDFs are non-Gaussian and skewed towards lower concentrations. The Eulerian PDFs are non-Gaussian and approach an exponential distribution beyond breakup, with high probability of zero concentrations due to meandering of the jet path resulting in ambient fluid existing at the centerline. Wider centroidal PDFs implied a lower mixing within the jet in the HIT ambient compared to that in a quiescent ambient. The centroidal CDFs show lower concentrations in the self-similar region and high likelihood of zero concentration after jet breakup.

Based on the centroidally-averaged statistics of the first-order properties of the scalar field of the jet, a two-region model for the jet structure in the HIT ambient is proposed. In the first region, following the developing region of the jet, the jet is self-similar, and the centerline concentration decay and the concentration half-width growth follow power-law behavior despite being perturbed by the ambient turbulence. Compared to that in a quiescent ambient, the mean concentration decays more rapidly, the width growth is faster, and the entrainment of the jet is reduced. The second region starts as the relative turbulence intensity between the ambient and the jet increases to 0.5, where the HIT ambient destroys the jet structure. In the second region, the jet no longer follows power-law behavior, the mean concentration approaches zero, the concentration half-width stops growing, and the time-averaged entrainment into the jet ceases.

Beyond breakup, turbulent diffusion by the ambient eddies is the only mechanism to transport the (momentumless) scalar field. The study of the diffusion of a momentumless patch of a passive scalar in the same turbulent ambient shows a rapid decay of the mean concentration and large rms concentration within the scalar field compared to that in a quiescent ambient, where the scalar field is subject to the slow process of molecular diffusion. The rms concentrations are of the same order as the mean concentrations, indicating a highly intermittent flow.

The width of the scalar patch increases linearly with time, and it is expected to grow at a slower rate once the size of the scalar patch approaches the integral length scale of the turbulence, and a time longer than the integral time scale has passed. Once the size of the scalar patch reaches the integral length scale, all eddy sizes contribute to diffusion of the scalar and mixing it into the ambient, without advecting it. At the limit, the turbulent diffusivity approaches an asymptotic value that depends on the integral length scale and the turbulence intensity of the ambient.

6.2 Recommendations for future work

It is recommended to analyze the jet in the HIT ambient for a wider range of relative turbulence intensity ratios, ξ, to verify the validity of the proposed two-region model. Lower relative turbulence intensities would allow for the determination of the extent of the developing region of the jet, and higher relative turbulence intensity ratios would provide information about the jet beyond its breakup, and that if the concentration half-width continues to remain constant at a size comparable to the integral length scale. Also, more moderate values for ξ between 0.16 and 0.5, would verify the authenticity of the proposed model in the self-similar region of the jet. A range of turbulence intensity ratios can be obtained either by changing the Reynolds number of the jet or by having a different distance between the RJA plane and the jet, as the RJA turbulence decays in a direction perpendicular to the plane of the RJA. Note that a minimum distance from the RJA is about y/M = 5 to ensure that the jets have merged and the ambient turbulent is approximately homogeneous.

Velocity measurements of the jet using PIV would provide high spatial resolution profiles (than that achieved from the the point measurements), making it possible to carry out a centroidal analysis for the velocity field of the jet. A knowledge of the velocity field of the jet will also contribute to the understanding of the entrainment into the jet. Also, PLIF velocimetry could be carried out to measure relatively small velocities of the jet in the radial direction (e.g. the entrainment velocity).

Simultaneous measurements of the velocity and the concentration fields (using 2D-3D PIV/PLIF) will be very useful for a better understanding of the mechanism of the entrainment and mixing in a jet emitted into the turbulent ambient. They will allow for the quantification of the mean and the turbulent components of the scalar flux of the jet, which is used to determine the turbulent diffusivity tensor of the jet. Also, it would be possible to measure the radial and the axial transport of the scalar and to study the conservation of mass using simultaneous PIV/PLIF measurements.

Appendix A

A note on Chapter 4

This appendix addresses the minor points that were not included in the main body of Ch. 4 for the purpose of brevity of paper publication.

The JPDFs of the position of the jet centroid in the turbulent ambient (Fig. 4.3) showed a greater displacement of the jet centroid in the turbulent ambient compared to the full extent of the jet in a quiescent ambient, i.e. $-0.2 < r/x < 0.2$. This is shown in Fig. A.1 for x/d = 20, 40 and 60 of the Re = 10600 and 5800 jets as examples. The decreasing standard deviation of the jet centroid for larger axial distances (Fig. 4.4) suggests that the jet is less deviated from its mean centroid position in the downstream distance. Beyond breakup, the JPDFs become more circular, indicating that the centroid of the jet is displaced more randomly, which can be attributed to lower effect of the length scale of the single-sided RJA turbulence on the motion of the jet.

The radial extents of the jet (i.e. y and z) are normalized by the axial distance, x, due to self-similarity of the jet and that its half-width scales with x in the quiescent ambient. It is noted that the self-similarity profiles in Fig. 4.14 reflected the effect of scaling of the jet half-width with $x^{1.1}$ in the turbulent ambient.

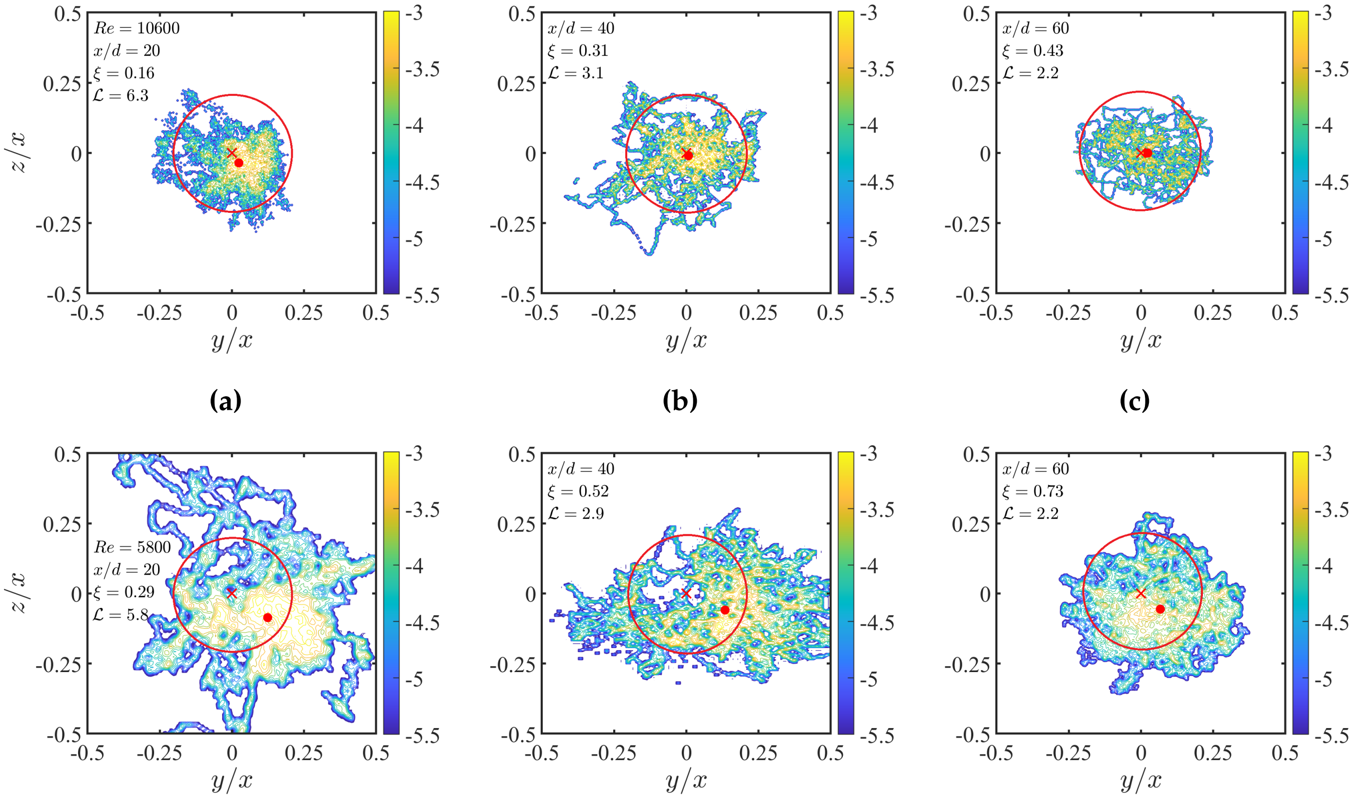

(a) **(b)** **(c)**

(d) **(e)** **(f)**

Figure A.1: Comparison between the extent of the jet in the quiescent ambient (i.e. red circle) and the displacement of the position of the jet centroid in the turbulent ambient. (*a*) x/d = 20, (*b*) x/d = 40, and (*c*) x/d = 60 for Re = 10600 jet, and (*d*) x/d = 20, (*e*) x/d = 40, and (*f*) x/d = 60 for Re = 5800 jet, respectively.

Appendix B

Homogeneity of the turbulent ambient

The present experimental setup used a single-RJA plane to generate an approximately homogeneous isotropic turbulence with negligible mean flow downstream of the RJA plane, where the flows of the individual jets merge. Due to the symmetry of the RJA apparatus, the turbulence was statistically homogeneous in the $x - z$ planes (parallel to the RJA) at sufficiently large distances from the RJA jets ($y/\mathrm{M} > 5$) (Khorsandi et al., 2013; Perez-Alvarado et al., 2016). However, the turbulence intensity of the turbulent ambient, defined as $u_\tau = [1/3(u^2_{rms,HIT} + v^2_{rms,HIT} + w^2_{rms,HIT})]^{1/2}$, decays exponentially in the downstream direction of the RJA plane (Khorsandi et al., 2013; Perez-Alvarado et al., 2016). In the turbulent jet experiments (Ch. 4), the analyses were performed on equi-distant profiles (from the RJA plane), passing through the instantaneous centroid of the jet, which were subject to a small range of levels of turbulence intensity centered on the value at geometric centreline due to the jet meandering. In the turbulent diffusion tests (Ch. 5), the analyses were carried out along all the radial profiles passing through the instantaneous centroid of the scalar patch, thus, experiencing a small range of turbulence intensities centered on the level at the geometric centreline. The lateral decay of the homogeneity of the RJA-generated turbulence in the regions of interest is studied.

The downstream decay of u_τ relative to the RJA plane is plotted in Fig. B.1 using velocity data at y/M = 5.5, 6.7, 7.3, 9.3 from Khorsandi et al. (2013) and Perez-Alvarado et al.

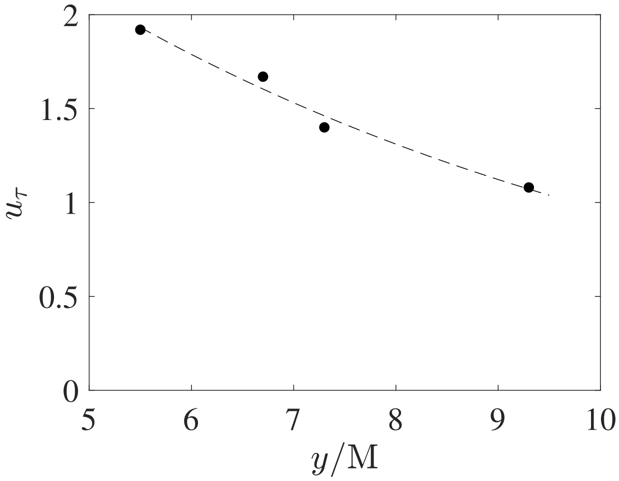

Figure B.1: Decay of the ambient turbulence intensity downstream of the RJA plane.

(2016). An exponential curve is fitted to the data to allow for a rough estimation of the decay of the ambient turbulence intensity. For the jet in the HIT ambient, the greatest width of the jet is almost equal to the the integral length scale of the turbulent ambient (Fig. 4.10), which corresponds approximately to a lateral width of 6.9 $< y/\mathrm{M} <$ 7.6 relative to the geometric centerline (at y/M = 7.3). The decay of the turbulence intensity between 6.9 $< y/\mathrm{M} <$ 7.6 is almost 10%. For the turbulent diffusion tests, the width of the scalar patch grows to $0.7L$, occupying a lateral extent of 7.1 $< y/\mathrm{M} <$ 7.5, where the turbulence intensity decays approximately by 6%. It is noted that the decay of the turbulence intensity follows a power law, resulting in a greater change in turbulence intensity over the half of the image closer to the RJA plane. Therefore, the average over all jet centroid positions or over all radii experiences slightly higher turbulence intensity levels than that if the jet/scalar patch were only exposed to the turbulence intensity of the geometric centerline. Since the jet/scalar patch meander randomly and the centroid positions are comprised of an almost equal number of samples for which the turbulence intensity is higher than that at the geometric centerline as those that are lower, the net effect is approximately that of the turbulence intensity at the geometric centerline. Therefore, the present analysis assumes an "approximate" homogeneity of the turbulent ambient across the width of the jet/scalar patch, and the turbulence intensity level corresponding to y/M

= 7.3 provides an average effect of the turbulence intensity level to which the jet/scalar patch are subject to. In similar studies of homogeneous turbulence, Amoura et al. (2010) and Bellani and Variano (2014) assumed a 25% and a 17% variation of the turbulence intensity (across shorter lateral distances than in ours) in a turbulent channel flow and a double-sided RJA, respectively, as approximately homogeneous turbulence.

References

A. Agrawal and A. K. Prasad. Evolution of a turbulent jet subjected to volumetric heating. *J. Fluid Mech.*, 511:95–123, 2004.

Z. Amoura, V. Roig, F. Risso, and A. M. Billet. Attenuation of the wake of a sphere in an intense incident turbulence with large length scales. *Phys. Fluids*, 22:055105, 2010.

M. S. Anand and S. B. Pope. Diffusion behind a line source in grid turbulence. In *Turbulent Shear Flows 4*, pages 46–61. Springer, Berlin, Heidelberg, 1985.

C. Arcoumanis, J. J. McGuirk, and J. M. Palma. On the use of fluorescent dyes for concentration measurements in water flows. *Exp. Fluids*, 10(2):177–180, 1990.

S. Arya. *Air Pollution Meteorology and Dispersion*. Oxford University Press New York, 1999.

S. Aumaitre, S. Fauve, and J. F. Pinton. Large scale correlations for energy injection mechanisms in swirling turbulent flows. *Eur. Phys. J.*, 16(3):563–567, 2000.

P. Bagchi and S. Balachandar. Response of the wake of an isolated particle to an isotropic turbulent flow. *J. Fluid Mech.*, 518:95, 2004.

P. Baj, P. J. K. Bruce, and O. R. H. Buxton. On a plif quantification methodology in a nonlinear dye response regime. *Exp. Fluids*, 57(6):1–19, 2016.

G. Balamurugan, A. Rodda, J. Philip, and A. C. Mandal. Characteristics of the turbulent/non-turbulent interface in a spatially evolving turbulent mixing layer. *J. Fluid Mech.*, 894:A4, 2020.

B. M. Bara, D. J. Wilson, and B. W. Zelt. Concentration fluctuation profiles from a water channel simulation of a ground-level release. *Atmospheric Environment. Part A. General Topics*, 26(6):1053–1062, 1992.

G. K. Batchelor. Diffusion in a field of homogeneous turbulence. i. eulerian analysis. *Austral. J. Chem.*, 2(4):437–450, 1949.

G. K. Batchelor. Diffusion in a field of homogeneous turbulence: Ii. the relative motion of particles. In *Mathematical Proceedings of the Cambridge Philosophical Society*, volume 48, pages 345–362. Cambridge University Press, 1952.

G. K. Batchelor. Small-scale variation of convected quantities like temperature in turbulent fluid part 1. general discussion and the case of small conductivity. *J. Fluid Mech.*, 5 (1):113–133, 1959.

H. A. Becker, H. C. Hottel, and G. C. Williams. The nozzle fluid concentration field of the round turbulent jet. *J. Fluid Mech.*, 30:285–303, 1967.

G. Bellani and E. A. Variano. Homogeneity and isotropy in a laboratory turbulent flow. *Exp. Fluids*, 55(1):1–12, 2014.

T. Berk and F. Coletti. Dynamics of small heavy particles in homogeneous turbulence: a lagrangian experimental study. *J. Fluid Mech.*, 917, 2021.

G. S. Bhat and R. Narasimha. A volumetrically heated jet: large-eddy structure and entrainment characteristics. *J. Fluid Mech.*, 325:303–330, 1996.

A. D. Birch, D. R. Brown, M. G. Dodson, and J. R. Thomas. The turbulent concentration field of a methane jet. *J. Fluid Mech.*, 88(3):431–449, 1978.

M. Birouk, B. Sarh, and I. Gökalp. An attempt to realize experimental isotropic turbulence at low reynolds number. *Flow Turb. Combust.*, 70(1):325–348, 2003.

D. K. Bisset, J. C. R. Hunt, and M. M. Rogers. The turbulent/non-turbulent interface bounding a far wake. *J. Fluid Mech.*, 451:383–410, 2002.

D. B. Blum, S. B. Kunwar, J. Johnson, and G. A. Voth. Effects of non-universal large scales on conditional structure functions in turbulence. *Phys. Fluids*, 22(1):015107, 2010.

E. Bodenschatz, G. P. Bewley, H. Nobach, M. Sinhuber, and H. Xu. Variable density turbulence tunnel facility. *Rev. Sci. Inst.*, 85(9):093908, 2014.

G. Borrell and J. Jiménez. Properties of the turbulent/non-turbulent interface in boundary layers. *J. Fluid Mech.*, 801:554–596, 2016.

R. Breidenthal. Structure in turbulent mixing layers and wakes using a chemical reaction. *J. Fluid Mech.*, 109:1–24, 1981.

R. E. Britter, J. C. R. Hunt, G. L. Marsh, and W. H. Snyder. The effects of stable stratification on turbulent diffusion and the decay of grid turbulence. *J. Fluid Mech.*, 127:27–44, 1983.

G. L. Brown and A. Roshko. On density effects and large structure in turbulent mixing layers. *J. Fluid Mech.*, 64(4):775–816, 1974.

B. H. Brumley and G. H. Jirka. Near-surface turbulence in a grid-stirred tank. *J. Fluid Mech.*, 183:235–263, 1987.

H. C. Burridge, D. A. Parker, E.S. Kruger, J. Partridge, and P. Linden. Conditional sampling of a high péclet number turbulent plume and the implications for entrainment. *J. Fluid Mech.*, 823:26–56, 2017.

O. Cadot, S. Douady, and Y. Couder. Characterization of the low-pressure filaments in a three-dimensional turbulent shear flow. *Phys. Fluids*, 7(3):630–646, 1995.

A. Carter, D.and Petersen, O. Amili, and F. Coletti. Generating and controlling homogeneous air turbulence using random jet arrays. *Exp. Fluids*, 57:1–15, 2016.

D. W. Carter and F. Coletti. Scale-to-scale anisotropy in homogeneous turbulence. *J. Fluid Mech.*, 827:250–284, 2017.

H. J. Catrakis and P. E. Dimotakis. Mixing in turbulent jets: scalar measures and isosurface geometry. *J. Fluid Mech.*, 317:369–406, 1996.

A. Cazaubiel, J.-B. Gorce, J.-C. Bacri, M. Berhanu, C. Laroche, and E. Falcon. Three-dimensional turbulence generated homogeneously by magnetic particles. *Phys. Rev. Fluids*, 6(11):L112601, 2021.

K. Chang, G. P. Bewley, and E. Bodenschatz. Experimental study of the influence of anisotropy on the inertial scales of turbulence. *J. Fluid Mechanics*, 692:464–481, 2012.

P. C. Chatwin and P. J. Sullivan. The relative diffusion of a cloud of passive contaminant in incompressible turbulent flow. *J. Fluid Mech.*, 91(2):337–355, 1979.

K. Chauhan, J. Philip, and I. Marusic. Scaling of the turbulent/non-turbulent interface in boundary layers. *J. Fluid Mech.*, 751:298–328, 2014.

R. Chevray and N. K. Tutu. Intermittency and preferential transport of heat in a round jet. *J. Fluid Mech.*, 88:133–160, 1978.

C. Y. Ching, H. J. S. Fernando, and A. Robles. Breakdown of line plumes in turbulent environments. *J. Geophys. Res.: Oceans*, 100:4707–4713, 1995.

L. P. Chua and R. A. Antonia. The turbulent interaction region of a circular jet. *Int. comm. heat mass transfer*, 13(5):545–558, 1986.

L. P. Chua and R. A. Antonia. Turbulent prandtl number in a circular jet. *Int. J. Heat Mass Trans.*, 33(2):331–339, 1990.

G. Comte-Bellot and S. Corrsin. The use of a contraction to improve the isotropy of grid-generated turbulence. *J. Fluid Mech.*, 25(4):657–682, 1966.

E. G. Connor, M. K. McHugh, and J. P. Crimaldi. Quantification of airborne odor plumes using planar laser-induced fluorescence. *Exp. Fluids*, 59(9):1–11, 2018.

J Coppeta and C Rogers. Dual emission laser induced fluorescence for direct planar scalar behavior measurements. *Exp. Fluids*, 25(1):1–15, 1998.

S. Corrsin. On the spectrum of isotropic temperature fluctuations in an isotropic turbulence. *J. App. Phys.*, 22(4):469–473, 1951.

S. Corrsin. Limitations of gradient transport models in random walks and in turbulence. In *Advances in geophysics*, volume 18, pages 25–60. Elsevier, 1975.

S. Corrsin and A. L. Kistler. Free-stream boundaries of turbulent flows. Technical report, JOHNS HOPKINS UNIV BALTIMORE MD, 1955.

S. Corrsin and M. S. Uberoi. Further experiments on the flow and heat transfer in a heated turbulent air jet. *National Advisory Committee for Aeronautics, NACA*, 1950.

E. A. Cowen, K. A. Chang, and Q. Liao. A single-camera coupled PTV-LIF technique. *Exp. Thermal and Fluid Sci.*, 22:213–229, 2000.

J. P Crimaldi. The effect of photobleaching and velocity fluctuations on single-point lif measurements. *Exp. Fluids*, 23(4):325–330, 1997.

J. P. Crimaldi. Planar laser induced fluorescence in aqueous flows. *Exp. Fluids*, 44(6): 851–863, 2008.

J. P. Crimaldi and J. R. Koseff. Structure of turbulent plumes from a momentum-less source in a smooth bed. *Environmental Fluid Mech.*, 6(6):573–592, 2006.

A. J. Cuthbertson, D. Malcangio, P. A. Davies, and M. Mossa. The influence of a localised region of turbulence on the structural development of a turbulent, round, buoyant jet. *Fluid Dyn. Res.*, 38:683–698, 2006.

C. B. da Silva and R. R. Taveira. The thickness of the turbulent/nonturbulent interface is equal to the radius of the large vorticity structures near the edge of the shear layer. *Phys. Fluids*, 22(12):121702, 2010.

C. B. da Silva, J. C. R. Hunt, I. Eames, and J. Westerweel. Interfacial layers between regions of different turbulence intensity. *Annu. Rev. Fluid Mech.*, 46:567–590, 2014.

W. J. A. Dahm and P. E. Dimotakis. Measurements of entrainment and mixing in turbulent jets. *AIAA J.*, 25(9):1216–1223, 1987.

W. J. A. Dahm and P. E. Dimotakis. Mixing at large schmidt number in the self-similar far field of turbulent jets. *J. Fluid Mech.*, 217:299–330, 1990.

J. De Jong, L. Cao, S. H. Woodward, J. P. L. C. Salazar, L. R. Collins, and H. Meng. Dissipation rate estimation from piv in zero-mean isotropic turbulence. *Exp. Fluids*, 46(3): 499–515, 2009.

I. P. D. De Silva and H. J. S. Fernando. Oscillating grids as a source of nearly isotropic turbulence. *Phys. Fluids*, 6:2455–2464, 1994.

C. F. Dewey Jr. Qualitative and quantitative flow field visualization utilizing laser-induced fluorescence. *In AGARD Appl. of Non-Intrusive Instr. in Fluid Flow Res. 7 p (SEE N77-11221 02-31*, 1976.

P. E. Dimotakis. The mixing transition in turbulent flows. *J. Fluid Mech.*, 409:69–98, 2000.

P. E. Dimotakis. Turbulent mixing. *Ann. Rev. Fluid Mech.*, 37:329–356, 2005.

E. Dogan, R. E. Hanson, and B. Ganapathisubramani. Interactions of large-scale free-stream turbulence with turbulent boundary layers. *J. Fluid Mech.*, 802:79–107, 2016.

S. Douady, Y. Couder, and M. E. Brachet. Direct observation of the intermittency of intense vorticity filaments in turbulence. *Phys. Rev. Lett.*, 67(8):983, 1991.

D. R. Dowling and P. E. Dimotakis. Similarity of the concentration field of gas-phase turbulent jets. *J. Fluid Mech.*, 218:109–141, 1990.

PA Durbin. A stochastic model of two-particle dispersion and concentration fluctuations in homogeneous turbulence. *J. Fluid Mech.*, 100(2):279–302, 1980.

M. J. Dyer and D. R. Crosley. Two-dimensional imaging of oh laser-induced fluorescence in a flame. *Optics letters*, 7(8):382–384, 1982.

I. Eames, P. B. Johnson, V. Roig, and F. Risso. Effect of turbulence on the downstream velocity deficit of a rigid sphere. *Phys. Fluids*, 23(9):095103, 2011a.

I. Eames, C. Jonsson, and P. B. Johnson. The growth of a cylinder wake in turbulent flow. *J. Turbulence*, 12:N39, 2011b.

C. Eckart. An analysis of the stirring and mixing processes in incompressible fluids. *J. Mar. Res.*, pages 265–275, 1948.

Ö. Ertunç, N. Özyilmaz, H. Lienhart, F. Durst, and K. Beronov. Homogeneity of turbulence generated by static-grid structures. *J. Fluid Mech.*, 654:473–500, 2010.

L. B. Esteban, J. S. Shrimpton, and B. Ganapathisubramani. Laboratory experiments on the temporal decay of homogeneous anisotropic turbulence. *J. Fluid Mech.*, 862:99–127, 2019.

J. E. Fackrell and A. G. Robins. Concentration fluctuations and fluxes in plumes from point sources in a turbulent boundary layer. *J. Fluid Mech.*, 117:1–26, 1982.

T. Fallon and C. B. Rogers. Turbulence-induced preferential concentration of solid particles in microgravity conditions. *Exp. Fluids*, 33(2):233–241, 2002.

S. Fauve, C. Laroche, and B. Castaing. Pressure fluctuations in swirling turbulent flows. *Journal de physique II*, 3(3):271–278, 1993.

H. J. S. Fernando and I. P. D. De Silva. Note on secondary flows in oscillating-grid, mixing-box experiments. *Phys. Fluids A: Fluid Dyn.*, 5(7):1849–1851, 1993.

A. J. Ferrier, D. R. Funk, and P. J. W. Roberts. Application of optical techniques to the study of plumes in stratified fluids. *Dynamics of Atmospheres and Oceans*, 20(1-2):155–183, 1993.

H. B. Fischer, J. E. List, C. R. Koh, J. Imberger, and N. H. Brooks. *Mixing in Inland and Coastal Waters*. Academic press, 1979.

P. D. Friedman and J. Katz. Mean rise rate of droplets in isotropic turbulence. *Phys. Fluids*, 14(9):3059–3073, 2002.

C. A. Friehe, C. W. van Atta, and C. H. Gibson. Jet turbulence: dissipation rate measurements and correlations. *NATO Advisory Group for Aerospace Research and Development*, 1971.

C. Fukushima, L. Aanen, and J. Westerweel. Investigation of the mixing process in an axisymmetric turbulent jet using PIV and LIF. *In laser techniques for fluid mechanics*, pages 339–356, 2002.

S. Gaskin, M. McKernan, and F. Xue. The effect of background turbulence on jet entrainment: an experimental study of a plane jet in a shallow coflow. *J. Hydraulic Res.*, 42: 533–542, 2004.

S. Gaskin, A. Perez-Alvarado, and L. Mydlarski. Impact of relative turbulence scales on the effect of background turbulence on jet flows. *4th International Symposium of Shallow Flows*, 2017.

P. O. Gendron, F. Avaltroni, and K. J. Wilkinson. Diffusion coefficients of several rhodamine derivatives as determined by pulsed field gradient–nuclear magnetic resonance and fluorescence correlation spectroscopy. *J. Fluorescence*, 18(6):1093–1101, 2008.

E. Germaine, L. Mydlarski, and L. Cortelezzi. Evolution of the scalar dissipation rate downstream of a concentrated line source in turbulent channel flow. *J. Fluid Mech.*, 749: 227–274, 2014.

C. Goepfert, J. Marié, D. Chareyron, and M. Lance. Characterization of a system generating a homogeneous isotropic turbulence field by free synthetic jets. *Exp. Fluids*, 48(5): 809–822, 2010.

G. G. Guilbault. *Practical Fluorescence: Theory, Methods, and Techniques*. Marcel Dekker, 1973.

Y. Guo, D. Malcangio, P. A. Davies, and H. J. Fernando. A laboratory investigation into the influence of a localized region of turbulence on the evolution of a round turbulent jet. *Fluid Dyn. Res.*, 36:78–89, 2005.

S. K. Halloran, A. S. Wexler, and W. D. Ristenpart. Turbulent dispersion via fan-generated flows. *Phys. Fluids*, 26(5):055114, 2014.

P. E. Hancock and P. Bradshaw. Turbulence structure of a boundary layer beneath a turbulent free stream. *J. Fluid Mech.*, 205:45–76, 1989.

M. Holzner and B. Lüthi. Laminar superlayer at the turbulence boundary. *Phys. Rev. Lett.*, 106:134503, 2011.

M. Holzner, B. Lüthi, A. Tsinober, and W. Kinzelbach. Acceleration, pressure and related quantities in the proximity of the turbulent/non-turbulent interface. *J. Fluid Mech.*, 639: 153–165, 2009.

M. S. Hossain and W. Rodi. A turbulence model for buoyant flows and its application to vertical buoyant jets. In *Turbulent Buoyant Jets and Plumes*, pages 121–178. Elsevier, 1982.

J. C. R. Hunt. Atmospheric jets and plumes. *Recent Res. Adv. Fluid Mech. Turb. Jets and Plumes*, 255:309–334, 1994.

A. K. M. F. Hussain and A. R. Clark. On the coherent structure of the axisymmetric mixing layer: a flow-visualization study. *J. Fluid Mech.*, 104:263–294, 1981.

H. J. Hussein, S. P. Capp, and W. K. George. Velocity measurements in a high-reynolds-number, momentum-conserving, axisymmetric, turbulent jet. *J. Fluid Mech.*, 258:31–75, 1994.

N. Hutchins and I. Marusic. Large-scale influences in near-wall turbulence. *Phil. Trans. Royal Soc. A: Math., Phys. Eng. Sci.*, 365(1852):647–664, 2007.

W. Hwang and J. K. Eaton. Creating homogeneous and isotropic turbulence without a mean flow. *Exp. Fluids*, 36(3):444–454, 2004.

R. Jahanbakhshi. Mechanisms of entrainment in a turbulent boundary layer. *Phys. Fluids*, 33:035105, 2021.

R Jahanbakhshi and C Madnia. Entrainment in a compressible turbulent shear layer. *J. Fluid Mech.*, 797:564–603, 2016.

Jayesh and Z. Warhaft. Probability distribution, conditional dissipation, and transport of passive temperature fluctuations in grid-generated turbulence. *Phys. Fluids*, 4(10): 2292–2307, 1992.

H. S. Kang, S. Chester, and C. Meneveau. Decaying turbulence in an active-grid-generated flow and comparisons with large-eddy simulation. *J. Fluid Mech.*, 480:129–160, 2003.

K. S. Kankanwadi and O. R. Buxton. Turbulent entrainment into a cylinder wake from a turbulent background. *J. Fluid Mech.*, 905:A35, 2020.

P. S. Karasso and M. G. Mungal. Plif measurements in aqueous flows using the nd: Yag laser. *Exp. Fluids*, 23(5):382–387, 1997.

U. Karnik and S. Tavoularis. Measurements of heat diffusion from a continuous line source in a uniformly sheared turbulent flow. *J. Fluid Mech.*, 202:233–261, 1989.

M. Khashehchi, A. Ooi, J. Soria, and I. Marusic. Evolution of the turbulent/non-turbulent interface of an axisymmetric turbulent jet. *Exp. Fluids*, 54:1449, 2013.

B. Khorsandi, S. Gaskin, and L. Mydlarski. Effect of background turbulence on an axisymmetric turbulent jet. *J. Fluid Mech.*, 736:250–286, 2013.

K. U. Kim, G. S. Elliot, and J. C. Dutton. Compressibility effects on large structures and entrainment length scales in mixing layers. *AIAA Journal*, 58:12, 2020.

K. F. Kohan and S. Gaskin. The effect of the geometric features of the turbulent/non-turbulent interface on the entrainment of a passive scalar into a jet. *Phys. Fluids*, 32: 095114, 2020.

A. N. Kolmogorov. The local structure of turbulence in incompressible viscous fluid for very large reynolds numbers. *Cr Acad. Sci. URSS*, 30:301–305, 1941a.

A. N. Kolmogorov. Dissipation of energy in the locally isotropic turbulence. In *Dokl. Akad. Nauk SSSR A*, volume 32, pages 16–18, 1941b.

M. M. Koochesfahani. *Experiments on turbulent mixing and chemical reactions in a liquid mixing layer*. PhD thesis, California Institute of Technology, 1984.

M. M. Koochesfahani and P. E. Dimotakis. Laser-induced fluorescence measurements of mixed fluid concentration in a liquid plane shear layer. *AIAA journal*, 23(11):1700–1707, 1985.

P-Å. Krogstad and P. A. Davidson. Freely decaying, homogeneous turbulence generated by multi-scale grids. *J. Fluid Mech.*, 680:417–434, 2011.

A. Lacarelle and C. O. Paschereit. Increasing the passive scalar mixing quality of jets in crossflow with fluidics actuators. *J. Eng. Gas Turbines Power*, 134(2), 2012.

A. C. Lai, A. W. K. Law, and E. E. Adams. A second-order integral model for buoyant jets with background homogeneous and isotropic turbulence. *J. Fluid Mech.*, 871:271–304, 2019.

S. Laizet and J. C. Vassilicos. Stirring and scalar transfer by grid-generated turbulence in the presence of a mean scalar gradient. *J. Fluid Mech.*, 764:52–75, 2015.

L. G. Larsen and J. P. Crimaldi. The effect of photobleaching on plif. *Exp. Fluids*, 41(5): 803–812, 2006.

J. C. LaRue and P. A. Libby. Temperature fluctuations in the plane turbulent wake. *Phys. Fluids*, 17:1956–1967, 1974.

R. A. Lavertu and L. Mydlarski. Scalar mixing from a concentrated source in turbulent channel flow. *J. Fluid Mech.*, 528:135–172, 2005.

T. M. Lavertu. *Differential diffusion in a turbulent jet*. PhD thesis, McGill University Libraries, 2006.

T. M. Lavertu, L. Mydlarski, and S. Gaskin. Differential diffusion of high-schmidt-number passive scalars in a turbulent jet. *J. Fluid Mech.*, 612:439–475, 2008.

P. Lavoie, L. Djenidi, and R.A. Antonia. Effects of initial conditions in decaying turbulence generated by passive grids. *J. Fluid Mech.*, 585:395–420, 2007.

A. W. K. Law and H. Wang. Measurement of mixing processes with combined digital particle image velocimetry and planar laser induced fluorescence. *Exp. Thermal and Fluid Sci.*, 22:213–229, 2000.

A. W. K. Law, N. S. Cheng, and Davidson M. J. Jet spreading in oscillating-grid turbulence. In *Proceedings of the 3rd International Symposium on Environmental Hydraulics, IAHR*, pages 1–6, 2001.

D. Legendre, A. Merle, and J. Magnaudet. Wake of a spherical bubble or a solid sphere set fixed in a turbulent environment. *Phys. Fluids*, 18:048102, 2006.

J. Lepore and L. Mydlarski. Lateral dispersion from a concentrated line source in turbulent channel flow. *J. Fluid Mech.*, 678:417–450, 2011.

B. Li, Z. Yang, X. Zhang, G. He, B. Deng, and L. Shen. Using machine learning to detect the turbulent region in flow past a circular cylinder. *J. Fluid Mech.*, 905:A10, 2020.

H. T. Liu, J. T. Lin, D. P. Delisi, and F. A. Robben. Application of a fluorescence technique to dye-concentration measurements in a turbulent jet. In *Proceedings of the symposium on flow measurement in open channels and closed conduits. NBS Special Publication*, volume 484, pages 423–446, 1977.

S. Liu, J. Katz, and C. Meneveau. Evolution and modelling of subgrid scales during rapid straining of turbulence. *J. Fluid Mech.*, 387:281–320, 1999.

F. C. Lockwood and H. A. Moneib. Fluctuating temperature measurements in a heated round free jet. *Combustion Sci. Tech.*, 22(1-2):63–81, 1980.

Y. Long, D. Wu, and J. Wang. A novel and robust method for the turbulent/non-turbulent interface detection. *Exp. Fluids*, 62:138, 2021.

J. Lu, J. P. Fugal, H. Nordsiek, E. W. Saw, R. A Shaw, and W. Yang. Lagrangian particle tracking in three dimensions via single-camera in-line digital holography. *New J. Physics*, 10(12):125013, 2008.

C. L. Lubbers, G. Brethouwer, and B. J. Boersma. Simulation of the mixing of a passive scalar in a round turbulent jet. *Fluid Dyn. Res.*, 28:189, 2001.

N. Machicoane, R. Zimmermann, L. Fiabane, M. Bourgoin, J. Pinton, and R. Volk. Large sphere motion in a nonhomogeneous turbulent flow. *New J. Phys.*, 16(1):013053, 2014.

H. Makita. Realization of a large-scale turbulence field in a small wind tunnel. *Fluid Dyn. Res.*, 8(1-4):53, 1991.

J Mathew and A. J. Basu. Some characteristics of entrainment at a cylindrical turbulence boundary. *Phys. Fluids*, 14(7):2065–2072, 2002.

J. Maurer, P. Tabeling, and G. Zocchi. Statistics of turbulence between two counter-rotating disks in low-temperature helium gas. *Europhys. Lett.*, 26(1):31, 1994.

T. J. McDougall. Measurements of turbulence in a zero-mean-shear mixed layer. *J. Fluid Mech.*, 94(3):409–431, 1979.

S. P. McKenna and W. R. McGillis. Observations of flow repeatability and secondary circulation in an oscillating grid-stirred tank. *Phys. Fluids*, 16(9):3499–3502, 2004.

J. Mi, D. Nobes, and G. Nathan. Influence of jet exit conditions on the passive scalar field of an axisymmetric free jet. *J. Fluid Mech.*, 432:91–125, 2001.

Paul L Miller and Paul E Dimotakis. Reynolds number dependence of scalar fluctuations in a high schmidt number turbulent jet. *Phy. Fluids A: Fluid Dynamics*, 3(5):1156–1163, 1991.

D. Mistry, J. Philip, J. R. Dawson, and I. Marusic. Entrainment at multi-scales across the turbulent/non-turbulent interface in an axisymmetric jet. *J. Fluid Mech.*, 802:690–725, 2016.

M. Moeini, B. Khorsandi, and L. Mydlarski. Effect of coflow turbulence on the dynamics and mixing of a non-buoyant turbulent jet. *J. Hydraulic Eng.*, 147:04020088, 2020.

M. Mohaghar, L. P. Dasi, and D. R. Webster. Scalar power spectra and turbulent scalar length scales of high-schmidt-number passive scalar fields in turbulent boundary layers. *Phys. Rev. Fluids*, 5(8):084606, 2020.

N. Mordant, P. Metz, O. Michel, and J. Pinton. Measurement of lagrangian velocity in fully developed turbulence. *Phys. Rev. Lett.*, 87(21):214501, 2001.

B. R. Morton, G. I. Taylor, and J. S. Turner. Turbulent gravitational convection from maintained and instantaneous sources. *Proc. Royal Soc. London. Series A. Math. Phys. Sci.*, 234 (1196):1–23, 1956.

L Mydlarski. A turbulent quarter century of active grids: from makita (1991) to the present. *Fluid Dyn. Res.*, 49(6):061401, 2017.

L. Mydlarski and Z. Warhaft. On the onset of high-reynolds-number grid-generated wind tunnel turbulence. *J. Fluid Mech.*, 320:331–368, 1996.

J. Nedić and S. Tavoularis. Measurements of passive scalar diffusion downstream of regular and fractal grids. *J. Fluid Mech.*, 800:358–386, 2016.

A. Okubo. Some speculations on oceanic diffusion diagrams. Technical report, Johns Hopkins Univ., Baltimore, Md. Chesapeake Bay Inst., 1972.

Sø. Ott and J. Mann. An experimental investigation of the relative diffusion of particle pairs in three-dimensional turbulent flow. *J. Fluid Mech.*, 422:207–223, 2000.

FK Owen. Simultaneous laser measurements of instantaneous velocity and concentration in turbulent mixing flows. *In AGARD Appl. of Non-Intrusive Instr. in Fluid Flow Res. 7 p (SEE N77-11221 02-31*, 1976.

A. Pal and S. Sarkar. Effect of external turbulence on the evolution of a wake in stratified and unstratified environments. *J. Fluid Mech.*, 772:361–385, 2015.

N. R. Panchapakesan and J. L. Lumley. Turbulence measurements in axisymmetric jets of air and helium. part 1. air jet. *J. Fluid Mech.*, 246:197–223, 1993a.

NR Panchapakesan and JL Lumley. Turbulence measurements in axisymmetric jets of air and helium. part 2. helium jet. *Journal of Fluid Mechanics*, 246:225–247, 1993b.

P. N. Papanicolaou and E. J. List. Investigations of round vertical turbulent buoyant jets. *J. Fluid Mech.*, 195:341–391, 1988.

D. A. Parker, H. C. Burridge, J. Partridge, and P. Linden. A comparison of entrainment in turbulent line plumes adjacent to and distant from a vertical wall. *J. Fluid Mech.*, 882: A4, 2019.

S. V. Patsayeva, V. I. Yuzhakov, and V. Varlamov. Laser-induced fluorescence saturation for binary mixtures of organic luminophores. In *ICONO'98: Laser Spectroscopy and Optical Diagnostics: Novel Trends and Applications in Laser Chemistry, Biophysics, and Biomedicine*, volume 3732, pages 147–156. International Society for Optics and Photonics, 1999.

A. Penzkofer and W. Leupacher. Fluorescence behaviour of highly concentrated rhodamine 6g solutions. *J. Lumin.*, 37(2):61–72, 1987.

A. Perez-Alvarado. *Effect of background turbulence on the scalar field of a turbulent jet*. PhD dissertation, McGill University, Department of Mechanical Engineering, 2016.

A. Perez-Alvarado, L. Mydlarski, and S. Gaskin. Effect of the driving algorithm on the turbulence generated by a random jet array. *Exp. Fluids*, 57:20, 2016.

J. Philip and I. Marusic. Large-scale eddies and their role in entrainment in turbulent jets and wakes. *Phys. Fluids*, 24:055108, 2012.

O. M. Phillips. The irrotational motion outside a free turbulent boundary. In *Mathematical Proceedings of the Cambridge Philosophical Society*, volume 51, pages 220–229. Cambridge University Press, 1955.

S. B. Pope. *Turbulent Flows*. Cambridge University Press, 2000.

S. Rahman and D. R. Webster. The effect of bed roughness on scalar fluctuations in turbulent boundary layers. *Exp. Fluids*, 38(3):372–384, 2005.

N. Reuther and C. J. Kahler. Evaluation of large-scale turbulent/non-turbulent interface detection methods for wall-bounded flows. *Exp. Fluids*, 59:121, 2018.

C. D. Richards and W. M. Pitts. Global density effects on the self-preservation behaviour of turbulent free jets. *J. Fluid Mech.*, 254:417–435, 1993.

L. F. Richardson. Atmospheric diffusion shown on a distance-neighbour graph. *Proceedings of the Royal Society of London. Series A, Containing Papers of a Mathematical and Physical Character*, 110(756):709–737, 1926.

P. J. Roberts and D. R. Webster. *Turbulent Diffusion*. ASCE Press, Reston, Virginia, 2002.

M. M. Rogers, N. N. Mansour, and W. C. Reynolds. An algebraic model for the turbulent flux of a passive scalar. *J. Fluid Mech.*, 203:77–101, 1989.

L. Sabban and R. van Hout. Measurements of pollen grain dispersal in still air and stationary, near homogeneous, isotropic turbulence. *J. Aero. Sci.*, 42(12):867–882, 2011.

L. Sabban, A. Cohen, and R. van Hout. Temporally resolved measurements of heavy, rigid fibre translation and rotation in nearly homogeneous isotropic turbulence. *J. Fluid Mech.*, 814:42–68, 2017.

PG Saffman. On the effect of the molecular diffusivity in turbulent diffusion. *J. Fluid Mech.*, 8(2):273–283, 1960.

R. Sahebjam, K. F. Kohan, and S. Gaskin. The dynamics of an axisymmetric turbulent jet in ambient turbulence interpreted from the passive scalar field statistics. *Phys. Fluids*, 34(1):015129, 2022.

J. P. Salazar and L. R. Collins. Two-particle dispersion in isotropic turbulent flows. *Ann. Rev. Fluid Mech.*, 41:405–432, 2009.

B. Sawford. Turbulent relative dispersion. *Ann. Rev. of Fluid Mech.*, 33(1):289–317, 2001.

B. Sawford and J. C. R. Hunt. Effects of turbulence structure, molecular diffusion and source size on scalar fluctuations in homogeneous turbulence. *J. Fluid Mech.*, 165:373–400, 1986.

J. W. Shan, D. B. Lang, and P. E. Dimotakis. Scalar concentration measurements in liquid-phase flows with pulsed lasers. *Exp. Fluids*, 36(2):268–273, 2004.

P. L. Smart and I. M. S. Laidlaw. An evaluation of some fluorescent dyes for water tracing. *Water Resources Res.*, 13(1):15–33, 1977.

A. Srdic, H. J. S. Fernando, and L. Montenegro. Generation of nearly isotropic turbulence using two oscillating grids. *Exp. Fluids*, 20(5):395–397, 1996.

K. R. Sreenivasan, S. Tavoularis, and S. Corrsin. A test of gradient transport and its generalizations. In *Turbulent Shear Flows*, volume 3, pages 96–112. Springer, 1982.

K. R. Sreenivasan, R. Ramshankar, and C. H. Meneveau. Mixing, entrainment and fractal dimensions of surfaces in turbulent flows. *Proc. Royal Soc. London. A. Math. Phys. Sci.*, 421(1860):79–108, 1989.

H. Stapountzis, B. L. Sawford, J. C. R. Hunt, and R. E. Britter. Structure of the temperature field downwind of a line source in grid turbulence. *J. Fluid Mech.*, 165:401–424, 1986.

H. Suzuki, K. Nagata, and T. Sakai, Y.and Hayase. Direct numerical simulation of turbulent mixing in regular and fractal grid turbulence. *Physica Scripta*, 2010(T142):014065, 2010a.

H. Suzuki, K. Nagata, Y. Sakai, and R. Ukai. High-schmidt-number scalar transfer in regular and fractal grid turbulence. *Physica Scripta*, 2010(T142):014069, 2010b.

R. R. Taveira, J. S. Diogo, D. C. Lopes, and C. B. da Silva. Lagrangian statistics across the turbulent non-turbulent interface in a turbulent plane jet. *Phys. Rev. E*, 88(4):043001, 2013.

S. Tavoularis and S. Corrsin. Experiments in nearly homogeneous turbulent shear flow with a uniform mean temperature gradient. part 1. *J. Fluid Mech.*, 104:311–347, 1981.

S. Tavoularis and S. Corrsin. Effects of shear on the turbulent diffusivity tensor. *Int. J. Heat Mass Transfer*, 28(1):265–276, 1985.

G. I. Taylor. Diffusion by continuous movements. *Proc. London Math. Soc.*, 2(1):196–212, 1921.

G. I. Taylor. Statistical theory of turbulence. *Proc. of the Royal Soc. of London. Series A-Math. and Phys. Sciences*, 151(873):421–444, 1935.

H. Tennekes and J. L. Lumley. *A First Course in Turbulence*. MIT press, 1972.

K. A. Thole and D. G. Bogard. High freestream turbulence effects on turbulent boundary layers. *J. Fluid Eng.*, 1996.

S. M. Thompson and J. S. Turner. Mixing across an interface due to turbulence generated by an oscillating grid. *J. Fluid Mech.*, 67(2):349–368, 1975.

A. A. Townsend. The diffusion behind a line source in homogeneous turbulence. *Proceedings of the Royal Society of London. Series A. Mathematical and Physical Sciences*, 224(1159): 487–512, 1954.

A. A. Townsend. *The Structure of Turbulent Shear Flow*. Cambridge university press, 1956.

A. A. Townsend. The mechanism of entrainment in free turbulent flows. *J. Fluid Mech.*, 26(4):689–715, 1966.

J. S. Turner. Turbulent entrainment: the development of the entrainment assumption, and its application to geophysical flows. *J. Fluid Mech.*, 173:431–471, 1986.

M. S. Uberoi and S. Corrsin. *Diffusion of Heat from a Line Source in Isotropic Turbulence*, volume 1142. National Advisory Committee for Aeronautics, 1952.

P. C. Valente and J. C. Vassilicos. The decay of turbulence generated by a class of multiscale grids. *J. Fluid Mech.*, 687:300–340, 2011.

M. van Reeuwijk and J. Craske. Energy-consistent entrainment relations for jets and plumes. *J. Fluid Mech.*, 782:333–355, 2015.

M. van Reeuwijk and M. Holzner. The turbulence boundary of a temporal jet. *J. Fluid Mech.*, 739:254–275, 2014.

M. van Reeuwijk, J. C. Vassilicos, and J. Craske. Unified description of turbulent entrainment. *J. Fluid Mech.*, 908:A12, 2020.

C. Vanderwel. *Turbulent diffusion in uniformly sheared flow.* PhD thesis, Université d'Ottawa/University of Ottawa, 2014.

C. Vanderwel and S. Tavoularis. Measurements of turbulent diffusion in uniformly sheared flow. *J. Fluid Mech.*, 754:488–514, 2014a.

C. Vanderwel and S. Tavoularis. On the accuracy of plif measurements in slender plumes. *Exp. Fluids*, 55(8):1–16, 2014b.

E. A. Variano and E. A. Cowen. A random-jet-stirred turbulence tank. *J. Fluid Mech.*, 604: 1–32, 2004.

E. A. Variano, E. Bodenschatz, and E. A. Cowen. A random synthetic jet array driven turbulence tank. *Exp. Fluids*, 37:613–615, 2008.

E. Villermaux, B. Sixou, and Y. Gagne. Intense vortical structures in grid-generated turbulence. *Phys. Fluids*, 7(8):2008–2013, 1995.

G. A. Voth, A. La Porta, A. M. Crawford, J. Alexander, and E. Bodenschatz. Measurement of particle accelerations in fully developed turbulence. *Journal of Fluid Mechanics*, 469: 121–160, 2002.

DA Walker. A fluorescence technique for measurement of concentration in mixing liquids. *Journal of Physics E: Scientific Instruments*, 20(2):217, 1987.

G. R. Wang and H. E. Fiedler. On high spatial resolution scalar measurement with lif part 1: Photobleaching and thermal blooming. *Exp. Fluids*, 29(3):257–264, 2000a.

G. R. Wang and H. E. Fiedler. On high spatial resolution scalar measurement with lif part 2: The noise characteristic. *Exp. Fluids*, 29(3):265–274, 2000b.

H. Wang and A. W. K. Law. Second-order integral model for a round turbulent buoyant jet. *J. Fluid Mech.*, 459:397–428, 2002.

Z. Warhaft. The interference of thermal fields from line sources in grid turbulence. *J. Fluid Mech.*, 144:363–387, 1984.

T. A. Warnaars, M. Hondzo, and M. A. Carper. A desktop apparatus for studying interactions between microorganisms and small-scale fluid motion. *Hydrobiologia*, 563(1): 431–443, 2006.

T. Watanabe, X. Zhang, and K. Nagata. Turbulent/non-turbulent interfaces detected in dns of incompressible turbulent boundary layers. *Phys. Fluids*, 30:035102, 2018.

D. R. Webster, P. J. Roberts, and L. Ra'ad. Simultaneous DPTV-PLIF measurements of a turbulent jet. *Exp. in Fluids*, 30:65–72, 2001.

D. R. Webster, S. Rahman, and L. P. Dasi. Laser-induced fluorescence measurements of a turbulent plume. *J. Eng. Mech.*, 129(10):1130–1137, 2003.

D.R. Webster and A. Brathwaite. A novel laboratory apparatus for simulating isotropic oceanic turbulence at low Reynolds number. *Limnology and Oceanography: Methods*, 2: 1–12, 2004.

J. Westerweel, C. Fukushima, J. M. Pedersen, and J. C. R. Hunt. Mechanics of the turbulent-nonturbulent interface of a jet. *Phys. Rev. Lett.*, 95(17):174501, 2005.

J Westerweel, C Fukushima, Jakob Martin Pedersen, and JCR Hunt. Momentum and scalar transport at the turbulent/non-turbulent interface of a jet. *Journal of Fluid Mechanics*, 631:199–230, 2009.

R. A. M. Wilson and P. V. Danckwerts. Studies in turbulent mixing—ii: A hot-air jet. *Chem. Eng. Science*, 19(11):885–895, 1964.

M. Wolf, B. Lüthi, M. Holzner, D. Krug, W. Kinzelbach, and A. Tsinober. Investigations on the local entrainment velocity in a turbulent jet. *Phys. Fluids*, 24(10):105110, 2012.

S. J. Wright. The effect of ambient turbulence on jet mixing. *In Recent Research Advances in the Fluid Mechanics of Turbulent Jets and Plumes*, 255:13–27, 1994.

Z. Wu, J. Lee, C. Meneveau, and T. Zaki. Application of a self-organizing map to identify the turbulent-boundary-layer interface in a transitional flow. *Phys. Rev. Fluids*, 4:023902, 2019.

C. Würth, M. G. González, R. Niessner, U. Panne, C. Haisch, and U. R. Genger. Determination of the absolute fluorescence quantum yield of rhodamine 6g with optical and photoacoustic methods – providing the basis for fluorescence quantum yield standards. *Talanta*, 90:30–37, 2012.

I. Wygnanski and H. Fiedler. Some measurements in the self-preserving jet. *J. Fluid Mech.*, 38(3):577–612, 1969.

G. Xu and R. Antonia. Some measurements in the self-preserving jet. *Experiments in fluids*, 33(5)(5):677–683, 2002.

J. You and T. A. Zaki. Conditional statistics and flow structures in turbulent boundary layers buffeted by free-stream disturbances. *J. Fluid Mech.*, 866:526–566, 2019.

K. Younes, B. Gibeau, S. Ghaemi, and J. Hickey. A fuzzy cluster method for turbulent/non-turbulent interface detection. *Exp. Fluids*, 62:73, 2021.

D. L. Young, D. R. Webster, and A. I. Larsson. Structure and mixing of a meandering turbulent chemical plume: turbulent mixing and eddy diffusivity. *Exp. Fluids*, 63(1): 1–11, 2022.

B. A. Younis, C. G. Speziale, and T. T. Clark. A rational model for the turbulent scalar fluxes. *Proc. R. Soc. Lond.*, 461(2054):575–594, 2005.

R. Zimmermann, H. Xu, Y. Gasteuil, M. Bourgoin, R. Volk, J. Pinton, and E. Bodenschatz. The lagrangian exploration module: An apparatus for the study of statistically homogeneous and isotropic turbulence. *Rev. Sci. Instrum.*, 81(5):055112, 2010.